


5-2010

Thoracic radiotherapy treatment planning with cine PET/CT

Adam C. Riegel

Follow this and additional works at: http://digitalcommons.library.tmc.edu/utgsbs_dissertations

 Part of the [Medical Biophysics Commons](#), [Oncology Commons](#), [Other Physics Commons](#), and the [Radiology Commons](#)

Recommended Citation

Riegel, Adam C., "Thoracic radiotherapy treatment planning with cine PET/CT" (2010). *UT GSBS Dissertations and Theses (Open Access)*. Paper 19.

This Dissertation (PhD) is brought to you for free and open access by the Graduate School of Biomedical Sciences at DigitalCommons@The Texas Medical Center. It has been accepted for inclusion in UT GSBS Dissertations and Theses (Open Access) by an authorized administrator of DigitalCommons@The Texas Medical Center. For more information, please contact laurel.sanders@library.tmc.edu.

**THORACIC RADIOTHERAPY TREATMENT PLANNING
WITH CINE PET/CT**

**A
DISSERTATION**

Presented to the Faculty of
The University of Texas
Health Science Center at Houston
and
The University of Texas
M. D. Anderson Cancer Center
Graduate School of Biomedical Sciences
In Partial Fulfillment

of the Requirements

for the Degree of
DOCTOR OF PHILOSOPHY

by

Adam Christopher Riegel, B.A.
Houston, TX

May, 2010

Copyright © 2010 Adam C. Riegel
All rights reserved

DEDICATION

This work is dedicated to my family: My Mom, for always being there when I needed someone to listen; my Dad, for being my hero and providing a model for the kind of man I want to be; my sister Alex, for her unwavering support, love, and humor; and Kim, my soon-to-be wife, whose love and encouragement lifted me from start to finish.

This work is also dedicated to all who suffer from cancer, the patients and families who I have seen in the halls and waiting rooms of M. D. Anderson and beyond. Knowing that my research was helping these brave people inspired me to get up early and stay late completing this work.

ACKNOWLEDGEMENTS

First and foremost, I would like to thank Tinsu Pan for his guidance and support. Learning from Dr. Pan has been an invaluable experience and I cannot thank him enough for granting me the opportunity.

I would like to thank Osama Mawlawi for his pedagogical assistance, of course, but more importantly, for encouraging me to accept nothing less than excellence in my research.

Thanks also to George Starkschall, Sastry Vedam, Valen Johnson, the other members of my committee whose advice over the years has greatly contributed to this work, and to Drs. Joe Chang and Kara Bucci whose assistance in contouring was vital to the project.

Beyond my committee, there are many other people in the medical physics program whose help was invaluable to my studies. Thanks especially to Ed Jackson, John Hazle, Georgeanne Moore, and Kathy Prentice. A special thanks to my lab-mates Melinda Chi and Moiz Ahmad for being there to bounce ideas around, and, of course, thanks to all my fellow students.

Thanks also to George Stancel and Thomas Goka at the Graduate School of Biomedical Sciences for their continued support of the medical physics program.

Finally, I would like to acknowledge and thank the Schissler Foundation for their generous funding support in 2008.

THORACIC RADIOTHERAPY TREATMENT PLANNING

WITH CINE PET/CT

Publication No. _____

Adam Christopher Riegel, B.A.

Supervisory Professor: Tinsu Pan, Ph.D.

Purpose: Respiratory motion causes substantial uncertainty in radiotherapy treatment planning. Four-dimensional computed tomography (4D-CT) is a useful tool to image tumor motion during normal respiration. Treatment margins can be reduced by targeting the motion path of the tumor. The expense and complexity of 4D-CT, however, may be cost-prohibitive at some facilities. We developed an image processing technique to produce images from cine CT that contain significant motion information without 4D-CT. The purpose of this work was to compare cine CT and 4D-CT for the purposes of target delineation and dose calculation, and to explore the role of PET in target delineation of lung cancer.

Methods: To determine whether cine CT could substitute 4D-CT for small mobile lung tumors, we compared target volumes delineated by a physician on cine CT and 4D-CT for 27 tumors with intrafractional motion greater than 1 cm. We assessed dose calculation by comparing dose distributions calculated on respiratory-averaged cine CT and respiratory-averaged 4D-CT using the gamma index. A threshold-based PET segmentation model of size, motion, and source-to-background was developed from phantom scans and validated with 24 lung tumors. Finally, feasibility of integrating cine CT and PET for contouring was assessed on a small group of larger tumors.

Results: Cine CT to 4D-CT target volume ratios were (1.05 ± 0.14) and (0.97 ± 0.13) for high-contrast and low-contrast tumors respectively which was within intraobserver variation. Dose distributions on cine CT produced good agreement ($< 2\%/1 \text{ mm}$) with 4D-CT for 71 of 73 patients. The segmentation model fit the phantom data with $R^2 = 0.96$ and produced

PET target volumes that matched CT better than 6 published methods (-5.15%). Application of the model to more complex tumors produced mixed results and further research is necessary to adequately integrate PET and cine CT for delineation.

Conclusions: Cine CT can be used for target delineation of small mobile lesions with minimal differences to 4D-CT. PET, utilizing the segmentation model, can provide additional contrast. Additional research is required to assess the efficacy of complex tumor delineation with cine CT and PET. Respiratory-averaged cine CT can substitute respiratory-averaged 4D-CT for dose calculation with negligible differences.

TABLE OF CONTENTS

DEDICATION III

ACKNOWLEDGEMENTS IV

LIST OF FIGURES..... XI

LIST OF TABLESXVII

ABBREVIATIONS.....XVIII

CHAPTER 1 INTRODUCTION AND BACKGROUND 1

1.1 INTRODUCTION 1

1.2 BACKGROUND AND SIGNIFICANCE 3

1.3 SUMMARY OF CHAPTERS..... 15

1.3.1 *Chapter 2: Target Delineation of Stage I Non-Small Cell Lung Cancer with Cine CT.* 15

1.3.2 *Chapter 3: Dose Calculation with Cine Respiratory-Averaged CT* 16

1.3.3 *Chapter 4: Segmentation of Moving Targets with PET/CT: Correlation of Thresholds with Lesion Size, Motion Extent, and Source-to-Background Ratio*..... 17

1.3.4 *Chapter 5: Target Delineation of Stage III Non-Small Cell Lung Cancer with Cine PET/CT* 18

1.3.5 *Chapters 6 and 7: Discussion and Conclusions*..... 18

CHAPTER 2 TARGET DELINEATION OF STAGE I NON-SMALL CELL LUNG CANCER WITH CINE CT..... 19

2.1 INTRODUCTION 19

2.2 PURPOSE..... 22

2.3 METHODS 22

2.3.1 *Phantom Study* 22

2.3.2 *Patient Study* 24

2.3.3 *Analysis*..... 26

2.4 RESULTS..... 27

2.4.1 *Phantom Study* 27

2.4.2 *Patient Study* 28

2.5	DISCUSSION	32
2.6	CONCLUSIONS.....	37
CHAPTER 3 DOSE CALCULATION WITH CINE RESPIRATORY-AVERAGED CT		38
3.1	INTRODUCTION	38
3.2	PURPOSE.....	40
3.3	METHODS	41
3.3.1	<i>Patient Study</i>	41
3.3.2	<i>Analysis</i>	46
3.4	RESULTS.....	48
3.4.1	<i>Primary Patient Group</i>	48
3.4.2	<i>Follow-up Patient Group</i>	51
3.5	DISCUSSION	54
3.6	CONCLUSIONS.....	60
CHAPTER 4 SEGMENTATION OF MOVING TARGETS WITH PET/CT: CORRELATION OF THRESHOLDS WITH LESION SIZE, MOTION EXTENT, AND SOURCE-TO-BACKGROUND RATIO.....		61
4.1	INTRODUCTION	61
4.2	PURPOSE.....	62
4.3	METHODS	63
4.3.1	<i>Terminology</i>	63
4.3.2	<i>Development of the Regression Model</i>	64
4.3.2.1	Phantom Scanning	64
4.3.2.2	Target Delineation	66
4.3.2.3	Analysis	67
4.3.3	<i>Application of the Regression Function to Patients</i>	71
4.3.3.1	Imaging.....	71
4.3.3.2	Target Delineation	72
4.3.3.3	Recovery Coefficient	74
4.3.3.4	Analysis	74
4.4	RESULTS.....	77

4.4.1	<i>Volume/Motion/SBR Segmentation Model</i>	77
4.4.2	<i>Application to Patient Studies</i>	83
4.5	DISCUSSION	90
4.6	CONCLUSIONS	97
CHAPTER 5 FEASIBILITY OF TARGET DELINEATION OF STAGE III NON-SMALL CELL LUNG CANCER WITH CINE PET/CT		98
5.1	INTRODUCTION	98
5.2	PURPOSE.....	98
5.3	METHODS	99
5.4	RESULTS.....	101
5.4.1	<i>Patient 1</i>	101
5.4.2	<i>Patient 2</i>	102
5.4.3	<i>Patient 3</i>	103
5.4.4	<i>Patient 4</i>	104
5.4.5	<i>Patient 5</i>	105
5.5	DISCUSSION	105
5.6	CONCLUSIONS	106
CHAPTER 6 DISCUSSION.....		107
6.1	SIGNIFICANCE AND IMPACT	107
6.2	FUTURE WORK.....	112
6.2.1	<i>Weighted Maximum Intensity Projection (wMIP)</i>	112
6.2.2	<i>Improvement in PET Uptake Quantification</i>	112
6.2.3	<i>Fine-Tuning the Volume/Motion/SBR Model</i>	113
6.2.4	<i>Nodal Involvement in Stage III Non-Small Cell Lung Cancer</i>	113
CHAPTER 7 CONCLUSIONS AND RECOMMENDATIONS		115
CHAPTER 8 APPENDIX.....		116
8.1	SAMPLING THE REFERENCE SURFACE.....	116
8.2	DETERMINATION OF SHORTEST DISTANCE BETWEEN REFERENCE AND TEST SURFACES.....	118
8.2.1	<i>Faces</i>	118

8.2.2	<i>Edges</i>	120
REFERENCES	122
VITA	140

LIST OF FIGURES

Figure 1.1: Target volumes as described by ICRU 62 (left) and M. D. Anderson convention (right). GTV = gross tumor volume. CTV = clinical target volume. ITV = internal target volume. PTV = planning target volume. IGTV = internal gross tumor volume. ICTV = internal clinical target volume. EE = end-expiration. EI = end-inspiration. The M. D. Anderson approach utilizes 4D-CT to define a patient-specific motion path characterized by IGTV. 6

Figure 1.2: (A) maximum intensity projection and (B) respiratory-averaged CT from 4D-CT. End-expiration and end-inspiration, the extremes of respiratory motion, are shown in 4D-CT phase images (C) 50% phase and (D) 0% phase..... 8

Figure 1.3: Image processing of 4D-CT imaging versus raw cine CT imaging. MIP = maximum intensity projection, RACT = respiration-averaged computed tomography. Reproduced with permission from Riegel *et al.* (Riegel et al., 2009) 9

Figure 1.4: Sagittal views of a moving lesion obscured by the liver. (A) MIP without contour. (B) MIP with end-inspiration tumor contour (orange). (C) End-inspiration phase with contour drawn for reference. Note that the inferior border of the tumor is nearly impossible to delineate with the MIP alone..... 10

Figure 1.5: Sagittal CT image of tumor near the chest wall. (left) Maximum intensity projection. (right) Respiratory-averaged CT. Reproduced with permission from Riegel *et al.* (Riegel et al., 2009) 10

Figure 1.6: PET image of 37 mm diameter sphere moving at 0, 10, 20, and 30 mm sinusoidal motion..... 13

Figure 2.1: Respiratory surrogate setup for 4D-CT acquisition. The infrared camera tracks the movement of the infrared reflector on the patient’s abdomen to record the respiratory motion trace..... 20

Figure 2.2: NEMA IEC thorax phantom (Data Spectrum, Chapel Hill, NC) placed on a motion platform driven by a single-axis stepper motor (Velmex Inc., Bloomfield, NY). Note the RPM block placed on the phantom. 23

Figure 2.3: Mean volume magnitudes for high and low contrast tumors. Red error bars are the 95% confidence interval around the mean. Black error bars represent mean intraobserver variation for 3 re-contoured patients. Reproduced with permission from Riegel *et al.* (Riegel et al., 2009)..... 31

Figure 2.4: Transverse CT image of tumor adjacent to the liver. (left) Maximum intensity projection. (right) Respiratory-averaged CT. Reproduced with permission from Riegel *et al.* (Riegel et al., 2009) 32

Figure 2.5: Observed motion extent in 4D-CT (top) versus observed motion extent in MIP_{cine}. Note that in 4D-CT, images that reflected the full motion extent were not included in the phase imaging. In MIP_{cine}, however, all images are included and maximum motion extent is imaged. Reproduced with permission from Riegel *et al.* (Riegel et al., 2009) 33

Figure 2.6: Maximum intensity projections processed from 4D-CT (top row) and cine CT (bottom row). Red contours are IGTV_{cine} and green are IGTV_{4D-CT}. Note that cine CT captures several slices of tumor motion beyond that captured by 4D-CT. Reproduced with permission from Riegel *et al.* (Riegel et al., 2009)..... 35

Figure 3.1: $\sin(x)$ and the average of $\sin(x)$. Reproduced with permission from Riegel *et al.* (Riegel et al., 2008) 40

Figure 3.2: Overemphasis of sections of the respiratory pattern. The yellow-shaded region represents one period of the respiratory cycle and the orange-shaded region is the part of the breathing cycle averaged twice in RACT_{cine}, thereby “weighting” the image towards the repeated phase of the breathing cycle. Reproduced with permission from Riegel *et al.* 42

Figure 3.3: Intersection of planning target volume (PTV) and orthogonal dose planes. Reproduced with permission from Riegel *et al.* (Riegel et al., 2008)..... 47

Figure 3.4: (A) Maximum and (B) mean gamma (γ) indices for patients with regular respiratory patterns. Error bars are standard error (N=11). Reproduced with permission from Riegel *et al.* (Riegel et al., 2008)..... 49

Figure 3.5: (A) Maximum and (B) mean gamma (γ) indices for patients with irregular respiratory patterns. Error bars are standard error (N=12). Green arrows are significant differences as determined by ANOVA/Tukey HSD tests. Reproduced with permission from Riegel *et al.* (Riegel et al., 2008)..... 50

Figure 3.6: (A) Maximum and (B) mean gamma indices inside the PTV for the follow-up patient group. Error bars are standard error. Reproduced with permission from Riegel *et al.* (Riegel et al., 2008) 52

Figure 3.7: (A) Maximum and (B) mean gamma indices inside the PTV for the follow-up patient group, separated by treatment technique. IMRT = intensity modulated radiation therapy. SBRT = stereotactic body radiation therapy. Reproduced with permission from Riegel *et al.* (Riegel et al., 2008)..... 53

Figure 3.8: (A) Coronal RACT_{4D-CT} and (B) Coronal γ distribution for patient 40 of the follow-up group. Note that our 2%/1mm γ criteria are violated at the maximum extents of tumor motion. Reproduced with permission from Riegel *et al.* (Riegel et al., 2008) 56

Figure 3.9: The "dose shadowing" effect, demonstrated by calculating dose on end-inspiration and end-expiration of a 4D-CT and comparing the distributions. The difference image (A) between the end-inspiration phase CT and end-expiration phase CT highlight changes in anatomy due to motion. The gamma (γ) index distribution for a single oblique beam (B) shows the streaks of dose disagreement behind the moving anatomy. Reproduced with permission from Riegel *et al.* (Riegel et al., 2008) 57

Figure 3.10: Shadowing effect seen in patient 20 of the primary group. Pink arrows highlight areas of moving anatomy on the coronal RACT_{4D-CT} (A) and transverse RACT_{4D-CT} (B). Stripes of disagreement can be seen medial to the beam entrances behind the moving anatomy. Reproduced with permission from Riegel *et al.* (Riegel et al., 2008) 58

Figure 4.1: NEMA IEC thorax phantom on 1-D motion on flat couch of GE Discovery VCT PET/CT scanner. Reproduced with permission from Riegel *et al.* (Riegel et al., 2010) 65

Figure 4.2: Minimum intensity projection from cine CT ($\text{min-IP}_{\text{cine}}$) for 37 and 28 mm diameter spheres of NEMA IEC phantom. From left to right: 0, 10, 20, and 30 mm motion amplitude. 66

Figure 4.3: (Top) The test mesh (red) is compared with a reference mesh (black) with the surface separation algorithm. Blue lines represent shortest distances between sampling points on the reference mesh and the test mesh surface. (Bottom) Deviations are expressed in terms of altitudinal and azimuthal angles..... 69

Figure 4.4: Transverse, sagittal, and coronal PET images of the 37 mm inner diameter sphere moving at 20 mm sinusoidal motion amplitude. The green contour represents IGTV_{CT} derived from cine CT. Purple contours represent $\text{IGTV}_{\text{PET}_n\%}$ at a range of activity concentration thresholds. The optimal threshold (the threshold that created the purple ROI most similar to the green ROI) was determined with the surface separation algorithm. Reproduced with permission from Riegel *et al.* (Riegel et al., 2010) 76

Figure 4.5: Optimal thresholds (normalized to background) versus motion, source-to-background (SBR), and sphere volume. Volume is denoted by the different colors and symbols shown in the legend (which lists nominal sphere diameters). Error bars represent 1 standard deviation. Reproduced with permission from Riegel *et al.* (Riegel et al., 2010) 78

Figure 4.6: Optimal threshold versus source-to-background for stationary spheres. Each line represents a different sphere diameter as denoted in the legend. Note the linear nature of the relationship. Error bars are 1 standard deviation (3 measurements). Reproduced with permission from Riegel *et al.* (Riegel et al., 2010) 79

Figure 4.7: Optimal threshold versus motion for source-to-background = 19.9. Each line represents a sphere diameter as shown in the legend. Error bars are 1 standard deviation (3 measurements). Reproduced with permission from Riegel *et al.* (Riegel et al., 2010) 80

Figure 4.8: Optimal threshold versus volume for source-to-background = 19.9. Each line represents motion extent (0 mm to 30 mm). Error bars are 1 standard deviation (3 measurements). Reproduced with permission from Riegel *et al.* (Riegel et al., 2010) 80

Figure 4.9: Surfaces of regression function defined in equation (12). Each of the 4 surfaces displayed is calculated for spheres of inner diameter 10, 17, 28, and 37 mm. Reproduced with permission from Riegel *et al.* (Riegel et al., 2010) 82

Figure 4.10: Correlation between predicted threshold values and measured optimal threshold values for each segmentation method. Best-fit lines, their equations, and R^2 values of the fit are shown in each plot. 85

Figure 4.11: (A) Transverse, (B) sagittal, and (C) coronal PET/CT images of tumor 13 with internal gross tumor volume (IGTV) contours. PET is displayed with a “thermal” colormap. $IGTV_{CT}$, shown in red, was delineated on MIP_{cine} . Other IGTVs were delineated on PET using methods described in Table 4.1. The contour from the volume/motion/SBR model ($IGTV_{V,M,SBR}$) is shown in green..... 86

Figure 4.12: (A) Transverse, (B) sagittal, and (C) coronal PET/CT images of tumor 1 with internal gross tumor volume (IGTV) contours. PET is displayed with a “thermal” colormap. $IGTV_{CT}$, shown in red, was delineated on MIP_{cine} . Other IGTVs were delineated on PET using methods described in Table 4.1. The contour from the volume/motion/SBR model ($IGTV_{V,M,SBR}$) is shown in green..... 87

Figure 4.13: Volumes (in cubic centimeters) of $IGTV_{PET}$ and $IGTV_{CT}$. Error bars represent standard error of the mean (N = 24 tumors for $IGTV_{35\%}$, $IGTV_{42\%}$, $IGTV_{15\%+BG}$, $IGTV_{SUVmean}$, $IGTV_{V,M,SBR}$, N = 22 for $IGTV_{2.5}$, N = 18 for $IGTV_{15\%}$). p-values are shown with each column (green = significant, red = non-significant). 89

Figure 4.14: Surface separation (in millimeters) between $IGTV_{PET}$ and $IGTV_{CT}$. Error bars represent standard error of the mean (N = 24 tumors for $IGTV_{35\%}$, $IGTV_{42\%}$, $IGTV_{15\%+BG}$, $IGTV_{SUVmean}$, $IGTV_{V,M,SBR}$, N = 22 for $IGTV_{2.5}$, N = 18 for $IGTV_{15\%}$). p-values are shown with each column (green = significant, red = non-significant). 89

Figure 4.15: Reference volume for stationary sphere (black mesh, inner diameter = 28 mm) compared with 35% maximum activity concentration of same volume sphere at 30 mm motion extent and source-to-background = 19.9 (red mesh). Note that the 35% threshold underestimates the axial and overestimates the sagittal extent of the sphere, but underestimates the full motion envelope of the tumor. Reproduced with permission from Riegel *et al.* (Riegel et al., 2010)..... 93

Figure 5.1: Microsoft Excel spreadsheet used to calculate thresholds using volume/motion/SBR model. 100

Figure 5.2: Sagittal PET/CT data set and volume/motion/SBR contour (green line) for patient 1. For this particular patient, PET was performed prior to 4D-CT simulation and was manually registered to the maximum intensity projection. 101

Figure 5.3: Coronal PET/CT data set and volume/motion/SBR contours for patient 2. Green line represents contour when $AC_{80\%}$ is used in volume/motion/SBR model. Blue line represents contour when mean AC in manually drawn contour in middle of tumor is used in volume/motion/SBR model. 102

Figure 5.4: Sagittal PET/CT data set and volume/motion/SBR contour (green line) for patient 3..... 103

Figure 5.5: Coronal (left) and transverse (right) PET/CT data set and volume/motion/SBR contour (green line) for patient 4. Note the atelectasis present in the left upper lobe on the transverse CT image. 104

Figure 5.6: Sagittal (left) and transverse (right) PET/CT data set and volume/motion/SBR contour (green line) for patient 5..... 105

Figure 6.1: Workflow for (top) 4D-CT and PET acquisition versus (bottom) cine CT and PET acquisition..... 111

Figure 8.1: End result of the surface separation algorithm. Black mesh is "reference" mesh. Red mesh is "test" mesh. Blue lines represent shortest distances from the sampling points on the reference mesh to the test mesh surface. 121

LIST OF TABLES

Table 1.1: Non-small cell lung cancer staging system based on TNM classification	3
Table 2.1: Significance values for phantom study	28
Table 2.2: Internal gross tumor volume (IGTV) measurements for high-contrast patients..	29
Table 2.3: Internal gross tumor volume (IGTV) measurements for low-contrast patients..	30
Table 3.1: Primary group patient characteristics.....	43
Table 3.2: Follow-up group patient characteristics.	45
Table 4.1: Tumor delineation methods on PET	72
Table 4.2: Nominal and actual volumes and SBRs	77
Table 4.3: Regression coefficients for model in equation (11).	82
Table 4.4: Volume, motion, and source-to-background characteristics of 24 lung tumors, with model-produced threshold.....	84
Table 4.5: Comparison of $IGTV_{PET}$ with $IGTV_{CT}$ for different segmentation methods	88
Table 5.1: Patients for cine PET/CT feasibility study	99

ABBREVIATIONS

3DCRT	Three-Dimensional Conformal Radiation Therapy
4D-CT	Four-Dimensional Computed Tomography
AAPM	American Association of Physicists in Medicine
AC	Activity Concentration
ACS	American Cancer Society
AJCC	American Joint Committee on Cancer
AW	Advantage Workstation
CCC	Collapsed-Cone Convolution
COV	Coefficient of Variation
CT	Computed Tomography
CTV	Clinical Tumor Volume
DSC	Dice Similarity Coefficient
FOV	Field of View
FWHM	Full-Width Half-Maximum
GE	General Electric
GTV	Gross Tumor Volume
HU	Hounsfield Unit
ICRU	International Commission on Radiation Units and Measurements
IEC	International Electrotechnical Commission
IGRT	Image-Guided Radiation Therapy
IGTV	Internal Gross Tumor Volume
IMRT	Intensity-Modulated Radiation Therapy
IRB	Institutional Review Board
ITV	Internal Target Volume
Min-IP	Minimum Intensity Projection
MIP	Maximum Intensity Projection
MLEM	Maximum Likelihood Expectation Maximization

NCI	National Cancer Institute
NDSC	Normalized Dice Similarity Coefficient
NEMA	National Electrical Manufacturers Association
NSCLC	Non-Small Cell Lung Cancer
OSEM	Ordered Subsets Expectation Maximization
PACS	Picture Archiving and Communication System
PET	Positron Emission Tomography
PTV	Planning Target Volume
RACT	Respiratory-Averaged Computed Tomography
RC	Recovery Coefficient
ROI	Region of Interest
RPM	Real-time Positioning Management system
SBR	Source-to-Background Ratio
SBRT	Stereotactic Body Radiation Therapy
Voxel	Volume Element
VTK	Visualization ToolKit

Chapter 1 INTRODUCTION AND BACKGROUND

1.1 Introduction

In 2009, an estimated 220,000 new cases of lung cancer were diagnosed, 87% of which were non-small cell lung cancer (NSCLC). Deaths from lung cancer in 2009 were projected to reach nearly 160,000, substantially higher than deaths attributed to prostate, breast, and colorectal cancer combined. Lung cancer deaths account for 28% of all cancer deaths in the United States (ACS, 2009). Radiation therapy is one important treatment option for both early and later stage NSCLC. Shown to be an effective alternative to surgical resection, radiation therapy can produce 5-year survival rates up to 27% for stage I patients unfit or unwilling to undergo surgical resection (Dosoretz et al., 1992; Gauden et al., 1995). Stage III patients are often treated with radiation therapy alone or a combination of radiation therapy and chemotherapy, which, in terms of one-year survival, was demonstrated to be statistically superior to radiation therapy alone (Sause et al., 1995). The increasing use of radiation therapy in treatment of lung cancer has driven great technological advances in the last decade, including intensity-modulated radiation therapy (IMRT) and image-guided radiation therapy (IGRT). Treatment planning technology has, necessarily, kept pace.

When patients are slated for radiation therapy, they first receive an imaging exam on which the radiation treatment is planned. This exam, typically a computed tomography (CT) exam, is performed in the treatment position and is often called a CT “simulation,” referring to the fact that imaging geometry and patient setup mimic the geometry in the treatment room. There are many uncertainties in treatment planning, but for lung cancer patients, respiratory motion is especially significant. Typical helical CT scans can cause significant image artifacts (Chen et al., 2004) which could lead to inaccurate targeting of the tumor.

In 2004, a new imaging technology was introduced for CT simulation of lung cancer. Four-dimensional computed tomography (4D-CT) enables physicists to capture a 3-D movie of the patient’s respiratory pattern, thereby accurately representing the movement of the

tumor and allowing physicians to account for motion in the treatment plan (Keall et al., 2004; Low et al., 2003; Pan et al., 2004; Rietzel et al., 2005). Typically, physicians will aim radiation beams at the entire motion path of the tumor to ensure that the tumor stays within the beam during the entire respiratory cycle.

A huge technological breakthrough, 4D-CT has become very popular in the last 5 years and has been adopted for CT simulation of lung cancer treatment at many centers around the world including M. D. Anderson in Houston, Texas. The American Association of Physicists in Medicine (AAPM) Task Group 76 highlights 4D-CT as a technique to effectively assess tumor motion (Keall et al., 2006).

Parallel to the impressive advancement of medical technology in the last few decades, however, is the steep increase in healthcare costs. The implementation of 4D-CT is an example of one of these increases. The acquisition of 4D-CT imaging is a complex process: Besides the scanner itself, additional hardware from a different vendor is required to track the respiratory pattern of the patient. Such hardware may cost an additional \$75,000. In the General Electric implementation of 4D-CT, two additional pieces of software are required to create 4D-CT images which, along with the proprietary workstation on which the software runs, together may cost \$300,000. After installation of the technology, trained physicists and technicians must be present to ensure high-quality image acquisition which, of course, will incur additional costs. Though such costs may be minimal to an institution like M. D. Anderson or comparable university hospitals across the United States, many smaller hospitals and clinics cannot afford such expenses after purchasing the scanner itself.

Fortunately, there may be a way to make sophisticated imaging technology available to the majority of hospitals with average resources. By manipulating CT images that are used to create 4D-CT through re-sorting and image processing, we can create image sets which contain significant motion information without additional hardware and minimal software (Pan et al., 2006; Pan et al., 2007). These images could be used to plan radiation therapy at a fraction of the cost of 4D-CT.

The purpose of this dissertation was to determine if these alternative image sets, generated by a process called “cine CT,” could, in conjunction with functional imaging such as PET, be used for treatment simulation in place of 4D-CT. The work focused on demonstrating equivalence of target delineation and dose calculation using cine CT and PET compared with 4D-CT.

1.2 Background and Significance

Patients with NSCLC are staged according to the Revised International System for Staging Lung Cancer which was adopted by the American Joint Committee on Cancer in 1997 (NCI, 2010). The system utilizes combinations of TNM classification to stratify patients and is summarized in Table 1.1. “T” is generally determined by measuring tumor size. “N” is found by assessing spread to regional lymph nodes. “M” is essentially a binary value indicating whether or not the patient has distant metastasis. Because definitive radiation therapy is particularly important for stage I and stage III NSCLC, the following investigations are focused on these particular stages.

Table 1.1: Non-small cell lung cancer staging system based on TNM classification

IA	IB	IIA	IIB	IIIA	IIIB	IV
T1 N0 M0	T2 N0 M0	T1 N1 M0	T2 N1 M0	T1 N2 M0	T* N3 M0	T* N* M1
			T3 N0 M0	T2 N2 M0	T4 N* M0	
				T3 N1 M0		
				T3 N2 M0		

* = any numerical value

T = tumor stage

N = regional nodal status

M = distal metastasis

Computed tomography (CT) has revolutionized the treatment planning process for radiation therapy, facilitating the transition from two-dimensional planning to three-dimensional treatment simulation. CT, like conventional radiography, is a projection x-ray modality. In current “third-generation” CT scanners, x-rays are produced in a fan beam by

an x-ray tube rotating around the patient on a slip-ring gantry. The detector array rotates with the gantry, capturing projections from different angles through the patient. Projections are acquired at typical diagnostic energies such as 120 kVp, which provides a mean energy of 60-70 keV for a polyenergetic x-ray spectrum. At these energies, the photoelectric effect dominates total attenuation coefficient and produces useful contrast in the x-ray projections. Transverse images are reconstructed using filtered backprojection. Iterative reconstruction algorithms have been investigated (Marin et al., 2010), but are computationally intensive. Graphics processing unit (GPU) reconstruction may expedite the process (Xu et al., 2007). Obviously, scanner characteristics vary with manufacturer and model, but many modern scanners are capable of multi-slice helical CT in which the detector array consists of many individual detectors in the longitudinal direction (through the scanner bore) that can be binned together to detect photons over a certain area. The height of this binned area in the longitudinal direction defines the slice thickness. The number of slices is defined by the number of data channels available. Helical acquisition is performed by continuously moving the couch while the beam is on and acquiring data in a “candy-stripe” pattern around the patient. Helical projection data is interpolated to form projections at evenly spaced transverse slices (Bushberg, 2002).

The ability to localize tumors and define regions of interest (ROIs) in 3-D is a huge advantage of CT simulation for radiation therapy. For lung cancer, however, respiratory motion remains a huge source of uncertainty for radiotherapy planning, and increasing treatment margins is undesirable due to additional normal tissue that will be irradiated in the process. Furthermore, standard helical CT can induce severe artifacts when imaging thoracic lesions due to respiratory motion (Chen et al., 2004). One proposed solution is “slow” CT scanning, which uses a 4 second gantry rotation to capture breathing motion in one rotation of the x-ray gantry (Lagerwaard et al., 2001). Although the AAPM Task Group 76 report advocates the use of slow scanning (Keall et al., 2006), significant image artifacts can occur due to assumptions made in the filtered back-projection reconstruction process that are violated by the slow scan technique (Bacharach, 2007).

Four-dimensional computed tomography (4D-CT) overcomes these issues by collecting multiple images at a single couch position, thereby capturing different phases of the respiratory cycle (Keall et al., 2004; Low et al., 2003; Pan et al., 2004; Rietzel et al., 2005). In the image-binning approach to 4D-CT reconstruction provided by one commercial vendor (General Electric Healthcare, Waukesha, WI), image acquisition occurs in “cine mode,” in which the couch is stationary and the gantry rotates around the patient continuously acquiring data (Pan et al., 2004; Rietzel et al., 2005). Images are reconstructed at pre-defined intervals and are sorted according to respiratory phase determined by a respiratory surrogate, such as an external monitor of the location of the external patient surface (Real-Time Positioning Management [RPM] system, Varian, Palo Alto, CA). Ten 3-D image sets representing each phase of the respiratory cycle are formed (0% to 90%, where 0% represents end-inspiration and 50% represents end-expiration). The utility of 4D-CT was recognized immediately in the radiation oncology community and several studies have shown the use of 4D-CT in measuring lesion or organ motion (Brandner et al., 2006; Liu et al., 2007) and implementing 4-D treatment planning (Kang et al., 2007; Rietzel et al., 2006; Underberg et al., 2004).

One drawback to treatment planning with 4D-CT is the increased delineation workload. Gross tumor volume (GTV) is defined in the International Commission on Radiation Units and Measurements (ICRU) report 62 as “gross demonstrable extent and location of malignant growth” (International Commission on Radiation Units and Measurements., 1999) and is contoured by the radiation oncologist. For NSCLC, the GTV is expanded with an isotropic margin (barring any anatomical boundaries to extension of gross tumor) to the clinical target volume (CTV), which includes microscopic extension, and expanded again to the internal target volume (ITV) which accounts for physiological motion with the internal margin (International Commission on Radiation Units and Measurements., 1999). One last margin for setup uncertainty expands the ITV to the planning target volume (PTV). ICRU treatment volumes are illustrated in Figure 1.1 (left).

ICRU 62, however, was written in 1999, several years before 4D-CT was commercially available and does not consider the consequences of 4-D imaging. For

example, ITV was originally intended as a generic expansion for physiological motion. Now, it is possible to obtain patient-*specific* motion parameters with 4D-CT, thereby making a generic ITV expansion confusing and obsolete. Strictly interpreted from ICRU guidelines, GTV should be contoured on each phase of 4D-CT, which increases the delineation workload ten-fold.

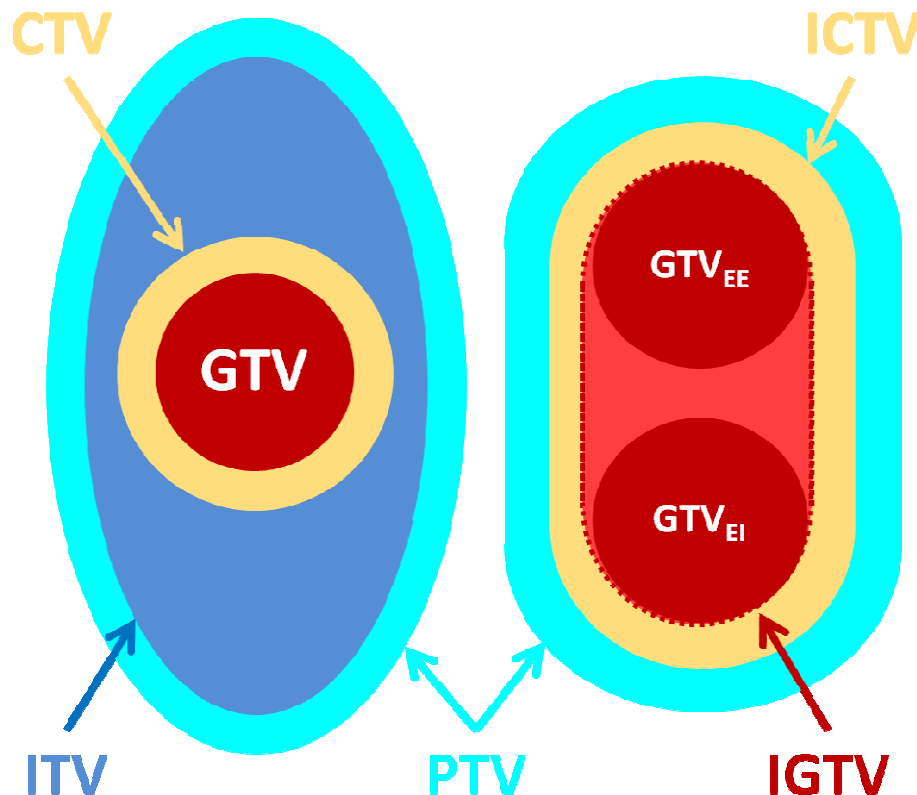


Figure 1.1: Target volumes as described by ICRU 62 (left) and M. D. Anderson convention (right). GTV = gross tumor volume. CTV = clinical target volume. ITV = internal target volume. PTV = planning target volume. IGTV = internal gross tumor volume (dotted line). ICTV = internal clinical target volume. EE = end-expiration. EI = end-inspiration. The M. D. Anderson approach utilizes 4D-CT to define a patient-specific motion path characterized by IGTV.

Various techniques have been investigated to overcome this obstacle, including rigid registration techniques (Ezhil et al., 2009; Liu et al., 2007) and the use of maximum intensity projection (MIP) (Bradley et al., 2006; Keall et al., 2006; Muirhead et al., 2008; Rietzel et al., 2006; Rietzel et al., 2008; Underberg et al., 2005). The MIP is a single 3-D image set

processed from 4D-CT data. Each voxel displays the maximum CT value it encountered throughout the 10 phases of the respiratory cycle. Because of the substantial difference in electron density between the tumor, which is similar to “soft tissue,” and the surrounding lung parenchyma, which is typically about 1/4 the density of soft tissue (Khan, 2003), the MIP, in essence, displays the “motion envelope” of the tumor, a record of everywhere the tumor moves over a respiratory cycle.

Because radiation oncologists typically target the motion envelope of the tumor for radiation therapy (treatment delivery technology is not yet sophisticated enough to reliably track the tumor during treatment, though this is an active area of research (Suh et al., 2009)), various institutions have independently modified ICRU target volume definitions to incorporate 4-D imaging into the simulation procedure. At M. D. Anderson, the *internal* gross tumor volume or “IGTV” has been defined as the motion envelope of the gross tumor which is expanded for microscopic disease to the *internal* clinical target volume (ICTV), illustrated in Figure 1.1 (right). A recent study found that IGTV contoured on MIP was significantly larger than GTV contoured on helical CT, which implies a more “inclusive” method of GTV determination thus less chance of geographic miss (Bradley et al., 2006). Several studies have shown that contouring IGTV with MIP produces volumes similar to the union of 10 phase GTVs from 4D-CT (Park et al., 2009; Rietzel et al., 2005; Rietzel et al., 2008; Underberg et al., 2005), suggesting that MIP could be used to define targets for radiation therapy instead of all 10 phases of 4D-CT.

Similar image processing techniques can be applied to 4D-CT data to produce other useful image sets, such as the minimum intensity projection (min-ip), which displays the minimum voxel value instead of maximum voxel value, and the respiratory-averaged CT (RACT), which is the arithmetic average of the 10 phases of 4D-CT. The RACT appears as a motion-blurred CT image and can be used for dose calculation (Admiraal et al., 2008; Glide-Hurst et al., 2008) and attenuation correction of positron emission tomography (Chi et al., 2007; Pan et al., 2005). Examples of end-inspiration and end-expiration phase images from 4D-CT, as well as MIP and RACT, are shown in Figure 1.2.

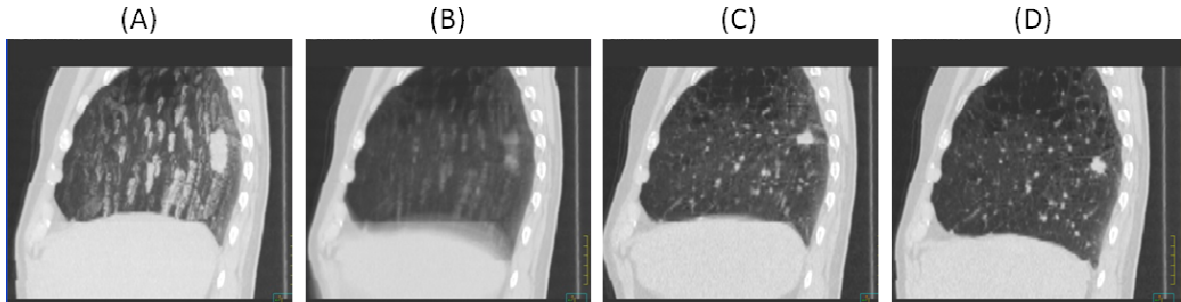


Figure 1.2: (A) maximum intensity projection and (B) respiratory-averaged CT from 4D-CT. End-expiration and end-inspiration, the extremes of respiratory motion, are shown in 4D-CT phase images (C) 50% phase and (D) 0% phase.

Recently, a technique was developed to produce RACT directly from cine CT data for the purpose of attenuation correction of diagnostic thoracic PET/CT for which 4D-CT is not performed (Pan et al., 2006). In this case, RACT is formed by averaging *all* the images at each couch position (between 20-30 images, depending on user-defined parameters) instead of a 10-phase subset as determined by 4D-CT. The same principle can be applied to MIP processing; instead of taking the MIP of the 10 phases of 4D-CT, one can take the MIP of all images reconstructed from the cine acquisition (Figure 1.3). In this work, the image sets from which MIP and RACT are derived are denoted by a subscript. For example, MIP processed from cine CT is “MIP_{cine}.” The advantage of processing directly from cine CT is that 4D-CT is no longer required to form MIP which, according to the studies above, can be used for target definition of the IGTV. This suggests that creating MIP directly from cine CT may be a way to bypass the complex and expensive 4D-CT process but still incorporate substantial motion information into the treatment plan.

A significant drawback of MIP, however, is the lack of contrast when tumors are located near structures of equal or greater density (Bradley et al., 2006; Muirhead et al., 2008; Rietzel et al., 2005; Rietzel et al., 2008; Underberg et al., 2005). Consider, for example, a tumor located just superior to the liver. The liver moves substantially during respiratory motion and can “overwrite” the inferior motion envelope of the tumor, making it nearly impossible to determine the inferior extent of the tumor’s motion (Figure 1.4). Another example of this problem is a tumor adjacent to the chest wall (Figure 1.5).

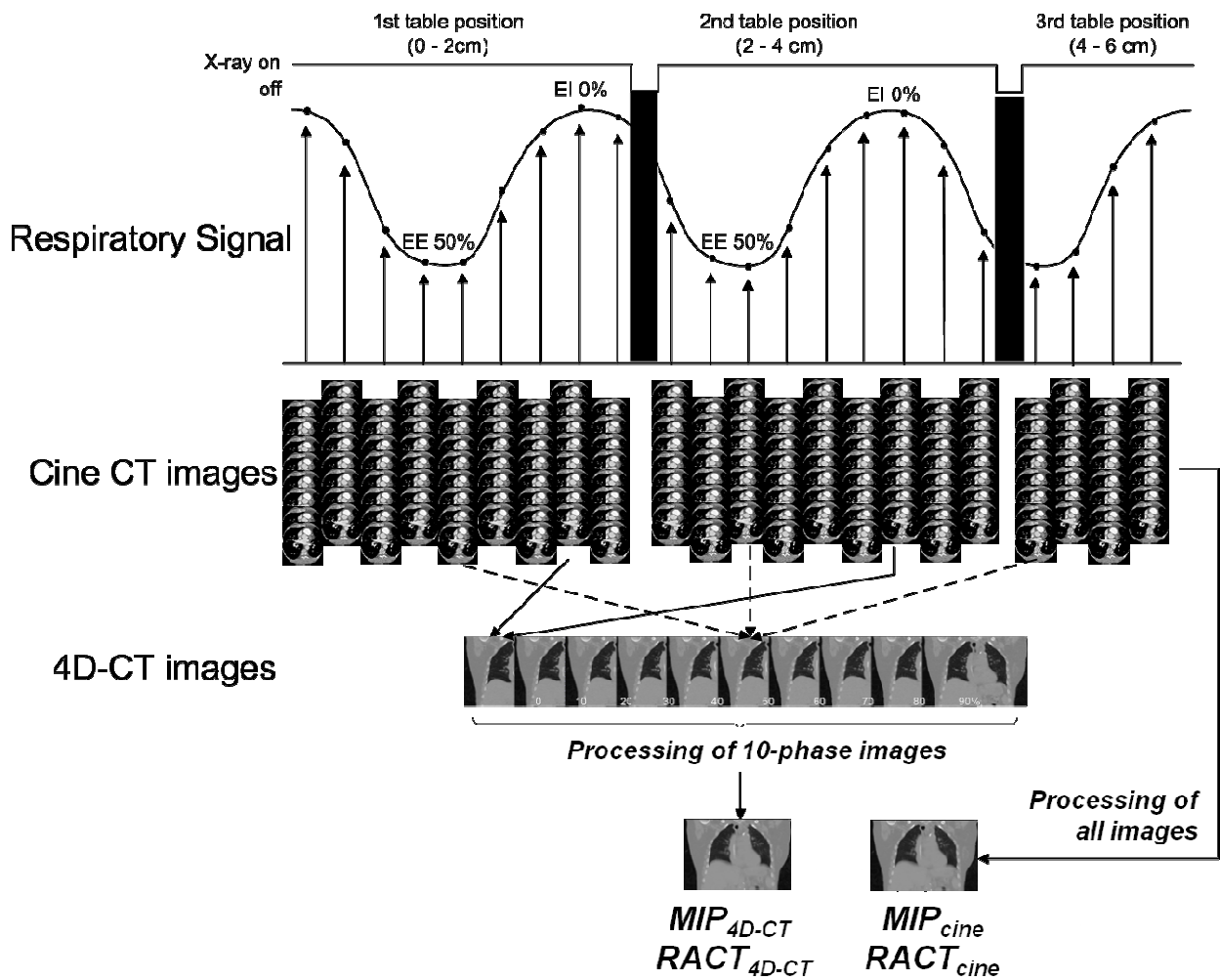


Figure 1.3: Image processing of 4D-CT imaging versus raw cine CT imaging. MIP = maximum intensity projection, RACT = respiration-averaged computed tomography. Reproduced with permission from Riegel *et al.* (Riegel *et al.*, 2009)

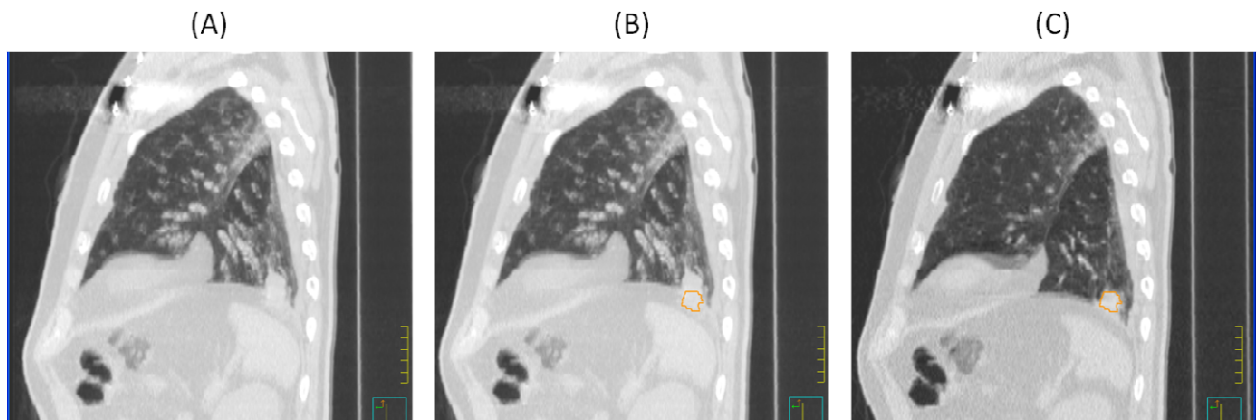


Figure 1.4: Sagittal views of a moving lesion obscured by the liver. (A) MIP without contour. (B) MIP with end-inspiration tumor contour (orange). (C) End-inspiration phase with contour drawn for reference. Note that the inferior border of the tumor is nearly impossible to delineate with the MIP alone.

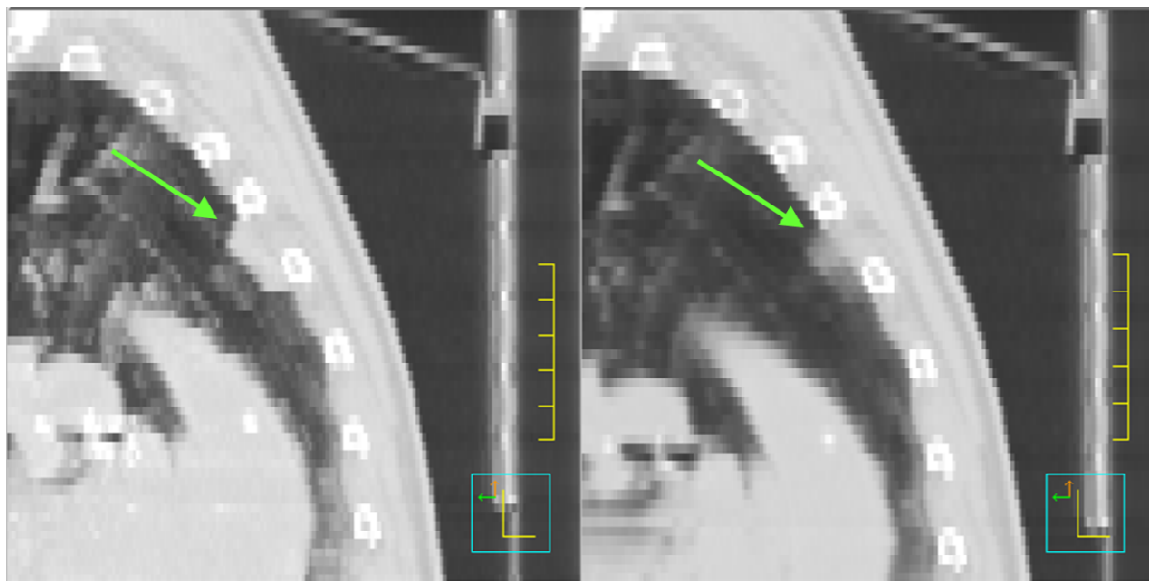


Figure 1.5: Sagittal CT image of tumor near the chest wall. (left) Maximum intensity projection. (right) Respiratory-averaged CT. Reproduced with permission from Riegel *et al.* (Riegel *et al.*, 2009)

It is plausible, however, that additional image sets could be used to supplement MIP_{cine} and provide enough information for accurate target definition. Consider the example of the tumor near the chest wall: The tumor is easily defined in the superior, inferior, and anterior directions on the MIP_{cine} image (Figure 1.5, left), but the contrast is poor in the posterior direction. The $RACT_{\text{cine}}$ image, however, provides good contrast for the posterior extent of the tumor due to a density gradient caused by motion blurring (Figure 1.5, right). Used together, it is feasible that the MIP_{cine} and $RACT_{\text{cine}}$ could be used for IGTV delineation of small, highly mobile tumors (Pan et al., 2007). For larger, more complicated tumors, however, it is likely that cine CT alone will not provide enough information for IGTV delineation. This hypothesis is supported by a result publication by Muirhead *et al.* in which target delineation on MIP_{4D-CT} was compared with 4D-CT phase imaging in patients stratified by lung cancer stage. The authors found that MIP could be reliably substituted for 4D-CT in stage I lesions, but not stage II or III (Muirhead et al., 2008).

Lesion/normal tissue contrast may be enhanced by adding a second imaging modality. The integration of fluorodeoxyglucose positron emission tomography (FDG-PET) into the treatment planning process is another recent development in radiation oncology, facilitated by the hardware fusion of PET/CT scanners. Several studies have analyzed the impact of including PET data in GTV delineation for NSCLC and have yielded noteworthy results, mostly due to the inclusion of lymph nodes and the exclusion of atelectasis (Ashamalla et al., 2005; Bradley et al., 2004; Erdi et al., 2002; Nestle et al., 1999; van Baardwijk et al., 2006).

PET imaging provides quantitative data regarding the metabolic behavior of the patient. In that sense, it is a *functional* imaging modality, as opposed to CT which is a *structural* imaging modality. To acquire a PET scan, a patient is injected with a radiotracer, that is, a compound that follows metabolic pathways but has a radioactive isotope attached to it. In almost all oncological PET imaging, the compound used is fluorodeoxyglucose (FDG). FDG behaves like glucose (except with a radioactive ^{18}F atom attached) and follows the glycolytic pathway until it becomes phosphorylated by hexokinase and becomes trapped in the cell. The ^{18}F nucleus decays to ^{18}O by positron (β^+) decay. The ejected

positron travels a certain distance (the “range” of the positron, which is unique to the isotope and is related to the initial energy of the positron after decay) and undergoes annihilation with an electron, emitting two 511 keV photons at approximately 180° from each other. These photons are detected by a ring of detectors positioned around the patient that discriminate detection events based on energy (a window around 511 keV) and time. Each event is recorded as a line of response, which is placed in a sinogram and is reconstructed using an iterative reconstruction technique such as maximum likelihood expectation maximization (Lange et al., 1984; Shepp et al., 1972) or, more recently, ordered subsets expectation maximization (OSEM) (Hudson et al., 1994).

One advantage of using PET images to delineate that GTV is the application of auto-segmentation techniques. Currently, there is very little guidance on exactly how to incorporate PET information into the delineation process, and, consequently, different physicians can produce different GTVs (Riegel et al., 2006). Auto-segmentation would standardize this process, thereby decreasing interobserver variation and simplifying the delineation process.

Target volume delineation of lung cancer with PET/CT has been extensively reported in the literature (Biehl et al., 2006; Black et al., 2004; Brambilla et al., 2008; Caldwell et al., 2003; Davis et al., 2006; Drever et al., 2007; Erdi et al., 1997; Nestle et al., 2005; Okubo et al., 2008; Park et al., 2008; Paulino et al., 2004), yet little consensus exists on exactly how to use PET to define a GTV (Nestle et al., 2006). Some studies recommend using an absolute SUV threshold such as 2.5 g/mL (Paulino et al., 2004), while others advocate a fixed percentage threshold of maximum activity concentration or standardized uptake value (SUV) (Erdi et al., 1997; Okubo et al., 2008). Biehl *et al.*, however, have shown that a single threshold for all lung lesions is inadequate and recommend thresholds varying from 15% of maximum activity concentration for tumors greater than 5 cm and 42% of maximum activity concentration for tumors less than 3 cm (Biehl et al., 2006). Black *et al.* derived a linear relationship for optimal thresholds from phantom scans as a function of mean SUV, which is, in turn, a function of background activity and target volume (Black et al., 2004). Brambilla *et al.* found that both target size and source-to-background ratio were significant

factors in determining appropriate activity concentration thresholds and recommended that both variables be included in automatic segmentation algorithms (Brambilla et al., 2008). Van Baardwijk *et al.*, by way of thresholds determined by Daisne *et al.* (Daisne et al., 2003), included both variables in their segmentation algorithm, applied the method to patients, and found good correlation with pathological specimens (van Baardwijk et al., 2007).

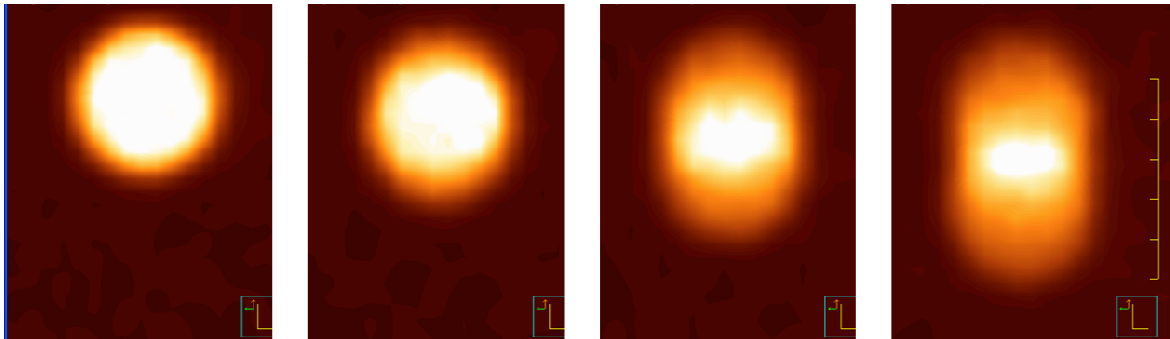


Figure 1.6: PET image of 37 mm diameter sphere moving at 0, 10, 20, and 30 mm sinusoidal motion.

One significant variable that most of these studies ignore is motion. Because PET acquisition occurs over several minutes to accumulate coincidence events, the effect of respiratory motion on PET imaging is a blurring of the tumor: Activity is spread out over voxels in the motion path of the tumor (Figure 1.6) which can lead to inaccurate quantification (Boucher et al., 2004) and exaggerated tumor geometry (Okubo et al., 2008). The aforementioned segmentation studies focused either on stationary objects in a phantom or moving objects in PET compared with a free-breathing or breath-hold CT. Comparison with free-breathing CT will most likely be inaccurate due to the possibility of motion artifacts (Chen et al., 2004), and comparison with breath-hold CT, while accurate, will be inappropriate because, typically, a breath-hold CT is not used for treatment planning when 4D-CT is available. Recall that 4D-CT is used in radiation therapy planning of moving lung lesions to define the IGTV, the motion envelope of the tumor.

It seems logical, then, to compare PET to 4D-CT to determine an optimal segmentation method. Caldwell *et al.* found that PET could indeed be used to determine IGTV for radiation therapy planning but that, as a result of their moving phantom study, conventional threshold values (acquired at rest) produced volumes that were too small. They reduced the threshold to 15% of maximum activity concentration to adequately capture what the authors called “ITV” (Caldwell et al., 2003). Similarly, Yaremko *et al.* found that hot spheres moving in air required a reduced threshold (25%) to capture the IGTV (Yaremko et al., 2005). To date, however, there have not been studies optimizing activity concentration thresholds using 4D-CT as the reference for phantoms or patients, though some of the aforementioned segmentation studies have called for just such an investigation (Biehl et al., 2006; Okubo et al., 2008).

If a robust segmentation protocol could be developed for moving lung tumors, then radiation oncologists could apply such a protocol to radiation therapy treatment planning with the confidence that PET is providing accurate targeting information. Recall that the main drawback with target delineation using MIP_{cine} and $RACT_{\text{cine}}$ was the lack of contrast for tumors with complicated structure. By using cine CT image sets and PET together (utilizing the segmentation protocol), there may be enough information for target delineation and treatment planning.

The purpose of this dissertation was to develop a treatment planning technique using image sets processed from cine CT in conjunction with PET imaging as a substitute for 4D-CT. The work is split into 4 chapters: First, we examined the use of MIP_{cine} and $RACT_{\text{cine}}$ for the purpose of contouring stage I NSCLC; second, we examined the use of $RACT_{\text{cine}}$ for dose calculation; third, we developed a threshold-based auto-segmentation model to accurately contour moving lung tumors; finally, we assessed the feasibility of using cine CT image sets and the PET auto-segmentation algorithm together to contour stage III NSCLC.

If successful, thoracic radiotherapy treatment planning with cine PET/CT may rival conventional 4D-CT plans at a fraction of the cost, thereby enabling small, local treatment centers to provide motion-encompassing treatment plans to lung cancer patients.

1.3 Summary of Chapters

1.3.1 Chapter 2: Target Delineation of Stage I Non-Small Cell Lung Cancer with Cine CT

Early-stage lung tumors are often small, well-defined, and can be very mobile. Our first task was to use MIP_{cine} and $RACT_{cine}$ to contour early stage lung cancer for group of patients slated for stereotactic body radiation therapy (SBRT). The purpose was to determine if target definition with MIP_{cine} and $RACT_{cine}$ was similar to target definition with 4D-CT. Chapter 2 was split into 2 parts: The phantom study and the patient study. Phantoms were used to assess differences between cine CT and 4D-CT in a controlled environment and patients were used for clinical significance.

In the phantom study, a body phantom with 6 spheres was placed on a motion platform and moved in an irregular respiratory pattern while cine CT was acquired. MIP_{cine} and MIP_{4D-CT} were formed and auto-segmented in a treatment planning system for volume comparison. In the patient study, cine CT images obtained during treatment simulation were used to form MIP_{cine} and $RACT_{cine}$ image sets. These image sets then were used together to define IGTVs. Patients were included if tumor motion was greater than 1 cm. Lesions were contoured first using MIP_{cine} and $RACT_{cine}$, then with MIP_{4D-CT} along with 10-phase image sets. Mean ratios of volume magnitude were compared with intraobserver variation, the variation expected by a physician contouring the same region multiple times. Mean shifts in centroid location were calculated, and volume overlap was assessed with the normalized Dice similarity coefficient index.

The patient studies demonstrated that IGTV defined on cine imaging was similar to or slightly larger than IGTV defined on 4D-CT. Phantom studies of irregular motion confirmed that IGTV defined on cine CT imaging was indeed larger and therefore more accurately captured the maximum motion extent of irregular respiration.

1.3.2 Chapter 3: Dose Calculation with Cine Respiratory-Averaged CT

Dose calculation for thoracic radiotherapy is commonly performed on a free-breathing helical CT despite artifacts caused by respiratory motion. Some centers now use $RACT_{4D-CT}$, the pixel-by-pixel average of the 10 phases of 4D-CT, for dose calculation. $RACT_{cine}$, however, may be a means to incorporate motion information into dose calculation without performing 4D-CT. The purpose of this chapter was to determine if $RACT_{cine}$ could be substituted for $RACT_{4D-CT}$ for the purposes of dose calculation, and if increasing the cine duration can decrease differences between the dose distributions. Cine CT data and corresponding 4D-CT simulations for 23 patients with at least 2 breathing cycles per cine duration were retrieved. RACT was generated four ways: (1) from 10 phases of 4D-CT, (2) from 1 breathing cycle of images, (3) from 1.5 breathing cycles of images, and (4) from 2 breathing cycles of images. The clinical treatment plan was transferred to each RACT and dose was recalculated. Planar dose distributions were exported on orthogonal planes through the isocenter (coronal, sagittal, and transverse orientations). The resulting dose distributions were compared using the gamma (γ) index within the planning target volume (PTV). Failure criteria were set to 2%/1mm. A follow-up study with 50 additional lung cancer patients was performed to increase sample size. The same dose recalculation and analysis was performed.

In the primary patient group, 22 of 23 patients had 100% of points within the PTV pass γ criteria. The average maximum and mean γ indices were very low (well below 1), indicating good agreement between dose distributions. Increasing the cine duration generally increased the dose agreement. In the follow-up study, 49 of 50 patients had 100% of points within the PTV pass the γ criteria. The average maximum and mean γ indices were again well below 1, indicating good agreement. Dose calculation on $RACT_{cine}$ is negligibly different from dose calculation on $RACT_{4D-CT}$. Differences can be decreased further by increasing the cine duration of the cine CT scan.

1.3.3 Chapter 4: Segmentation of Moving Targets with PET/CT: Correlation of Thresholds with Lesion Size, Motion Extent, and Source-to-Background Ratio

Several studies consider size and source-to-background ratio (SBR) in their automatic segmentation methods but neglect respiratory motion. The purpose of this chapter was to model the relationship between optimal activity concentration threshold, tumor volume, motion extent, and SBR using multiple regression techniques. An extensive series of phantom scans simulating tumors of varying size, SBR, and motion amplitudes was performed. Regions of interest delineated on PET were compared with the “motion envelope” of the moving sphere defined on cine CT.

A NEMA IEC thorax phantom containing 6 spheres of inner diameters 10, 13, 17, 22, 28, 37 mm was filled to 6 SBRs (5:1, 10:1, 15:1, 20:1, 30:1, 50:1) and was placed on a motion platform and moved sinusoidally at 0, 5, 10, 15, 20, 25, 30 mm amplitudes (252 combinations of experimental parameters). PET images were acquired for 18 minutes and split into three 6-minute acquisitions to assess reproducibility. The spheres (blurred on PET images due to motion) were segmented at 1% intervals of maximum activity concentration. The optimal threshold was determined by comparing threshold volume surfaces with a reference volume surface defined on cine CT. Optimal activity concentration thresholds were normalized to background and multiple regression was used to determine the relationship between optimal threshold, volume, motion, and SBR. Standardized regression coefficients were used to assess the relative influence of each variable.

The model was validated using patient data. PET and 4D-CT were performed in the same imaging session for 23 patients (24 tumors) for radiation therapy planning. IGTVs were segmented on MIP_{cine} and activity concentration thresholds which best matched were determined. IGTVs were delineated on PET imaging using our segmentation model and following methods for comparison: 15%, 35%, and 42% of maximum activity concentration, SUV of 2.5 g/mL, 15% of mean activity concentration plus background, a linear function of mean SUV, and our motion-inclusive model derived from phantom scans. Threshold values produced from each method were correlated with best-matched threshold values. PET

target volumes were geometrically compared to cine CT target volumes using volume magnitude and surface separation.

The resulting model and coefficients provided a functional form that fit the phantom data with an adjusted $R^2 = 0.96$. The most significant contributor to threshold level was SBR. Our technique yielded threshold values well-correlated with measured optimal thresholds (slope = 0.8991, $R^2 = 0.8577$) and produced PET to CT volume differences smaller than the 6 other methods (-5.15%) and surface separation smaller than 5 other methods (1.6 mm). IGTVs at 35% and 42% maximum activity concentration substantially underestimated the motion envelope of the tumor in most patients.

1.3.4 Chapter 5: Target Delineation of Stage III Non-Small Cell Lung Cancer with Cine PET/CT

The segmentation model developed in Chapter 4 was applied to 5 patients with NSCLC: 4 patients with stage III disease, 1 with stage I disease. Feasibility of using the PET segmentation model in conjunction with MIP_{cine} was assessed qualitatively. The segmentation model produced reasonable target volumes for 3 of 5 patients. Tumors of 2 patients, however, were not delineated accurately. Further research is required for this application of the segmentation model. Accounting for nodal involvement was not investigated in this chapter but is critical for accurate segmentation of stage III NSCLC and therefore should be explored in the future.

1.3.5 Chapters 6 and 7: Discussion and Conclusions

Results from Chapters 2, 3, 4, and 5 are discussed in the context of the cine PET/CT workflow. Recommendations are made based on experimental results.

Chapter 2 TARGET DELINEATION OF STAGE I NON-SMALL CELL LUNG CANCER WITH CINE CT

2.1 Introduction

Radiation therapy is an important treatment option for stage I NSCLC. Though surgery is still the standard of care, stereotactic body radiation therapy (SBRT) has been shown to be as effective as resection for inoperable stage I NSCLC (Chang et al., 2007; Timmerman et al., 2007) and multicenter clinical trials are underway to assess the efficacy of SBRT in operable NSCLC. In contrast with conventionally-fractionated radiation therapy, SBRT utilizes a hypofractionated approach. At M. D. Anderson, for example, the tumor receives 60 Gy in 4 fractions, or 15 Gy per fraction, as compared with 66 Gy in 2 Gy fractions in conventional radiation therapy. Beyond the convenience of four-fraction treatment for the patient, the combination of hypofractionation, multiple fields, and image guidance allows higher ablative doses to be delivered to the tumor while keeping normal tissue toxicity at an acceptable level (Timmerman et al., 2007). High doses per fraction, however, mean that accuracy becomes even more critical to avoid geometric miss.

To account for respiratory motion in the SBRT treatment plan, a 4D-CT exam is used to image 10 phases of the patient's respiratory cycle and target the motion path of the tumor. Earlier, the complexity and cost of 4D-CT was briefly described. The 4D-CT imaging process is explained here in more detail to highlight the differences between the conventional 4D-CT approach and the cine CT approach.

The scanner setup is slightly different for 4D-CT simulation than for standard helical CT simulation. In addition to the flat table-top and wing board, the patient's respiration is monitored and recorded (Real-Time Positioning Management, Varian, Palo Alto, CA). The system consists of an infrared camera and a CCD detector docked on the end of the couch and a small plastic box with two reflective markers which is placed on the patient's abdomen (Figure 2.1). The box acts as the surrogate for the patient's respiratory pattern, moving up and down with each inhalation and exhalation of breath.

For GE CT scanners, images are acquired in “cine” mode in which the couch is stationary, and the x-ray tube rotates around the patient multiple times acquiring a continuous stream of projection data. After enough data has been collected, the beam is turned off and the couch moves to the next bed position and acquisition begins again.

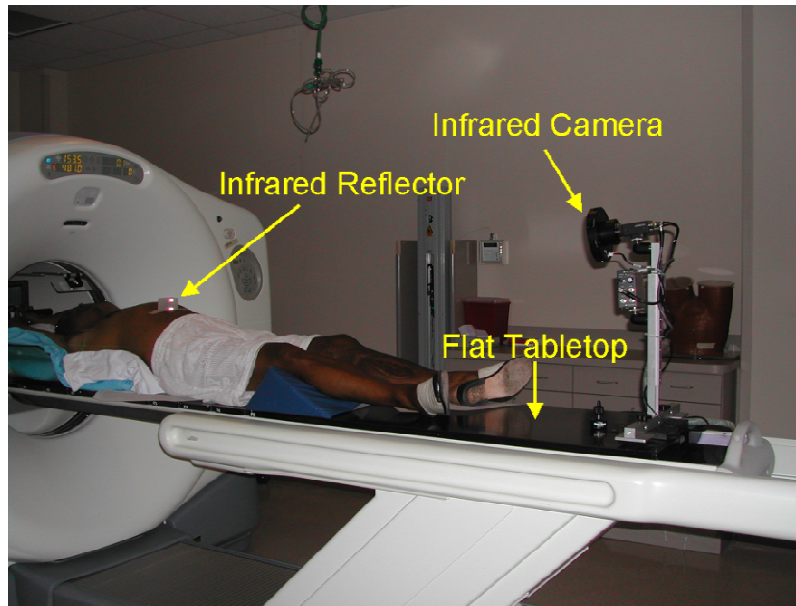


Figure 2.1: Respiratory surrogate setup for 4D-CT acquisition. The infrared camera tracks the movement of the infrared reflector on the patient’s abdomen to record the respiratory motion trace.

Several user parameters define the cine acquisition. Gantry rotation “speed” (typically quoted as the gantry rotation period) typically runs between 0.3 s and 1 s depending on the scanner model. The cine duration (CD) is the amount of time projections are acquired at each bed position, in other words, the “beam on” time. Typically, the CD is chosen to reflect the average breathing period of the patient plus one second to ensure that a complete set of projections exists for reconstruction at the beginning and end of cine acquisition (Pan et al., 2004). Because cine data is a long stream of projection data, the user must define how the stream will be split into reconstructed images (i.e. which projections belong to which reconstruction). The cine interval (CI) defines the temporal separation between adjacent image reconstructions. The cine interval need not be limited by gantry rotation speed (one projection per one gantry rotation); projections can be used in multiple

image reconstructions to produce finer temporal sampling. In clinical practice, this is often the case. Typical CI's range from 0.2 to 0.3 s with a gantry speed of 0.5 s. When the CI is finer than the gantry rotation speed, projection data is used redundantly in adjacent images. The trade-off to finer temporal sampling, however, is an increased number of images. Typically, 10-30 images are reconstructed per cine duration. To scan 20-25 cm of anatomy with 2.5 mm slice thickness, 2400-3000 images are generated. Currently, the number of images generated from cine acquisition is limited to 3000 due to reconstruction time and storage limitations.

This large set of images is commonly referred to as "cine CT." Each image captures a distinct moment in time and space like a frame in a movie reel. It is at this point where our experimental method detours from the conventional 4D-CT technique. The experimental method will be discussed shortly.

Because of the time required to move the couch from one position to the next, the series of cine CT images captures a different starting phase of the breathing cycle each time. This effect is demonstrated in Figure 1.3. Reconstructing 3-D image sets based on image number, then, would be non-sensical (image 1 of couch position 1 does not match the same part of the respiratory cycle of image 1 of couch position 2.) Irregular respiration further complicates this problem. The cine CT images must therefore be sorted into different respiratory states and then combined to form 3-D image sets for each respiratory state. The respiratory state is provided by the trace recorded by the respiratory monitoring device. Typically, the respiratory cycle is divided into 10 equidistant phase-bins from one inspiration to the next. Proprietary software is used to match cine CT images with their appropriate phase by examining the midscan time of each cine CT image and comparing it with the respiratory trace. The result is 10 3-D image sets, each one representing a different phase of respiration (hence the term "4D-CT").

As described in section 1.2, contouring the tumor on 4D-CT is time-consuming and labor-intensive. The maximum intensity projection (MIP) is often used to display the "motion envelope" of the tumor in a single image set. Several studies have shown that target delineation on MIP is similar to target delineation on 4D-CT (Rietzel et al., 2005;

Rietzel et al., 2008; Underberg et al., 2005). Clinically, at M. D. Anderson, MIP_{4D-CT} and 4D-CT phase images are used together to define the tumor and its motion extent (Ezhil et al., 2009).

Recall that our experimental method deviates from 4D-CT acquisition at the series of cine CT images, just before the sorting into phase bins. We have developed software to create MIP directly from the cine CT images, bypassing the sorting process of 4D-CT (Pan et al., 2007). The differences between the 4D-CT approach to MIP and cine CT approach to MIP are shown diagrammatically in Figure 1.3. As described in the background and significance section, this could eliminate significant costs of 4D-CT simulation while still providing useful motion information for planning purposes.

2.2 Purpose

In this chapter, we compared two methods of IGTV segmentation on highly mobile early stage lung tumors: First, the conventional 4D-CT approach utilizing phase imaging from 4D-CT and MIP processed from 4D-CT and second, the experimental “cine CT” approach utilizing MIP_{cine} and RACT_{cine}. The goal of this chapter was to show that the experimental method can produce target volumes similar to the conventional 4D-CT method.

2.3 Methods

2.3.1 Phantom Study

Because 4D-CT is essentially a subset of cine CT, we anticipated that generating a MIP from 10 phase image sets would yield a target volume different from a MIP generated from all images captured during the cine duration (20-30 images) when the motion is irregular, which is usually the case with patient scanning. The objective of the phantom study was to show that MIP_{cine} visualized the full extent of irregular motion more precisely

than MIP_{4D-CT} . In other words, we wanted to demonstrate that volumes segmented on MIP_{cine} were larger than those from MIP_{4D-CT} .

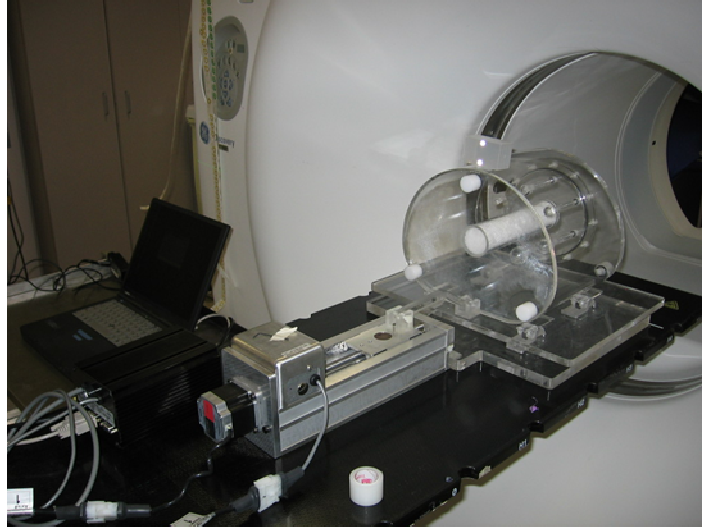


Figure 2.2: NEMA IEC thorax phantom (Data Spectrum, Chapel Hill, NC) placed on a motion platform driven by a single-axis stepper motor (Velmex Inc., Bloomfield, NY). Note the RPM block placed on the phantom.

A body phantom made in accordance with National Electrical Manufacturers Association (NEMA) and International Electrotechnical Commission (IEC) recommendations was used (Data Spectrum, Chapel Hill, NC). The phantom contained 6 water-filled spheres was scanned using a cine CT protocol on a PET/CT scanner (Discovery ST, General Electric Healthcare, Waukesha, WI), the CT portion of which is an 8-slice scanner. The background tank was filled with air. The phantom was placed on a platform and moved one-dimensionally, driven by a single-axis stepper motor (Velmex Inc., Bloomfield, NY). Experimental setup is shown in Figure 2.2. The irregular motion (previously described in Starkschall *et al.* (Starkschall et al., 2007)) was nearly sinusoidal with amplitude and frequency respectively varying from 0.7 to 1.1 cm and 15 to 20 cycles per minute. The following cine scan protocol was repeated 10 times on the moving phantom: 120 kV, 50 mA, 2.5 mm slice thickness, gantry rotation of 0.5 s, cine interval of 0.2 s, cine duration of 7.5 s (twice the average breathing cycle of the irregular pattern plus one gantry rotation).

Images were reconstructed with filtered backprojection (Brooks et al., 1975) to a 512 by 512 image matrix with 50 cm field of view (FOV). MIP_{4D-CT} and MIP_{cine} were reconstructed.

Images were transferred to a commercial radiation treatment planning system (Pinnacle³, version 7.6, Philips Medical Systems, Madison, WI) for contouring and a -700 Hounsfield unit (HU) threshold was used to segment IGTVs on MIP_{cine} and MIP_{4D-CT} image sets (denoted $IGTV_{cine}$ and $IGTV_{4D-CT}$ respectively). Volume measurements were recorded for each of the 6 spheres on the 10 scans, and a paired *t*-test was used to measure statistically significant differences between the mean volume magnitudes of $IGTV_{4D-CT}$ and $IGTV_{cine}$.

2.3.2 Patient Study

We reviewed the radiation oncology patient database at M. D. Anderson to identify patients with stage I NSCLC who had been treated with SBRT, received 4D-CT simulation, and had tumor motion extent greater than 1 cm. Between January of 2005 and April of 2007, 26 patients (27 tumors) fit the criteria. The study protocol was DR07-0809, approved by the institutional review board (IRB). We determined the extent of tumor motion by visually assessing the displacement between extreme phases of the 4D-CT (usually 0% and 50%). Motion extent greater than 1 cm was included because this feature represents the “worst case” scenario for motion artifact. According to Liu *et al.*, approximately 10% of stage I and stage III tumors move more than 1 cm (Liu et al., 2007). If target delineation on cine CT is similar to 4D-CT for the larger motions, the method demonstrated in this study could easily be applied to scenarios where motion is less severe.

Patients were divided into two groups: 12 patients were in the “high contrast” group (13 tumors), with lesions in the middle of the lung parenchyma, and 14 were in the “low contrast” group, with lesions adjacent to structures of equal or higher density. Patients were separated in this fashion to reflect the concerns of previous studies that the MIP does not provide enough contrast to determine the tumor edges when the target is adjacent to dense structures (Rietzel et al., 2005; Underberg et al., 2005). Furthermore, we

did not want the success of segmentation in the high-contrast cases to blur statistically significant differences from the low-contrast cases.

In the course of 4D-CT simulation, each patient received a cine CT scan during which the patient's respiratory signal was acquired. Two sets of images were reconstructed: 4D-CT images derived from the 10 phase images and produced by the proprietary 4D-CT software, and processed images from cine CT. 4D-CT images included 10 phase images, MIP_{4D-CT} , and $RACT_{4D-CT}$. Cine CT images included MIP_{cine} and $RACT_{cine}$ and were produced directly from the cine CT images using in-house software (Pan et al., 2007). All cine scans were performed at 120 kV and 100 mA, with the exception of two patients, whose scans were performed at 150 mA and 80 mA. Gantry rotation period for all patients was 0.5 s.

First, IGTV was auto-segmented on MIP_{cine} and MIP_{4D-CT} for 11 high-contrast lesions that were not adjacent to dense structures. A seed-based region-growing algorithm in the treatment planning software was used for contouring. It should be noted, however, that, although the treatment planning software documentation defines the algorithm as "region growing," the technique differs from conventionally-defined region growing. Typically, region growing occurs on a pixel-by-pixel basis radiating outwards from the seed point until a threshold is reached (Beutel, 2000). Region growing in the treatment planning system occurs by searching pixels to the right of the seed point until a threshold is reached, and the closed boundary around the structure is contoured. The resulting contours were compared with a paired *t*-test to investigate patient contouring while minimizing the influence of a human observer.

One radiation oncologist who specialized in thoracic SBRT delineated the tumors for all patients using the commercial radiation treatment planning system. The radiation oncologist first contoured $IGTV_{cine}$ in all patients from high- and low-contrast tumor groups using MIP_{cine} and $RACT_{cine}$ concurrently. Then, the radiation oncologist contoured $IGTV_{4D-CT}$ according to the current M. D. Anderson clinical protocol: MIP_{4D-CT} was used to outline an IGTV and this volume was then edited based on the 4D-CT phase images. All contours were drawn using the "lung" window/level.

2.3.3 Analysis

For the phantom study, mean volume magnitudes were compared with a paired t-test to assess observer-independent differences in contouring on cine and 4D-CT image sets ($\alpha = 0.05$).

For the patient study, auto-segmented IGTVs were compared with a paired t-test ($\alpha = 0.05$). Physician-drawn $IGTV_{4D-CT}$ and $IGTV_{cine}$ volume magnitudes were compared statistically by taking the ratio of the volume magnitudes and constructing 95% confidence intervals around the mean ratio and comparing these confidence intervals to the intraobserver variation. Three lesions in the high contrast group and 3 lesions in the low contrast group were re-contoured on 4D-CT phase imaging by the radiation oncologist at least 2 months after initial contouring. Resulting IGTVs were compared with initial 4D-CT results and the average percent differences represented the intraobserver variation for each group. Difference in centroid location between $IGTV_{4D-CT}$ and $IGTV_{cine}$ was compared statistically using a log-normal distribution. 95% confidence intervals were constructed around the mean centroid shift (geometric mean was used with the logarithmic transformation) to assess the variability of centroid shift.

Volume overlap was assessed with the Dice Similarity Coefficient index (DSC), which is a measure of the degree of overlap between two areas or volumes (Dice, 1945; Zou et al., 2004). If A is a “reference” volume and B is a “test” volume to be compared to the reference,

$$DSC(A, B) = \frac{2 \times |A \cap B|}{|A| + |B|} \quad (1)$$

Though the DSC is similar to the concordance index in that small changes in volume yield large changes in DSC when the volumes analyzed are small, the DSC is normalized to the sum of the two volumes rather than the union (Giraud et al., 2002). As with any manual segmentation, some uncertainty exists in the tumor delineation. By normalizing the DSC, we take both volume size and segmentation uncertainty into account by dividing the DSC in

equation (1) by an “uncertainty index” (UI). UI is defined as the DSC of the reference volume with the reference volume contracted by 1 mm (A_{-1}). This value was chosen because it reflects the width of one CT pixel in the transverse plane using a 50 cm FOV and 512 by 512 image matrix (which is the typical protocol for CT simulation at M. D. Anderson). The normalized DSC (NDSC), therefore, was given by

$$NDSC(A, B) = \frac{DSC(A, B)}{UI(A)} = \frac{\frac{2 \times |A \cap B|}{|A| + |B|}}{\frac{2 \times |A \cap A_{-1}|}{|A| + |A_{-1}|}} \quad (2)$$

It is helpful to consider the limiting cases when interpreting this index. Higher DSCs mean greater agreement between the experimental and reference volumes. If the NDSC is greater than 1, the DSC of the experimental-to-reference volumes is greater than the uncertainty index, implying that the volumes agreed to less than 1 mm uncertainty. In the current study, the reference volume was $IGTV_{4D-CT}$ and the comparison volume was $IGTV_{cine}$.

2.4 Results

2.4.1 Phantom Study

Ten sets of $IGTV_{cine}$ and $IGTV_{4D-CT}$ auto-segmented at a -700 HU threshold on MIP_{cine} and MIP_{4D-CT} image sets respectively were compared with a paired *t*-test. For all 6 spheres in the phantom, the $IGTV_{cine}$ was significantly larger than $IGTV_{4D-CT}$ (Table 2.1). Most differences between $IGTV_{cine}$ and $IGTV_{4D-CT}$ occurred in the most superior and inferior slices of the motion envelope and, by visual inspection, were not caused by in-slice motion artifact (the spiral patterns often seen when the sphere is present in some projections but not others were not present). This suggests that the larger $IGTV_{cine}$ better captured the full extent of motion because MIP_{cine} included images in the maximum intensity processing which were not present in the 4D-CT. Processing from cine CT, therefore, more accurately

captures the extremes of a naturally varying waveform because more samples of the waveform are included.

Table 2.1: Significance values for phantom study

Sphere Diameter (cm)	MIP _{4D-CT} (cm ³)		MIP _{cine} (cm ³)		<i>p</i>
	Mean Volume	Standard Deviation	Mean Volume	Standard Deviation	
3.7	49.8	0.8	51.0	1.1	<0.01
2.8	24.9	0.5	25.7	0.8	<0.01
2.2	13.7	0.3	14.1	0.4	0.02
1.7	7.9	0.2	8.2	0.3	<0.01
1.3	4.4	0.2	4.6	0.2	0.04
1.0	2.5	0.1	2.7	0.1	0.01

MIP = maximum intensity projection

2.4.2 Patient Study

For the auto-segmented volumes of 11 high-contrast lesions, the IGTV_{cine} was significantly larger than IGTV_{4D-CT} ($p=0.02$). These results are consistent with the phantom results of section 2.4.1.

Table 2.2 and Table 2.3 list IGTV_{cine} and IGTV_{4D-CT} measurements and IGTV_{cine}/IGTV_{4D-CT} ratios of manually segmented volumes for the high- and low-contrast patient groups respectively. IGTV_{cine} and IGTV_{4D-CT} volumes were not significantly different (as found by a paired *t*-test) in patients with high-contrast tumors ($p=0.32$) or patients with low-contrast tumors ($p=0.29$). Comparisons of mean IGTV ratios with intraobserver variation for high-contrast and low-contrast patient groups are shown in Figure 2.3. The 95% confidence intervals of the low-contrast group indicate the variation between contouring on cine CT and 4D-CT was within measured intraobserver variation ($p<0.05$) (Feng et al., 2006). Interestingly, for the high-contrast group, the distribution was shifted slightly higher, implying IGTV_{cine} was slightly larger than IGTV_{4D-CT}. This is, however, consistent with our phantom and patient auto-segmentation results shown above. Mean centroid shift was 0.9 mm for the high-contrast group and 1.4 mm for the low-contrast

group. The upper 95% confidence interval was 1.5 mm and 2.0 mm for high- and low-contrast lesions respectively, indicating that cine CT produces volumes positioned similarly to those drawn on 4D-CT in high- and low-contrast scenarios.

Table 2.2: Internal gross tumor volume (IGTV) measurements for high-contrast patients.

Patient #	IGTV _{cine} (cm ³)	IGTV _{4D-CT} (cm ³)	Ratio	DSC	NDSC
1	12.6	9.8	1.28	0.83	0.95
2	11.0	12.6	0.87	0.84	0.98
3	4.8	3.9	1.26	0.78	0.96
4	6.6	6.7	1.00	0.90	1.07
5	15.2	13.8	1.10	0.90	1.01
6	4.3	3.6	1.20	0.81	1.05
7	2.9	2.8	1.04	0.78	0.98
8	11.5	11.2	1.02	0.88	1.02
9*	2.0	2.1	0.94	0.75	0.97
10*	15.1	13.8	1.09	0.86	0.99
11	2.9	2.9	0.99	0.81	0.99
12	6.1	7.3	0.83	0.84	0.97
13	18.6	18.8	0.99	0.87	0.96
Average	8.7	8.4	1.05	0.84	0.99
SD	5.5	5.4	0.14	0.05	0.04
CI95			±0.08		
CI90			±0.07		

Asterisks (*) indicate bisynchronous lesions.

SD = standard deviation

CI95 = 95% confidence interval

CI90 = 90% confidence interval

Table 2.3: Internal gross tumor volume (IGTV) measurements for low-contrast patients.

Patient #	IGTV_{cine} (cm³)	IGTV_{4D-CT} (cm³)	Ratio	DSC	NDSC
14	5.0	5.8	0.86	0.84	0.99
15	12.1	11.7	1.04	0.85	0.99
16	21.6	20.2	1.07	0.85	0.95
17	4.1	4.1	0.99	0.82	0.97
18	5.8	6.8	0.84	0.79	0.93
19	8.1	7.9	1.03	0.86	0.98
20	3.0	3.3	0.90	0.74	0.96
21	2.4	2.5	0.97	0.86	1.08
22	22.4	27.1	0.83	0.83	0.92
23	14.0	15.4	0.91	0.88	1.01
24	14.8	15.8	0.93	0.84	0.95
25	38.1	37.5	1.02	0.88	0.97
26	22.1	24.2	0.91	0.82	0.91
27	8.5	6.4	1.33	0.84	0.97
Average	13.1	13.5	0.97	0.84	0.97
SD	10.1	10.5	0.13	0.04	0.04
CI95			±0.07		
CI90			±0.06		

SD = standard deviation

CI95 = 95% confidence interval

CI90 = 90% confidence interval

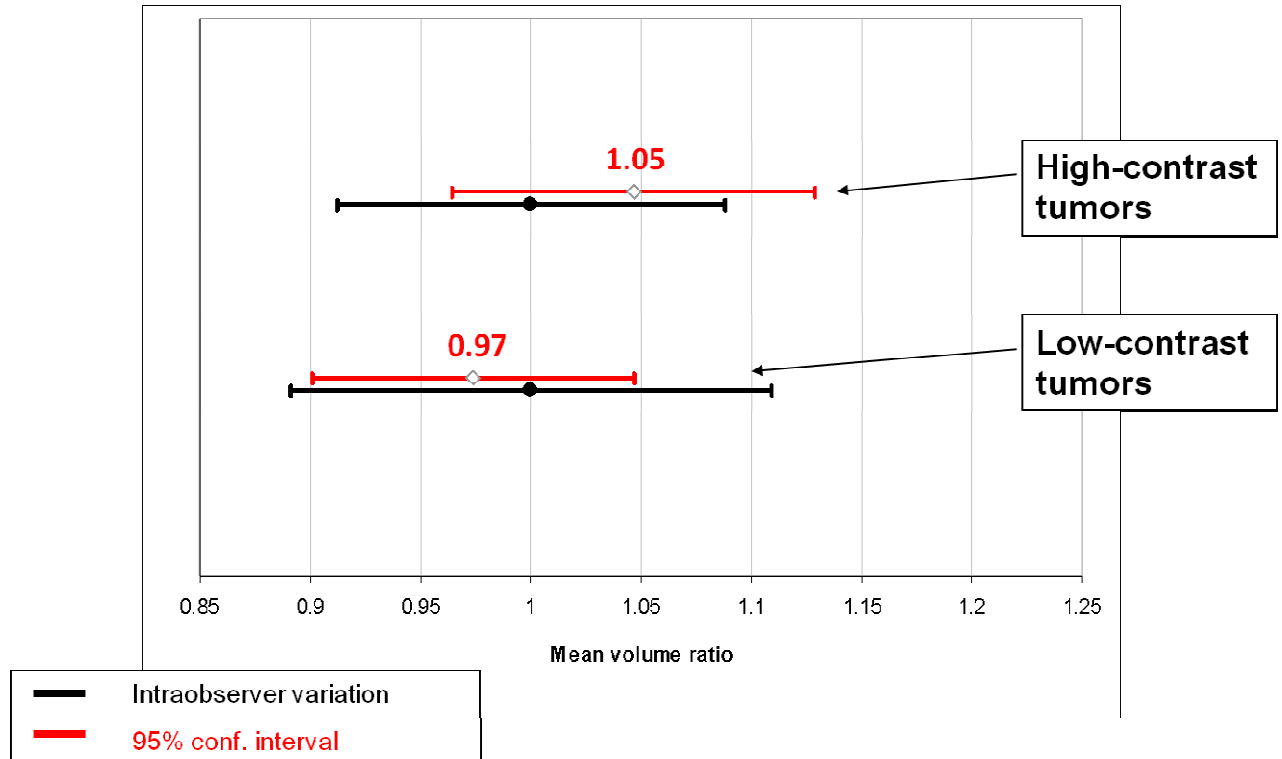


Figure 2.3: Mean volume magnitudes for high and low contrast tumors. Red error bars are the 95% confidence interval around the mean. Black error bars represent mean intraobserver variation for 3 re-contoured patients. Reproduced with permission from Riegel *et al.* (Riegel *et al.*, 2009)

Table 2.2 and Table 2.3 list results of the DSC analyses for high- and low-contrast groups respectively. DSCs were well over 0.7, which is considered good overlap (Bartko, 1991; Zou *et al.*, 2004). The mean NDSC for high-contrast tumors was 0.99. The mean NDSC for low-contrast tumors was 0.97. Because both values are slightly less than 1, this implies that the volumes were slightly below the threshold for agreement within 1 mm uncertainty.

Examples of low-contrast tumors are shown in Figure 1.5 and Figure 2.4. In Figure 1.5, as previously described in section 1.2, the lung tumor is positioned adjacent to the chest wall and the anterior, superior, and inferior edges of the tumor that border the lung are clearly defined on the MIP_{cine} . The posterior edge, however, is adjacent to the higher-density chest wall and the border is difficult to discern. By using the $RACT_{cine}$ to provide additional information, however, the edges become much more apparent; the degraded

density of the $RACT_{cine}$ provides contrast to define the posterior border. In Figure 2.4, the liver obscures the lesion on the transverse MIP_{cine} , but the $RACT_{cine}$ reveals the transverse extent of the tumor.

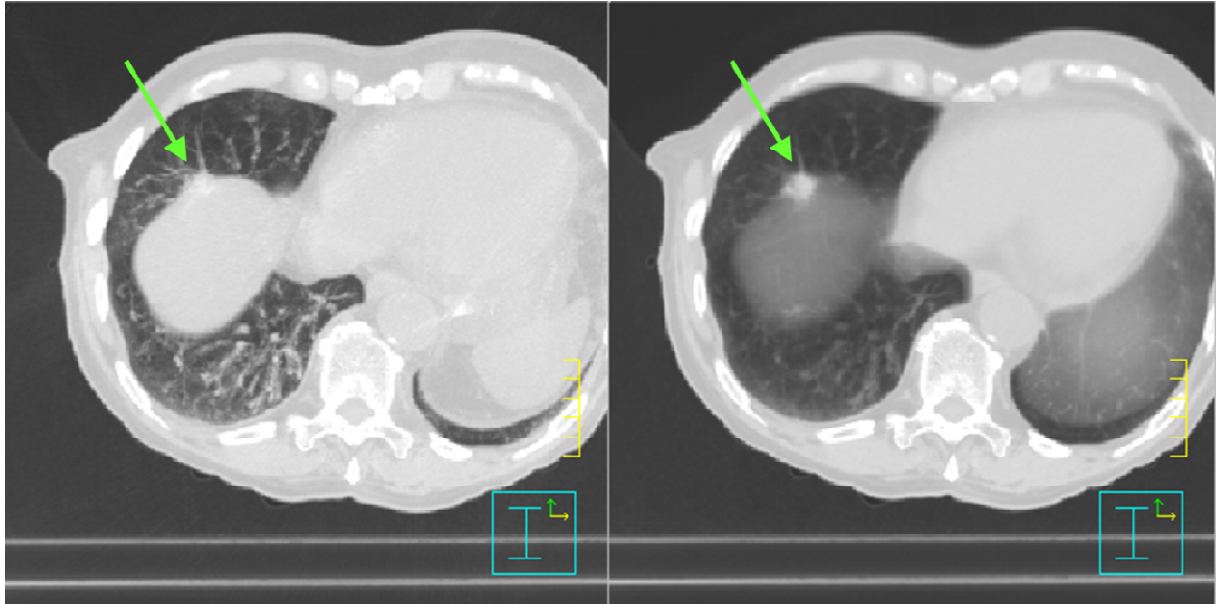


Figure 2.4: Transverse CT image of tumor adjacent to the liver. (left) Maximum intensity projection. (right) Respiratory-averaged CT. Reproduced with permission from Riegel *et al.* (Riegel *et al.*, 2009)

2.5 Discussion

Our results indicate that SBRT targets drawn with cine CT images sets are similar to or slightly larger than those drawn by full 10-phase 4D-CT image sets.

Bradley *et al.* found that contours based on MIP_{4D-CT} were significantly larger than those based on helical CT and $RACT_{4D-CT}$ and concluded that volumes drawn on MIP_{4D-CT} would presumably be less prone to geometric miss due to the fact they were larger and more inclusive (Bradley *et al.*, 2006). A recent dynamic MRI study by Cai *et al.*, however, demonstrated that MIP_{4D-CT} underestimated the true extent of tumor motion for lesions moving irregularly (Cai *et al.*, 2007). Furthermore, the underestimation was proportional to the variability of the respiratory pattern. The authors identified limited temporal resolution and “incomplete sampling strategy” as causes for the underestimation. A second study

using 4D-CT to scan a phantom under irregular motion (similar to the current study) found results consistent with our findings (Park et al., 2009). In the current study, we have shown that segmenting on MIP_{cine} produces larger IGTVs in phantoms and patients. Following the findings of Bradley and Cai, processing the MIP from cine CT improves the limited sampling of the MIP_{4D-CT} image set because it includes the complete set of cine images at each couch position, not just a 10-phase subset.

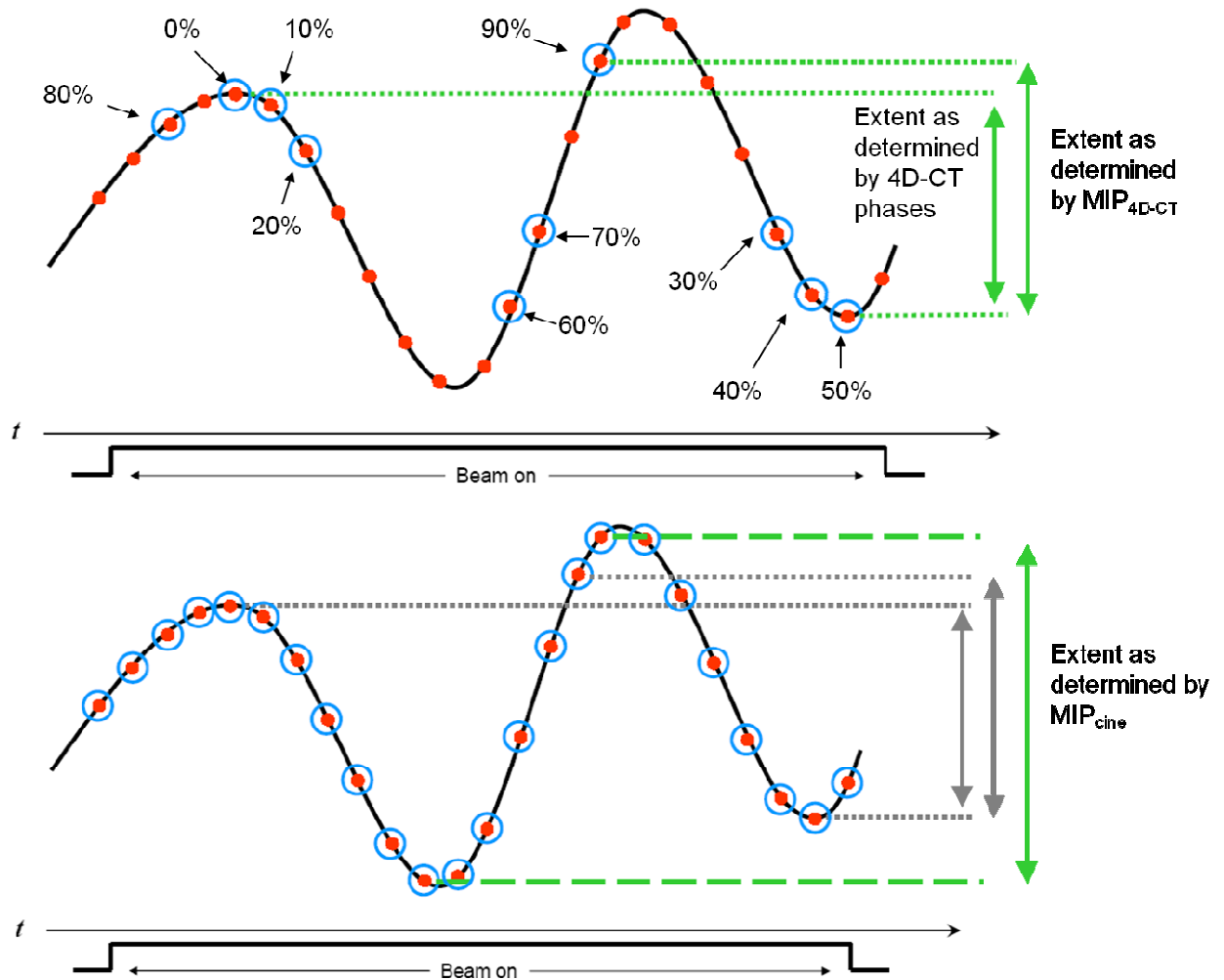


Figure 2.5: Observed motion extent in 4D-CT (top) versus observed motion extent in MIP_{cine} . Note that in 4D-CT, images that reflected the full motion extent were not included in the phase imaging. In MIP_{cine} , however, all images are included and maximum motion extent is imaged. Reproduced with permission from Riegel *et al.* (Riegel et al., 2009)

When more than one breathing cycle of a naturally varying respiratory waveform is imaged in 4D-CT acquisition, it is possible that the end inspiration (0%) and end expiration (50%) phases will not include the images that represent the largest motion extent of a tumor. Including more samples in the MIP process will increase the chances that the largest motion extent is imaged. This most likely explains the results of the phantom and patient auto-segmentation studies (where $IGTV_{\text{cine}}$ was significantly larger than $IGTV_{4\text{D-CT}}$) and this effect is demonstrated diagrammatically in Figure 2.5. As we previously found that 90% of patients have average breathing cycle periods of less than 6 s (Pan et al., 2006), we recommended that cine durations of 6 s be chosen for cine CT acquisition (Chi et al., 2007). One can increase the cine duration beyond one average breathing cycle, however, to provide better sampling of the varying respiratory waveform and produce a more encompassing MIP_{cine} image set.

One limitation of our method is that processing directly from cine CT will include rare respiratory irregularities such as coughing in the image sets. This is undesirable because such discontinuities represent relatively infrequent events that should not be included in treatment planning. Isolating these effects by manually removing cine CT images affected by such an event is possible (Pan et al., 2007).

In the manual segmentation study of patient images, cine-CT-based radiation treatment planning performed as well as 4D-CT. The results of our study show that including $RACT_{\text{cine}}$ in the delineation process with MIP_{cine} is sufficient in producing $IGTV$ s similar (within intraobserver variability) to those formed with full 4D-CT for lesions adjacent to tissue of equal or greater density. Several authors have cautioned against using MIP in these cases (Muirhead et al., 2008; Rietzel et al., 2005; Rietzel et al., 2008; Underberg et al., 2005), and one group has recommended that RACT not be used for contouring because the edges of the tumor are blurred by motion (Bradley et al., 2006). A group from the Netherlands, however, has advocated using RACT with a colormap to highlight degrees of motion (Cover et al., 2006). Figure 1.5 and Figure 2.4 demonstrate the benefit of using MIP and RACT together for moving tumors.

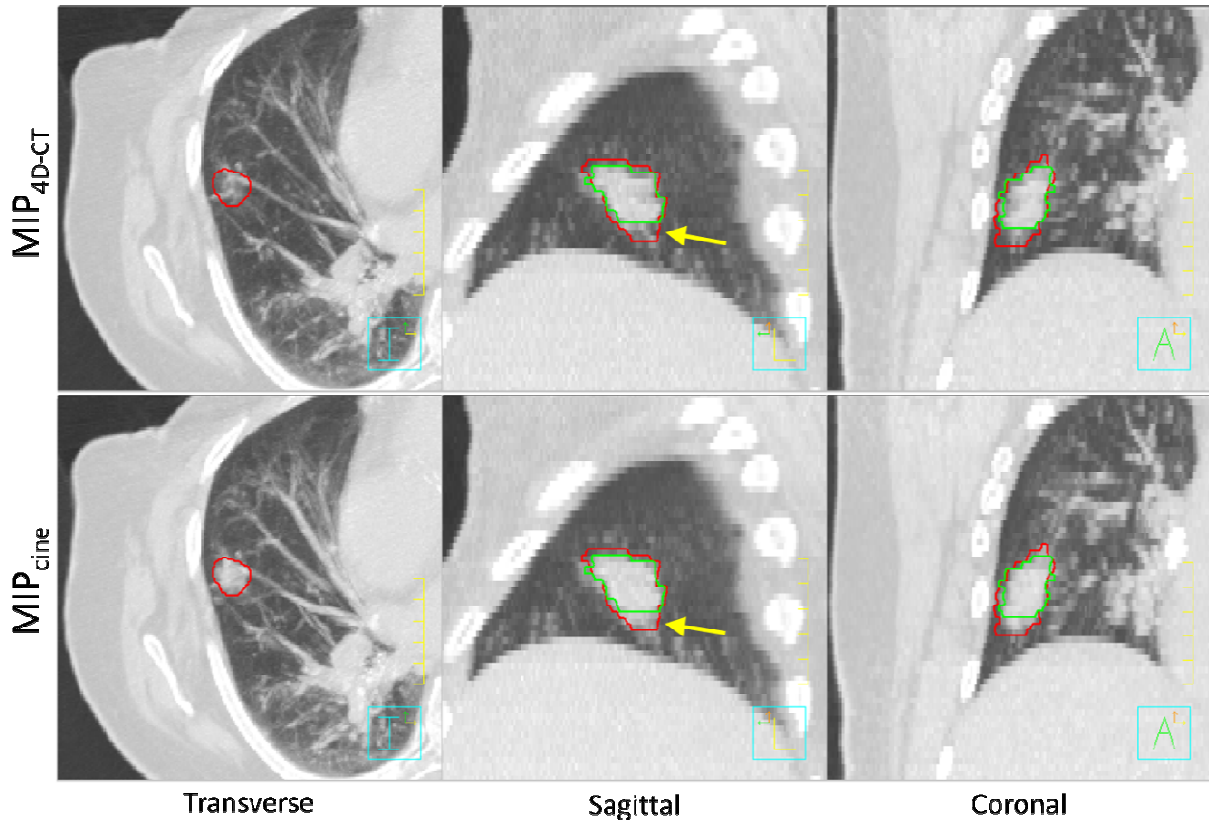


Figure 2.6: Maximum intensity projections processed from 4D-CT (top row) and cine CT (bottom row). Red contours are $IGTV_{cine}$ and green are $IGTV_{4D-CT}$. Note that cine CT captures several slices of tumor motion beyond that captured by 4D-CT. Reproduced with permission from Riegel *et al.* (Riegel *et al.*, 2009)

It is interesting that $IGTV_{4D-CT}$ and $IGTV_{cine}$ were not equivalent in the high-contrast group of tumors, where the lesions were *not* adjacent to dense structures. Mean $IGTV_{cine}$ was larger, though not significantly, than $IGTV_{4D-CT}$. This result can most likely be attributed to two factors: First, the average volume of high-contrast tumors was approximately two-thirds the average volume of low-contrast tumors, so an identical volume difference between $IGTV_{cine}$ and $IGTV_{4D-CT}$ in both groups would be a larger *percentage* difference in the first group than in the second, which would affect the volume ratio. Second, as described in the discussion above, MIP_{cine} uses the entire set of cine CT images for processing (between 20-30 images per slice location), which is a larger sample than MIP_{4D-CT} processing (10 images per slice location). The larger $IGTV_{cine}$ in the manually-contoured high-contrast tumors is consistent with the results of the patient and phantom auto-

segmentation studies. Figure 2.6 illustrates this effect for patient 1, whose $IGTV_{\text{cine}}/IGTV_{4\text{D-CT}}$ volume ratio was the second largest of all 27 patients. $MIP_{4\text{D-CT}}$ and MIP_{cine} images are shown that highlight the region of increased density at the inferior region of the tumor in the MIP_{cine} , which is not present in the $MIP_{4\text{D-CT}}$.

Though cine- and 4D-CT-defined tumor contours for treatment planning showed good agreement over the entire sample, individual cases still demonstrated the pitfalls of using MIP for contouring. Three patients with the lowest NDSC values (patients 18, 22, 26) all had lesions near the diaphragm where it was difficult to determine inferior extent because of overlap with the liver, even when contouring with RACT image data. These patients could potentially benefit from target definition with PET. In section 5.4.1, patient 26 is revisited using MIP_{cine} and PET together for contouring.

Cine acquisition mode is not unique to General Electric CT scanners and other groups have explored cine CT with scanners of different manufacture (Low et al., 2003; McClelland et al., 2006), but cine acquisition on other CT scanners is more complicated and less efficient than the GE implementation. Other manufacturers use a series of axial acquisitions at the same couch position rather than continuously acquiring data and reconstructing an image series retrospectively. Furthermore, the ability to scan a large area seems to be limited by protocol setup. For 4D-CT, Philips and Siemens both use a low-pitch helical acquisition mode which requires a respiratory trace to reconstruct images (Keall et al., 2004; Pan, 2005). In theory, low-pitch helical data could be subjected to “cine type” processing discussed in this chapter, but data that are not included in 4D-CT reconstruction cannot be accessed easily after reconstruction is completed due to the prospective nature of the scan. In the future, it may be possible to implement a similar reconstruction process to low-pitch helical data, but no such method has yet been developed.

Curiously, the GE 4D-CT sorting software enables the user to create MIP and RACT directly from cine CT instead of the 10 phases, but a respiratory trace is still required to initialize the program even though it is not used for the desired operation. Our software operates on a simple personal computer and bypasses the need for a respiratory trace.

2.6 Conclusions

As described in section 1.2, 4D-CT is complex and costly for many cancer centers. The motion information it provides, however, is extremely important in accurately targeting lung cancer and reducing treatment margins, thereby sparing additional normal tissue. This chapter has presented a cost-effective alternative to 4D-CT for treatment planning that does not require additional hardware or commercial software beyond that already available on scanners already in use. Creating MIP and RACT directly from the cine CT images and using these images sets together to define targets for SBRT produces volumes that are similar to those drawn by full 10-phase 4D-CT.

The results of this chapter pertain mainly to small, mobile lesions. We anticipated that, for larger tumors and later-stage lung cancer (such as stage III, for which IMRT in conjunction with chemotherapy is a curative treatment modality for inoperable disease (Furuse et al., 1999; Govindan, 2003)), the use of cine CT in treatment planning will be limited because of more complicated involvement with surrounding tissue (Muirhead et al., 2008). In chapters 4 and 5, attempts to incorporate positron emission tomography (PET) into the cine CT treatment planning process are described. PET/CT may provide additional contrast for target definition in cases with complicated tumor involvement with surrounding tissue. Several studies have analyzed the impact of including PET data in GTV delineation for NSCLC and have yielded noteworthy results, mostly due to the inclusion of lymph nodes and exclusion of atelectasis (Bradley et al., 2004; Nestle et al., 1999; van Baardwijk et al., 2006). Those studies suggest that metabolic information from PET helps physicians discriminate between normal and malignant tissue that is indistinguishable on CT alone, which can sometimes occur when using MIP.

Another subject not covered in this chapter yet still an important aspect of treatment planning is dose calculation. This topic is covered in chapter 3.

Chapter 3 DOSE CALCULATION WITH CINE RESPIRATORY-AVERAGED CT

3.1 Introduction

In the previous chapter, the important aspect of tumor delineation on MIP_{cine} and $RACT_{cine}$ was discussed. In this chapter, dose calculation with $RACT_{cine}$ is explored. After the tumor is delineated, the appropriate margins are added, and beam arrangements have been planned, the resulting dose distribution is calculated. Convolution-superposition, a typical calculation algorithm, operates by integrating the product of the primary photon fluence from each beam, a convolution kernel or “dose spread array” that can be obtained by measurement or Monte Carlo simulation, and the mass attenuation coefficient provided by the CT image set (Khan, 2003). Note that linear attenuation coefficients obtained at diagnostic energies must be scaled for use in the therapeutic (megavoltage) range. Typically, dose is calculated on a free-breathing helical CT data set. However, artifacts during image acquisition due to respiratory motion are well-known (Chen et al., 2004; Gagne et al., 2004).

Dose calculation based on 4D-CT data sets has been explored (Flampouri et al., 2006; Guckenberger et al., 2007; Keall et al., 2004; Rietzel et al., 2005). These calculation methods generally apply a 3-D treatment plan to each phase of the 4D-CT data set, equally divide the number of monitor units among each of the phases, and register the resulting dose distributions to a reference phase using rigid or deformable registration. Though not truly 4-D treatment planning, this calculation methodology should provide a more accurate estimate of how dose is distributed over a respiratory cycle than calculation on a single, presumably stationary image set. Currently, however, this methodology is not commonly used clinically.

Guckenberger *et al.* compared dose calculation on 3-D and 4-D image sets by recalculating dose on different phases of the 4D-CT and comparing these distributions to 4-D dose calculation described above. This study demonstrated minimal dosimetric differences for GTV and ITV in the two methods (Guckenberger et al., 2007), suggesting that

full 4-D dose calculation using all phases of imaging may not be necessary to estimate dose to a moving target. Producing 3-D image sets that reflect respiratory motion, however, still requires 4D-CT; end-inspiration and end-expiration scans are generally not reliable (Pan et al., 2005). Admiraal *et al.* demonstrated that dose calculation on $\text{RACT}_{4\text{D-CT}}$, the pixel-by-pixel average of the 10 phases of 4D-CT, produces similar results to the dose calculation methodology described above (Admiraal et al., 2008). The use of $\text{RACT}_{4\text{D-CT}}$ for dose calculation has been adopted at M. D. Anderson because $\text{RACT}_{4\text{D-CT}}$ represents moving structures more accurately than free-breathing helical CT or end-inspiration/expiration imaging over a fraction of radiation.

As the last chapter explored the use of MIP_{cine} and $\text{RACT}_{\text{cine}}$ for target delineation, a logical question is whether or not $\text{RACT}_{\text{cine}}$ could replace $\text{RACT}_{4\text{D-CT}}$ for dose calculation. $\text{RACT}_{\text{cine}}$, however, averages *all* the images at each couch position, which can over- or under-emphasize different parts of the respiratory cycle in the CT number averaging process (Chi et al., 2007). This can be demonstrated with a simple example. From calculus, the mean of any function is:

$$\overline{f(x)} = \frac{\int_a^b f(x') dx'}{b-a} \quad (3)$$

If we consider the respiratory trace as a simple sine function, the mean of the sine function is:

$$\overline{f(x)} = \frac{1-\cos(x)}{x} \quad (4)$$

Figure 3.1 illustrates the sine function and the mean of the sine function. When $x = 2\pi k$ (where k are integers), $\cos(x) = 1$ and $\overline{f(x)} = 0$. This is comparable to $\text{RACT}_{4\text{D-CT}}$: Ten image sets are chosen to represent equally-spaced phases of one respiratory cycle, like 1 period of a sine wave ($k = 1$). When $x \geq 2\pi$, $\overline{f(x)}$ reaches a maximum at $x \approx 3\pi$ or 1.5 breathing cycles. $\text{RACT}_{\text{cine}}$, therefore, will be most different from $\text{RACT}_{4\text{D-CT}}$ when

approximately 1.5 breathing cycles are captured in 1 cine duration (CD). $RACT_{cine}$ will be “weighted” towards one-half of the respiratory pattern more than the other, which may have a significant impact on dose calculation (Chu et al., 2000; Geise et al., 1977). Another feature of Figure 3.1 is the presence of an “envelope” function ($1/x$) which causes the overall function to decrease with increasing x . Consequently, increasing the number of images acquired at each couch position (e.g. increasing the CD) should make $RACT_{cine}$ more similar to $RACT_{4D-CT}$.

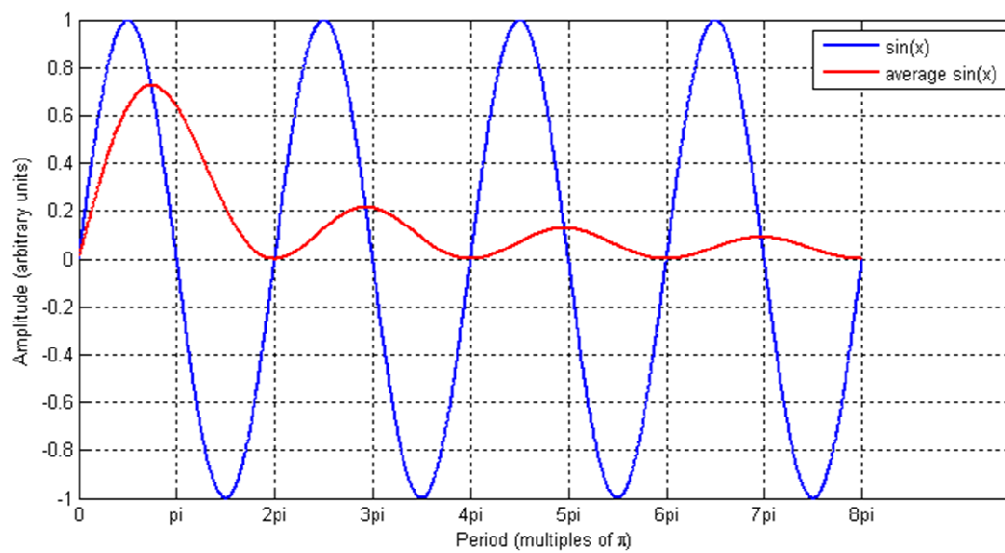


Figure 3.1: $\sin(x)$ and the average of $\sin(x)$. Reproduced with permission from Riegel et al. (Riegel et al., 2008)

3.2 Purpose

The purpose of this chapter was to evaluate the difference in dose calculation on $RACT_{4D-CT}$ and $RACT_{cine}$. We hypothesized that differences between the dose distributions would be negligible and that differences would decrease as CD increases (because more imaging samples of the respiratory cycle are included in the averaging process). Successfully demonstrating that $RACT_{cine}$ can replace $RACT_{4D-CT}$ for dose calculation could provide an image set which emulates 4-D dose calculation to treatment centers without

access to 4D-CT. This, in conjunction with the results of Chapter 2 , lends further support to our over-arching hypothesis that image sets processed from cine CT can replace 4D-CT image sets for treatment planning purposes with negligible differences.

3.3 Methods

3.3.1 Patient Study

Twenty-three lung cancer patients who received 4D-CT simulation as part of their radiation therapy were retrospectively included in the “primary” patient group. These patients had an average of at least 2 breathing cycles per CD. The respiratory patterns were classified as “regular” or “irregular” by calculating the coefficient of variation (COV) of the respiratory period over the duration of the scan. The COV was defined as the standard deviation over the mean expressed as a percentage. COVs <10% were considered regular and those >10% were considered irregular. We anticipated the over/under-emphasis phenomenon will affect patients with regular breathing cycles more because the same *fraction* of the breathing cycle will be averaged for every couch position, though the *phase* will be different (Figure 3.2). Table 3.1 summarizes the patient respiratory characteristics.

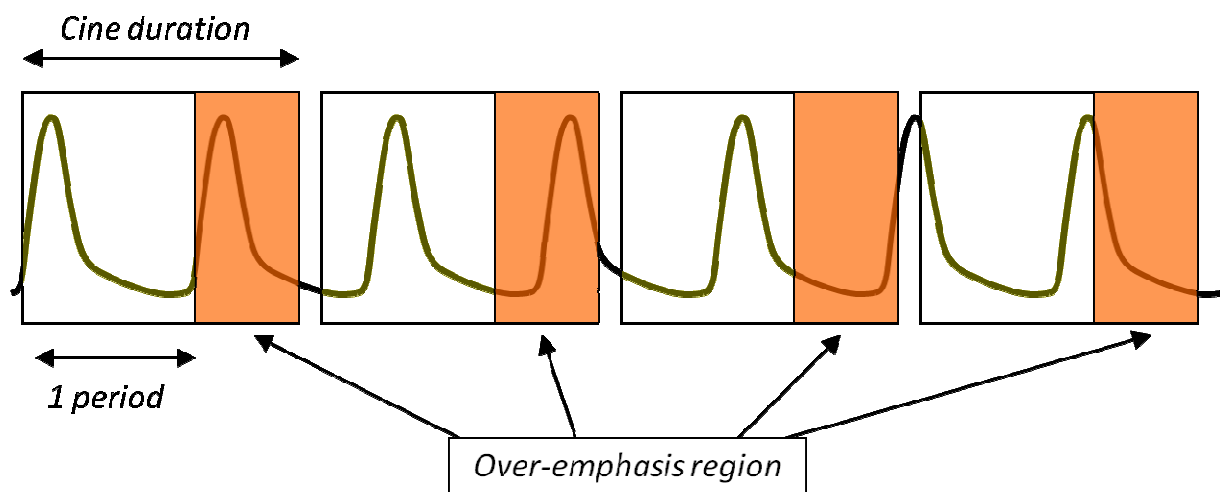


Figure 3.2: Overemphasis of sections of the respiratory pattern. The yellow-shaded region represents one period of the respiratory cycle and the orange-shaded region is the part of the breathing cycle averaged twice in $RACT_{cine}$, thereby “weighting” the image towards the repeated phase of the breathing cycle. Reproduced with permission from Riegel *et al.*

Table 3.1: Primary group patient characteristics.

Patient #	Location	Avg. T (s)	CD/Avg. T	COV (%)	Tx
1	Lung	2.2	2.0	4.3	IMRT
2	Lung	2.7	2.2	4.4	IMRT
3	Lung	2.3	2.2	4.8	IMRT
4	Liver	2.5	2.2	6.4	3DCRT
5	Esophageal	1.8	2.5	6.7	IMRT
6	Lung	2.1	2.4	6.8	IMRT
7	Lung	2.7	2.2	7.8	SBRT
8	Lung	1.9	2.1	7.9	SBRT
9	Lung	1.6	2.5	8.0	IMRT
10	Lung	2.1	2.1	8.9	SBRT
11	Liver	3.0	2.3	9.7	IMRT
12	Lung	2.6	2.2	11.2	IMRT
13	Lung	2.3	2.2	12.9	SBRT
14	Lung	2.2	2.3	13.0	IMRT
15	Lung	3.5	2.1	16.1	IMRT
16	Lung	3.2	2.2	18.9	3DCRT
17	Lung	2.7	2.2	20.5	IMRT
18	Esophageal	1.9	2.3	20.5	IMRT
19	Lung	3.1	2.3	22.6	IMRT
20	Esophageal	2.6	2.3	26.2	3DCRT
21	Lung	2.2	2.3	34.0	IMRT
22	Lung	2.3	2.3	37.0	IMRT
23	Lung	2.6	2.5	37.2	IMRT
Average		2.4	2.3		
Standard Dev.		0.5	0.1		

Avg. T = average breathing cycle

CD = cine duration

COV = coefficient of variation

Tx = treatment technique

IMRT = intensity modulated radiation therapy

SBRT = stereotactic body radiation therapy

3DCRT = 3-D conformal radiation therapy.

All 4D-CT simulations were performed on an 8-slice General Electric Discovery ST PET/CT scanner (GEMS, Waukesha, WI) in cine mode with 2.5 mm slice thickness, 50 cm field-of-view, and 512 by 512 image matrix producing a pixel size of $0.97 \times 0.97 \times 2.5 \text{ mm}^3$. $\text{RACT}_{\text{cine}}$ was processed from the same cine CT from which the simulation 4D-CT was formed, thereby eliminating the need to expose the patient to further irradiation. A different number of images were included in each $\text{RACT}_{\text{cine}}$ to simulate fractions of the breathing cycle being captured at each couch position (1 breathing cycle, 1.5 breathing cycles, and 2 breathing cycles). These image sets are designated $\text{RACT}_{\text{cine1}}$, $\text{RACT}_{\text{cine1.5}}$, and $\text{RACT}_{\text{cine2}}$ in this chapter.

The clinical treatment plan was copied to each $\text{RACT}_{\text{cine}}$ image set and dose was recalculated using CCC on a 4 mm isotropic grid with Pinnacle³ version 7.6. Sagittal, coronal, and transverse dose planes through the isocenter were interpolated to 1 mm pixels and exported for $\text{RACT}_{4\text{D-CT}}$, $\text{RACT}_{\text{cine1}}$, $\text{RACT}_{\text{cine1.5}}$, and $\text{RACT}_{\text{cine2}}$ treatment plans.

Because the clinical protocol for 4D-CT is to set the CD to 1 breathing cycle plus 1 gantry rotation (Pan et al., 2004), the number of patients in the study is small. Furthermore, the average breathing period of these patients was relatively short. We therefore performed a follow-up study with a larger number of patients and longer breathing periods more typical of clinical exams. Fifty (50) lung cancer patients whose clinical dose calculation was performed on $\text{RACT}_{4\text{D-CT}}$ were included for comparison. This group was designated the “follow-up” patient group. Table 3.2 summarizes patient characteristics for the follow-up patient group. Of these 50 patients, 25 received SBRT and 25 received IMRT. As before, $\text{RACT}_{\text{cine}}$ was reconstructed using the same cine CT data as the 4D-CT simulation. Averaging, however, was only performed with the maximum number of images at each couch position (as would be performed clinically in our cine CT-based planning paradigm). As before, the clinical plan was copied to the $\text{RACT}_{\text{cine}}$ image set, dose was recalculated, and dose distributions on $\text{RACT}_{4\text{D-CT}}$ and $\text{RACT}_{\text{cine}}$ were compared.

Table 3.2: Follow-up group patient characteristics.

IMRT			SBRT		
Patient #	Avg. T (s)	CD/Avg. T	Patient #	Avg. T (s)	CD/Avg. T
1	7.0	1.3	26	3.4	1.6
2	6.2	1.2	27	4.6	1.7
3	6.2	1.1	28	3.1	1.6
4	6.2	1.2	29	4.9	1.3
5	6.2	1.2	30	5.2	1.2
6	6.2	1.2	31	---	---
7	6.1	1.2	32	4.2	1.4
8	5.8	1.3	33	5.6	1.3
9	5.5	1.3	34	5.7	1.6
10	5.3	1.3	35	4.5	1.6
11	5.2	1.1	36	2.6	1.9
12	5.2	1.3	37	6.0	1.6
13	5.1	1.4	38	4.6	1.9
14	5.1	1.5	39	7.9	1.5
15	5.0	1.4	40	7.6	1.2
16	4.8	1.3	41	5.9	1.0
17	4.7	1.3	42	5.2	1.3
18	4.7	1.3	43	4.9	1.1
19	4.6	1.3	44	4.8	1.3
20	4.5	1.1	45	4.7	1.2
21	4.4	1.4	46	4.7	1.3
22	4.4	1.6	47	4.7	1.7
23	4.4	1.4	48	4.6	1.4
24	4.4	1.4	49	4.4	1.3
25	4.3	1.4	50	4.1	1.4
Average	5.3	1.3	Average	4.9	1.4
SD	0.8	0.1	SD	1.2	0.2

Respiratory trace could not be retrieved for patient 31.
 For abbreviations, see Table 3.1.

3.3.2 Analysis

RACT_{cine} plans were compared to the RACT_{4D-CT} plan using the gamma (γ) index (Depuydt et al., 2002; Low et al., 1998; Low et al., 2003) inside the planning target volume (PTV). The γ index is defined in equations (5) and (6). The variables r_e and r_r represent points on the evaluated and reference distributions respectively, where d and D are the distance-to-agreement and dose difference pass/fail criteria selected by the user.

$$\Gamma(\vec{r}_e, \vec{r}_r) = \sqrt{\frac{r^2(\vec{r}_e, \vec{r}_r)}{\Delta d^2} + \frac{\delta^2(\vec{r}_e, \vec{r}_r)}{\Delta D^2}} \quad (5)$$

$$\gamma(\vec{r}_r) = \min\{\Gamma(\vec{r}_e, \vec{r}_r)\} \forall \{\vec{r}_e\} \quad (6)$$

Pass/fail criteria for the γ index are typically 5%/3 mm or 3%/3 mm in clinical situations such as IMRT quality assurance (Depuydt et al., 2002; Low et al., 1998; Low et al., 2003). In these cases, dose distributions are calculated in a phantom and are compared to film measurements. Since we compared two calculated distributions, the pass/fail criteria were tightened to 2%/1mm to reflect a lower percent dose difference limit of dose calculation accuracy (Papanikolaou et al., 2004) and the spatial resolution of the CT scanner in the transverse plane with a 512×512 image matrix and 50 cm FOV.

DOSELAB software, a publicly-available dose-comparison software package, was used to calculate γ indices in each of the 3 orthogonal planes (Childress et al., 2003; Childress et al., 2005). Dose planes contained the full extent of the dose grid. The intersection of the clinical PTV and the orthogonal dose planes were the areas of interest (Figure 3.3). Maximum and mean γ indices and percentages of points passing the γ criteria were measured for these areas. The PTV was formed clinically according to the procedure described in a recent publication from authors at M. D. Anderson (Ezhil et al., 2009). First, the IGTV was formed by contouring the “motion envelope” on MIP_{4D-CT} and confirming extent on the 4D-CT phase images. The IGTV was expanded to the internal clinical target

volume (ICTV) using an 8 mm isotropic expansion. The ICTV was expanded to the PTV with a 5 mm or 3 mm expansion depending on the type and frequency of image guidance utilized in treatment. For PTVs with multiple regions, a weighted average of the γ index in each region was calculated.

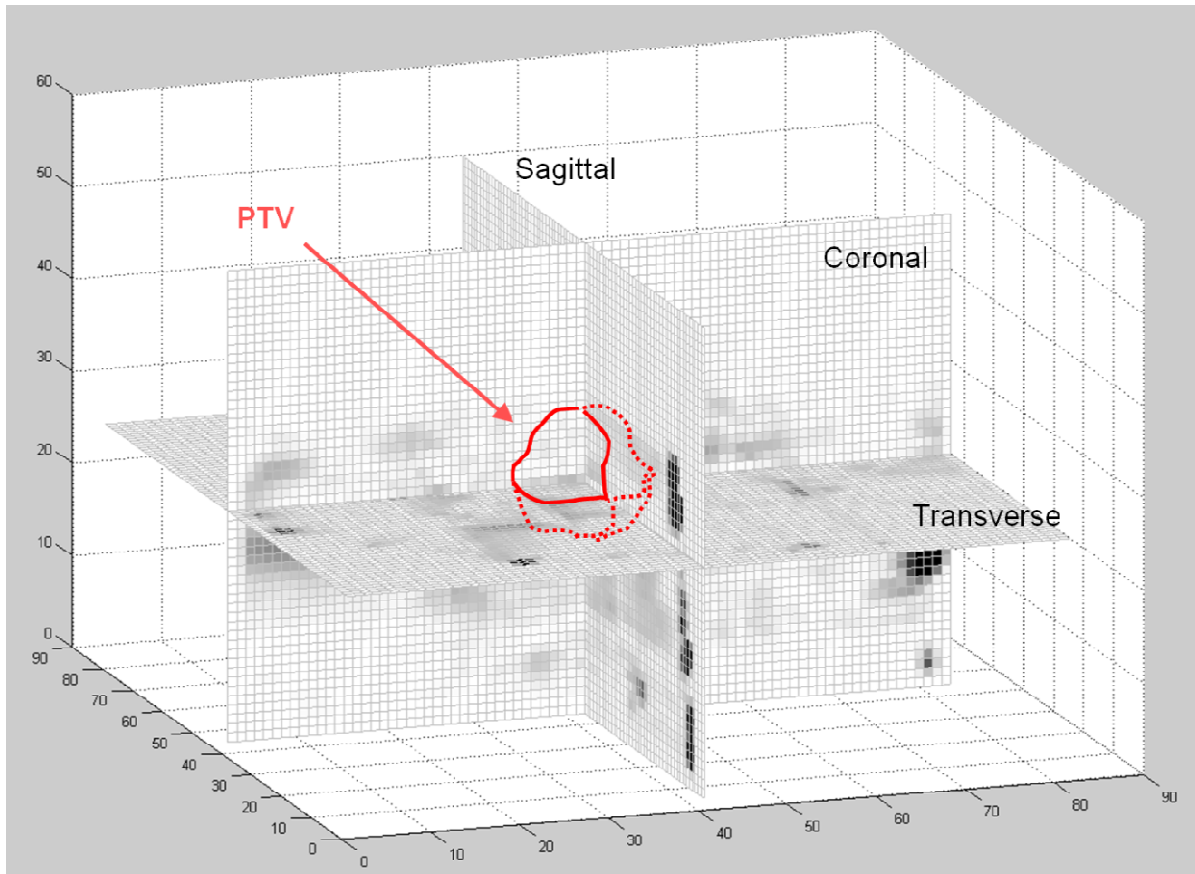


Figure 3.3: Intersection of planning target volume (PTV) and orthogonal dose planes. Reproduced with permission from Riegel *et al.* (Riegel *et al.*, 2008)

For the primary group of patients, γ indices for $RACT_{\text{cine1}}$ vs. $RACT_{4\text{D-CT}}$, $RACT_{\text{cine1.5}}$ vs. $RACT_{4\text{D-CT}}$, and $RACT_{\text{cine2}}$ vs. $RACT_{4\text{D-CT}}$ were calculated and compared using a one-way analysis of variance (ANOVA) for correlated samples with a post-ANOVA Tukey HSD test to detect any statistically significant differences between the dose calculations on image sets of increasing CD (Lowry, 2008). We anticipated that maximum and mean γ indices would decrease with increasing CD. For the follow-up group of patients, γ indices were calculated

for the $\text{RACT}_{\text{cine}}$ vs. $\text{RACT}_{4\text{D-CT}}$ comparison. Note that statistical analysis was not performed because only one comparison was performed for the follow-up group.

3.4 Results

3.4.1 Primary Patient Group

For the $\text{RACT}_{\text{cine1}}$ vs. $\text{RACT}_{4\text{D-CT}}$ and $\text{RACT}_{\text{cine1.5}}$ vs. $\text{RACT}_{4\text{D-CT}}$ comparisons, 22 of 23 patients demonstrated 100% of points within the PTV on coronal, sagittal, and transverse planes passing our 2%/1mm γ criteria. The lone patient who demonstrated any failing points had 1.4% and 0.3% of points fail on coronal and sagittal planes respectively for the $\text{RACT}_{\text{cine1}}$ vs. $\text{RACT}_{4\text{D-CT}}$ comparison. Though already extremely low, the failures decreased to 0.6% and 0% on coronal and sagittal planes respectively in the $\text{RACT}_{\text{cine1.5}}$ vs. $\text{RACT}_{4\text{D-CT}}$ comparison, then disappeared completely in the $\text{RACT}_{\text{cine2}}$ comparison. All patients demonstrated 100% passing points within the PTV for all geometrical orientations in the $\text{RACT}_{\text{cine2}}$ vs. $\text{RACT}_{4\text{D-CT}}$ comparison.

Maximum and mean γ indices for the $\text{RACT}_{\text{cine1}}$, $\text{RACT}_{\text{cine1.5}}$, and $\text{RACT}_{\text{cine2}}$ comparisons within the PTV for regular respiratory patterns are shown in Figure 3.4 and results for irregular respiratory patterns are shown in Figure 3.5. Maximum and mean values are very low, well under 1, which demonstrates that dose calculation on $\text{RACT}_{\text{cine}}$ is very similar to dose calculation on $\text{RACT}_{4\text{D-CT}}$, regardless of how many breathing cycles are used for averaging. The data shows, however, that increasing the CD does, in general, decrease the γ index to even lower levels. The maximum and mean γ indices from the $\text{RACT}_{\text{cine2}}$ vs. $\text{RACT}_{4\text{D-CT}}$ comparison are significantly lower than the $\text{RACT}_{\text{cine1}}$ vs. $\text{RACT}_{4\text{D-CT}}$ and $\text{RACT}_{\text{cine1.5}}$ vs. $\text{RACT}_{4\text{D-CT}}$ indices for several comparisons (coronal and transverse plane) with irregular respiration (arrows in Figure 3.5). The $\text{RACT}_{\text{cine1.5}}$ vs. $\text{RACT}_{4\text{D-CT}}$ γ indices were not significantly higher for regular respiration, contrary to what we had anticipated.

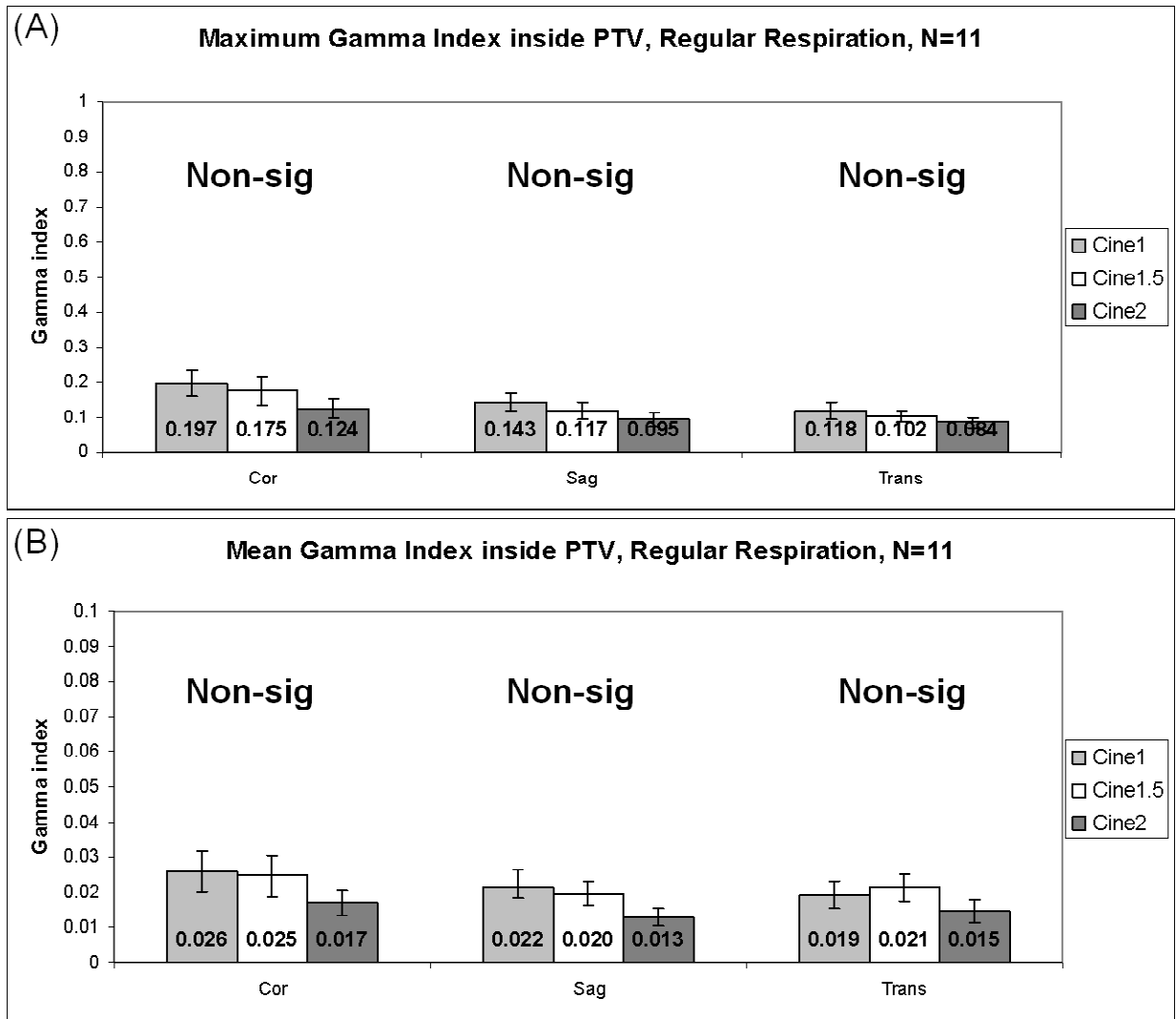


Figure 3.4: (A) Maximum and (B) mean gamma (γ) indices for patients with regular respiratory patterns. Error bars are standard error (N=11). Reproduced with permission from Riegel *et al.* (Riegel *et al.*, 2008)

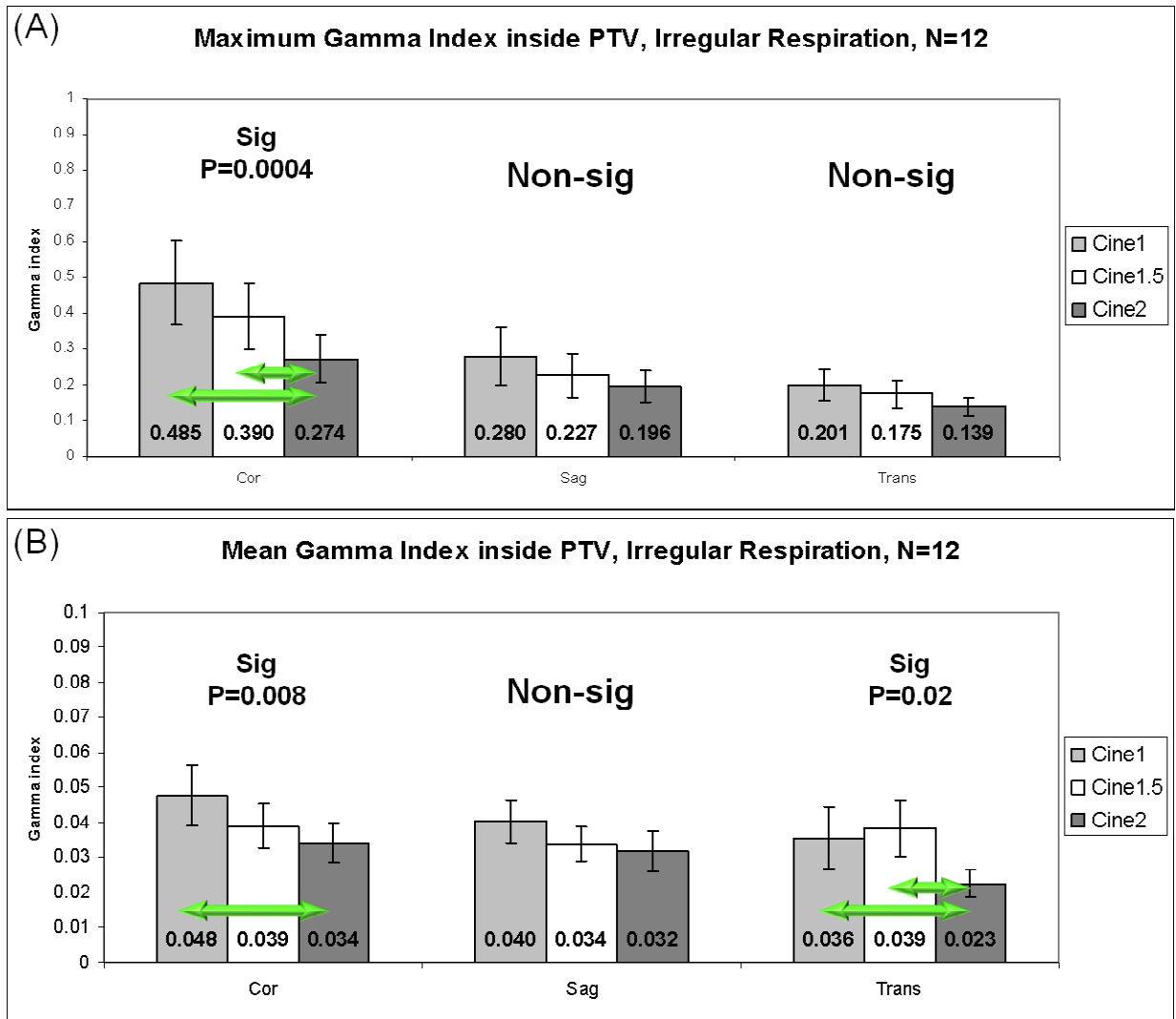


Figure 3.5: (A) Maximum and (B) mean gamma (γ) indices for patients with irregular respiratory patterns. Error bars are standard error (N=12). Green arrows are significant differences as determined by ANOVA/Tukey HSD tests. Reproduced with permission from Riegel *et al.* (Riegel *et al.*, 2008)

3.4.2 Follow-up Patient Group

Gamma criteria were met for 100% of points within the PTV for 49 of 50 patients. Patient 22 had 1% of points within the PTV fail the 2%/1mm criteria on the coronal γ distribution.

Figure 3.6 shows the maximum and mean γ indices within the PTV for the 3 orthogonal dose planes. All are well below 1, again supporting that calculation on $RACT_{cine}$ is very similar to calculation on $RACT_{4D-CT}$. Figure 3.7 compares maximum and mean γ indices within the PTV for SBRT and IMRT treatment techniques. The maximum γ index is higher in IMRT treatment techniques, but the mean γ index is higher in SBRT treatment techniques. This discrepancy is most likely caused by the small PTVs utilized in SBRT: Dose was calculated using a 4 mm isotropic grid interpolated to 1 mm on each dose plane for γ analysis. A $4 \times 4 \times 4 \text{ mm}^3$ cube occupies a larger percentage of the total volume for a small volume than a large volume, thereby weighting the mean towards the higher γ value.

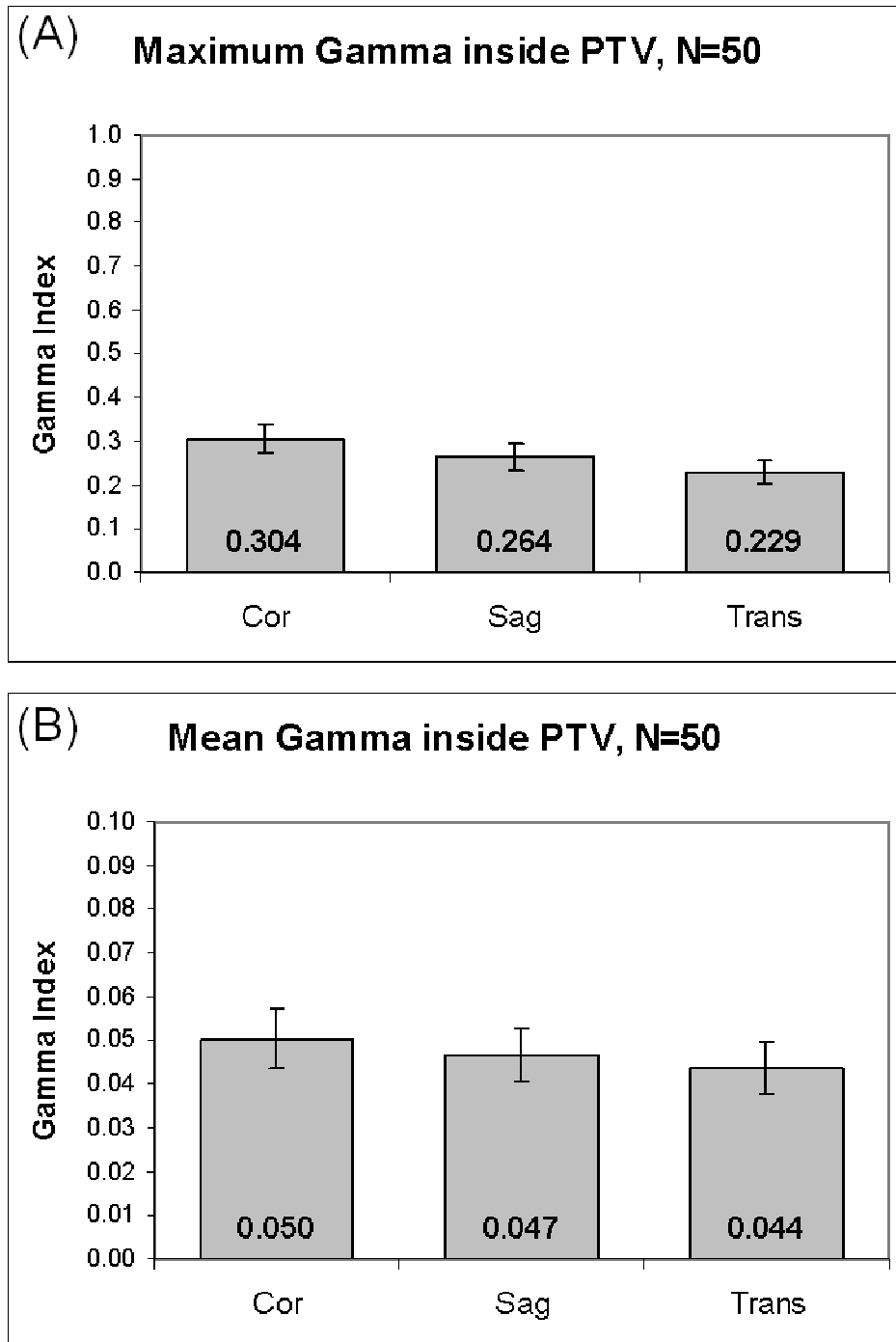


Figure 3.6: (A) Maximum and (B) mean gamma indices inside the PTV for the follow-up patient group. Error bars are standard error. Reproduced with permission from Riegel *et al.* (Riegel *et al.*, 2008)

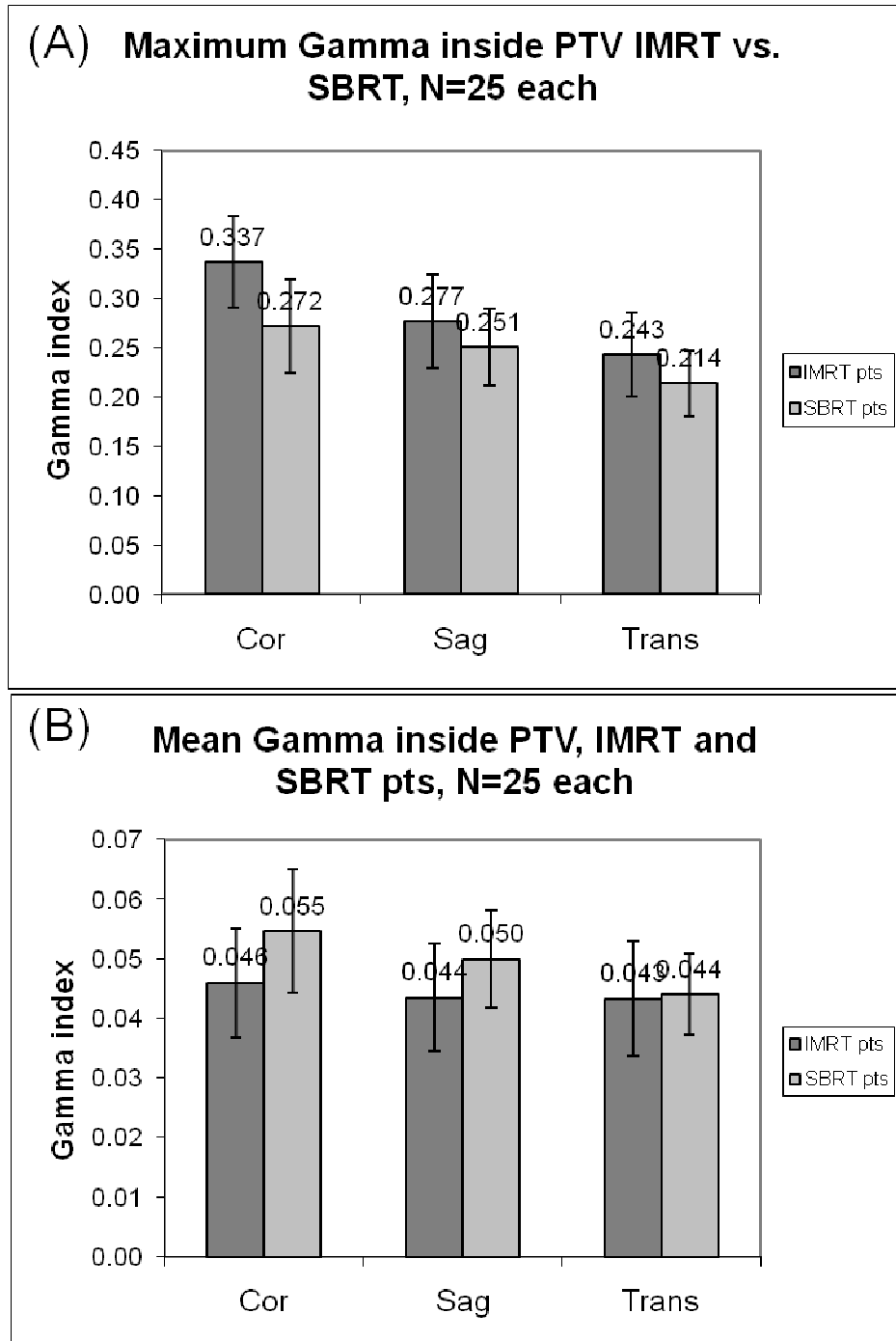


Figure 3.7: (A) Maximum and (B) mean gamma indices inside the PTV for the follow-up patient group, separated by treatment technique. IMRT = intensity modulated radiation therapy. SBRT = stereotactic body radiation therapy. Reproduced with permission from Riegel *et al.* (Riegel *et al.*, 2008)

3.5 Discussion

Several authors have explored 4-D dose calculation (Flampouri et al., 2006; Guckenberger et al., 2007; Keall et al., 2004; Rietzel et al., 2005), but the technique is not commonly used clinically due to the need for 4D-CT (which, as described above, is not readily available for many institutions) and increased calculation time. At M. D. Anderson, dose calculation with RACT_{4D-CT} is currently utilized for treatment planning of thoracic lesions. Admiraal *et al.* have shown that this technique can produce similar results to 4-D dose calculation (Admiraal et al., 2008). We developed a technique to create RACT image sets directly from the cine CT images which does not require a respiratory trace or sorting into phase or amplitude bins. RACT_{cine}, however, is not identical to RACT_{4D-CT}: Including all the cine CT images in RACT processing may cause CT number differences from the RACT_{4D-CT}. An early paper by Geise *et al.* cites that a 4-10% change in electron density may produce a 2% error in dose (Geise et al., 1977). In the case of regions highly affected by motion, especially irregular motion, CT number fluctuation may exceed this limit.

The current chapter has shown that calculating dose on RACT_{cine} image sets is negligibly different than calculating dose on RACT_{4D-CT}. Discrepancies can be decreased further by including more than one period of a respiratory pattern in each CD of cine CT (Figure 3.4 and Figure 3.5). Patient 22 in the primary group was the only patient to demonstrate any points failing the 2%/1mm γ criteria in the RACT_{cine1} and RACT_{cine1.5} comparisons, but these failing points disappeared as the CD increased to 2 breathing cycles. Our findings suggest that RACT_{cine} could replace RACT_{4D-CT} for the purposes of dose calculation with negligible differences in resulting dose distributions.

As briefly described in section 3.3.1, the first set of patients suffers from several problems: First, the sample size is small because the typical criteria for CD selection is 1 average breathing cycle plus 1 gantry rotation (Pan et al., 2004), therefore making patients with 2 breathing cycles per CD rare. Second, as a consequence of the first point, some patients with esophageal or liver malignancies were added to the core of lung cancer patients to increase sample size. Third, patients with multiple respiratory cycles per CD are often breathing rapidly and the average respiratory periods of these scans are typically

smaller than those of the general population receiving 4D-CT. The average breathing period of patients used in the first part of the study was less than 3 s, while most patients have a breathing period between 4 and 5 s (Pan et al., 2006).

To address these concerns, we included a second “follow-up” set of 50 lung cancer patients whose respiratory periods were closer to the population average. Multiple RACT_{cine} image sets, however, could not be reconstructed because less than 2 breathing cycles were captured at each couch position. The fact that γ analysis of the follow-up patient group is similar to results of the first supports the conclusion that RACT_{cine} is sufficiently similar to RACT_{4D-CT} for dose calculation.

Patient 40 demonstrated a substantial change in density distribution from motion blurring on RACT_{4D-CT} and RACT_{cine}. Patient 40 was also the only patient to show failing points in the follow-up group of patients. The differing density values caused the observed disagreement in dose distributions, particularly at the superior and inferior regions of the tumor, which was located near the diaphragm (Figure 3.8). Regardless, the regions of disagreement were small and the points failing within the PTV represented only 1% of the PTV volume. Other patients demonstrated similar differences near high contrast boundaries, though not beyond our 2%/1mm failure criteria.

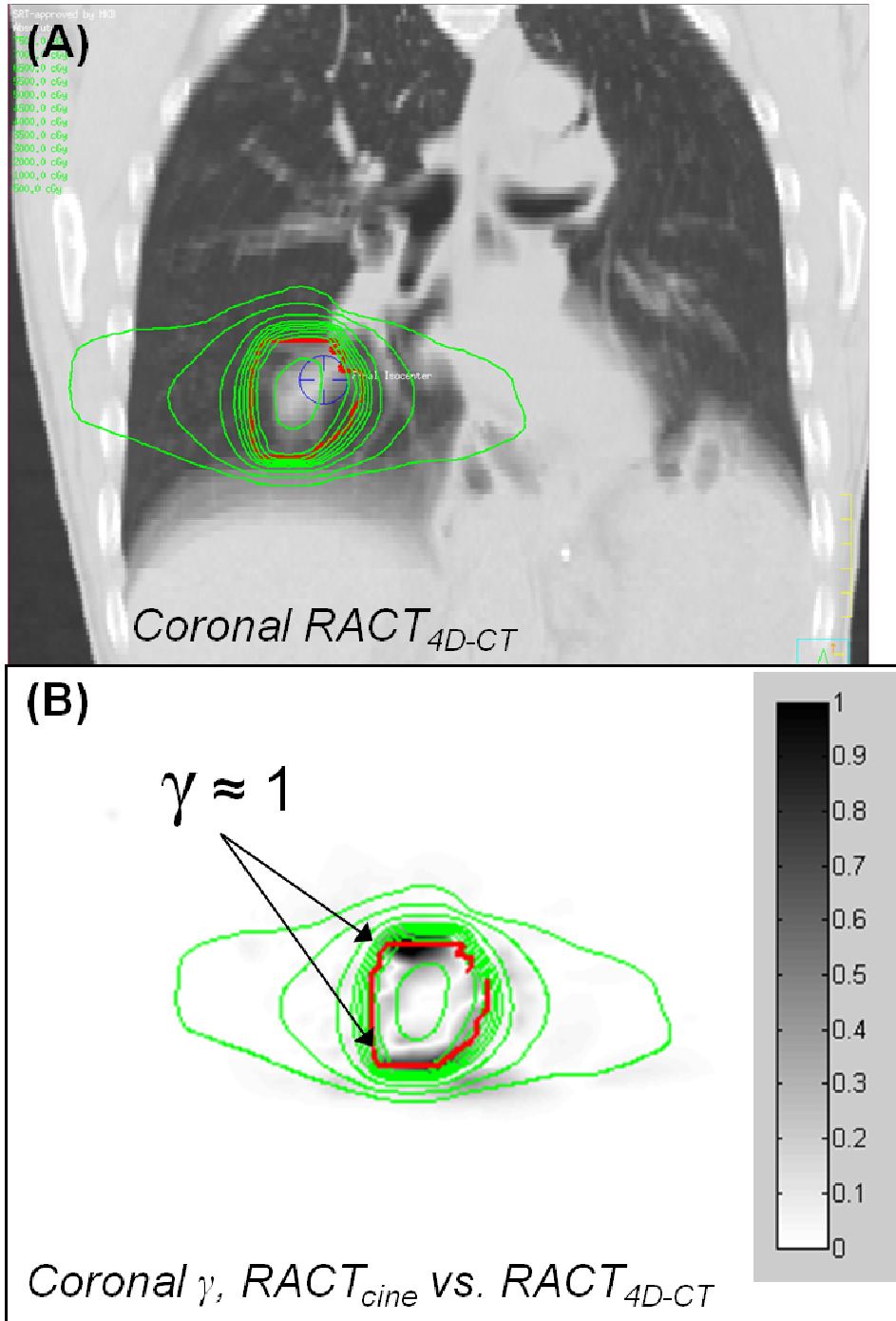


Figure 3.8: (A) Coronal $RACT_{4D-CT}$ and (B) Coronal γ distribution for patient 40 of the follow-up group. Note that our 2%/1mm γ criteria are violated at the maximum extents of tumor motion. Reproduced with permission from Riegel *et al.* (Riegel *et al.*, 2008)

Even when changes in motion blur occur outside the target volumes themselves, high-motion areas can still affect dose agreement within the PTV. Moving structures in the beam path can modulate the depth dose curves, which can cause “shadows” of dose disagreement behind moving structures. As an example, Figure 3.9 uses the end-inspiration and end-expiration phases of a 4D-CT to demonstrate this effect with dose calculated for one oblique beam. Figure 3.10 shows images and γ distributions from patient 20 of the primary group where this effect can be observed. Because coplanar beams enter the patient parallel to the transverse plane, this may explain why “shadowing” effects transverse slices more than coronal or sagittal slices. This is supported by Figure 3.4 and Figure 3.5, where the $RACT_{\text{cine1.5}}$ mean γ index is greater, though not significantly, than the $RACT_{\text{cine1}}$ mean γ index inside the PTV for regular and irregular respiration on transverse slices only, not coronal or sagittal.

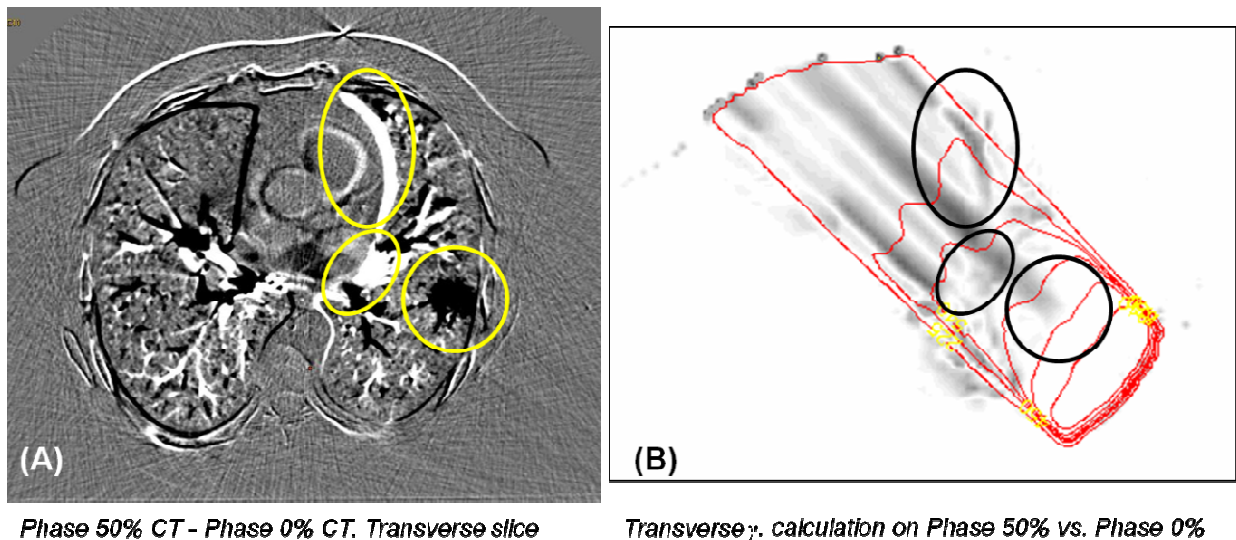


Figure 3.9: The "dose shadowing" effect, demonstrated by calculating dose on end-inspiration and end-expiration of a 4D-CT and comparing the distributions. The difference image (A) between the end-inspiration phase CT and end-expiration phase CT highlight changes in anatomy due to motion. The gamma (γ) index distribution for a single oblique beam (B) shows the streaks of dose disagreement behind the moving anatomy. Reproduced with permission from Riegel *et al.* (Riegel *et al.*, 2008)

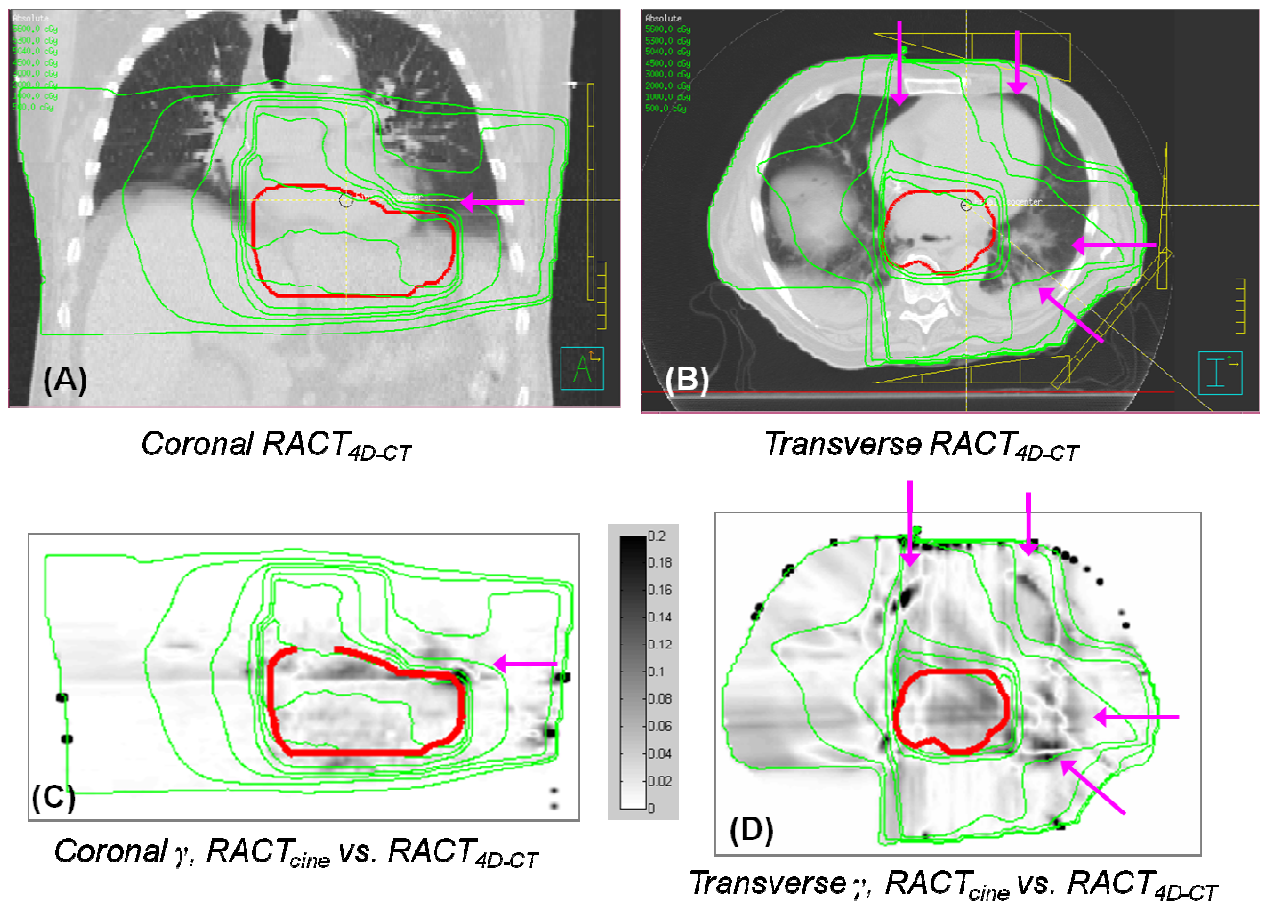


Figure 3.10: Shadowing effect seen in patient 20 of the primary group. Pink arrows highlight areas of moving anatomy on the coronal $RACT_{4D-CT}$ (A) and transverse $RACT_{4D-CT}$ (B). Stripes of disagreement can be seen medial to the beam entrances behind the moving anatomy. Reproduced with permission from Riegel *et al.* (Riegel *et al.*, 2008)

This geometric ambiguity could be remedied by performing a true 3-D γ analysis, not a 2-D γ analysis of 3 orthogonal planes of dose through the isocenter as executed in this chapter. At the time this study was performed, no such analytical tool existed at our institution. Spezi *et al.* suggested that an approximate 3-D γ analysis could be created performing 2-D γ analyses on successive dose planes and “stacking” the slices to form a 3-D γ distribution (Spezi *et al.*, 2006). Several authors have demonstrated, however, that indices in a full 3-D γ distribution are less than indices in a “stack” of 2-D γ distributions (Gillis *et al.*, 2005; Spezi *et al.*, 2006; Wendling *et al.*, 2007). Given the low γ indices encountered in this chapter, we do not expect a “stacked” 3-D analysis or a true 3-D

analysis (which would produce lower values than a stacked analysis) to yield significant (if any) failures using our established criteria.

We had originally anticipated that irregular respiratory patterns would be less affected by the over-emphasis averaging than regular respiratory patterns. As explained briefly in section 3.3.1, for regular respiratory patterns, the same fraction of the respiratory cycle is emphasized at each couch position. The over-emphasized *phase*, however, is different each time. The results of section 3.4.1 and Figure 3.4 and Figure 3.5 have shown this to be untrue: Disagreement was approximately twice greater for 1, 1.5, and 2 breathing cycle RAC_{cine} image sets visualizing irregular respiratory motion. This greater disagreement can most likely be attributed to extreme changes in respiratory amplitude, which can produce severe artifacts on RACT images (Gould et al., 2008). Recall, however, that respiratory patterns were classified as “regular” and “irregular” by *period* not *amplitude*. Respiratory frequency and amplitude are often correlated (Davis et al., 1975), which would explain why artifacts caused by irregular amplitude would show up with patients separated by irregularity of respiratory period. These artifacts are localized to the “slabs” of tissue imaged at each couch position defined by the beam width, but may occur at multiple couch positions if the irregularity persists through the entire scan.

The results of Chapter 2 and Chapter 3 suggest that increasing the CD during cine CT acquisition will produce better results for both target delineation (to better capture the extremes of an irregular breathing pattern) and dose calculation. Increasing CD, however, increases scan time and patient dose. Previous experience with cine CT has shown that RAC_{cine} and MIP_{cine} can be produced using as little as 40 mA and still maintain acceptable image quality, which could drastically reduce patient dose from a cine CT scan (Pan et al., 2007).

While the negligible differences between RAC_{cine} and RAC_{4D-CT} for dose calculation is encouraging, it is important to note that the similarity of RAC_{cine} to RAC_{4D-CT} for dose calculation does not necessarily imply similarity of RAC_{cine} to 4-D dose calculation. We did not explicitly compare RAC_{cine} to 4-D dose calculation. This topic should be investigated.

Given the low γ indices produced in spite of conservative 2%/1mm γ criteria, however, we do not expect that additional differences would be significant.

3.6 Conclusions

The previous two chapters focused on applying image sets processed from cine CT to different, but equally important, parts of the treatment planning process: Target delineation (Chapter 2) and dose calculation (Chapter 3). For tumors influenced by respiratory motion, RACT generated from unsorted cine CT images provided a similar environment for dose calculation as RACT generated from sorted, 10-phase 4D-CT images. Substituting $RACT_{\text{cine}}$ for $RACT_{4\text{D-CT}}$ for the purposes of dose calculation can provide centers without 4D-CT access to an image set that may emulate 4-D dose calculation.

The results of the previous two chapters support the over-arching hypothesis that image sets processed from cine CT can be used for treatment planning of mobile thoracic lesions. As described in section 2.6, however, target delineation was only shown for small lesions. The next chapter explores the incorporation of PET/CT to aid in segmentation of larger mobile tumors using an automatic segmentation algorithm.

Chapter 4 SEGMENTATION OF MOVING TARGETS WITH PET/CT: CORRELATION OF THRESHOLDS WITH LESION SIZE, MOTION EXTENT, AND SOURCE-TO-BACKGROUND RATIO

4.1 Introduction

The use of fluorodeoxyglucose positron emission tomography (FDG-PET) in the treatment planning process for lung cancer has become popular in recent years due to evidence that data from PET imaging can significantly change various aspects of treatment. Several studies have found that incorporating PET information into CT simulation can change treatment intent from curative to palliative (Brink et al., 2004; Ciernik et al., 2003; Dizendorf et al., 2003; Mah et al., 2002), reduce interobserver variation (Ashamalla et al., 2005; Caldwell et al., 2001; Ciernik et al., 2003; Mah et al., 2002), and alter GTV delineation where PET effectively discriminates between malignant tissue and atelectasis (Ashamalla et al., 2005; Erdi et al., 2002; Nestle et al., 1999; van Baardwijk et al., 2006). Recall from Chapter 2 that we successfully demonstrated target delineation of small, mobile stage I NSCLC using image sets processed from cine CT, but based on findings by Muirhead et al. (Muirhead et al., 2008) and common clinical experience at M. D. Anderson, we anticipated that these image sets alone would be insufficient for treatment planning of larger tumors. We hypothesized that PET would provide additional information to make target delineation possible.

Target volume delineation of lung cancer with PET/CT has been extensively reported in the literature (Biehl et al., 2006; Black et al., 2004; Brambilla et al., 2008; Caldwell et al., 2003; Davis et al., 2006; Drever et al., 2007; Erdi et al., 1997; Nestle et al., 2005; Okubo et al., 2008; Park et al., 2008; Paulino et al., 2004), yet little consensus exists on exactly how to use PET to define a GTV (van Baardwijk et al., 2006). One of the first studies by Erdi *et al.* found that 36-44% of maximum activity concentration (AC_{max}) correlated well with known sphere volumes in a stationary phantom (Erdi et al., 1997). In a later publication, the group settled on a single threshold of 42% (Erdi et al., 2002). Paulino *et al.* suggested an SUV

threshold of 2.5 g/mL (Paulino et al., 2004), a value that originated from differentiation of benign versus malignant lesions in PET imaging of NSCLC (Patz et al., 1993).

Subsequent publications questioned the use of a single threshold and proposed other techniques. As described in section 1.2, several studies show that target size and source-to-background ratio (SBR) are important parameters (Biehl et al., 2006; Brambilla et al., 2008; van Baardwijk et al., 2007). Nestle *et al.*, in an attempt to incorporate background into the contouring scheme, proposed thresholds at 15% of mean activity concentration plus background activity concentration (Nestle et al., 2005). Black *et al.*, using phantom scans of different-sized spheres, developed a linear function of mean standardized uptake value (SUV_{mean}) (Black et al., 2004). Few studies, however, investigated motion as a parameter for threshold-based automatic segmentation of the PET image. Caldwell *et al.* found conventional segmentation techniques produced volumes too small to cover the motion extent of the tumor on PET imaging. They suggested using a threshold at 15% of AC_{max} to include motion (Caldwell et al., 2003). In a subsequent study attempting to define a motion-inclusive tumor volume, Okubo *et al.* found that 35% was the optimal threshold for large stationary or moving spheres. Given the shortcomings of single threshold values for stationary objects, however, the validity of single-threshold values for segmentation of motion-inclusive target volumes remains questionable.

4.2 Purpose

The purpose of this chapter was to develop a threshold-based segmentation technique that accounted for tumor size, motion, and SBR. We therefore modeled activity concentration threshold dependence on object volume, motion amplitude, and SBR for moving targets using an extensive series of phantom scans performed at varying object volume, motion, and SBR. We validated the model with 24 lung tumors that were imaged with 4D-CT and PET/CT for radiation therapy simulation and compared IGTVs formed with our model to IGTVs formed with 6 segmentation methods previously reported in the literature (Black et al., 2004; Caldwell et al., 2003; Erdi et al., 1997; Nestle et al., 2005;

Okubo et al., 2008; Paulino et al., 2004). A reliable segmentation technique that incorporates volume, motion, and SBR into threshold determination could provide radiation oncologists with a tool to segment tumors whose contrast on cine CT image sets is insufficient for tumor delineation.

4.3 Methods

4.3.1 Terminology

For clarity, terminology and notation used in this chapter will be summarized in this section. Many segmentation methods utilize activity concentration (AC) or standardized uptake value (SUV) measurements in some way. AC is typically in units of Becquerel per milliliter (Bq/mL). SUV for voxel i is defined in equation (7) as the AC of the voxel AC_i divided by the injected activity A_0 in Bq normalized to patient mass in grams (M). Defined as such, the units of SUV are grams per milliliter (g/mL). One can make SUV unitless by normalizing to density of soft tissue, which is assumed equal to that of water (1 g/mL). Pixel-by-pixel densities are not used to normalize SUV.

$$SUV_i = \frac{AC_i}{A_0/M} \quad (7)$$

Maximum activity concentration will be denoted AC_{max} . A threshold value will be denoted $AC_{n\%}$. For example, 15% of AC_{max} is described as $AC_{15\%}$. Mean activity concentration, which requires an ROI in which to take the mean, is denoted $\overline{AC_{n\%}}$ which can be interpreted as “mean activity concentration of voxels above n% of AC_{max} . All ROIs in this chapter were formed using seed-based region growing (thresholds were not applied to the entire image), so all ROIs are closed shapes. Mean activity concentration in background is designated by $\overline{AC_{BG}}$. ROIs produced from these methods will be denoted similarly. For example, the IGTV produced by taking all voxels above 15% of AC_{max} will be indicated “IGTV_{15%}.” More complex methods will be defined accordingly.

It is also worthwhile to review the distinction between “GTV” and “IGTV,” as both will be included in the discussion with reference to the literature. “IGTV” is a term coined by M. D. Anderson and is not recognized outside the institution. In this chapter, the term “GTV” will be used when motion was neglected or there was no intent to capture motion. For example, when a study investigated delineation of gross tumor with a free-breathing helical CT where no attempt was made to incorporate motion information (whether through inhale/exhale breath-holds, expanding to ITV, etc.), the gross tumor volume is “GTV.” IGTV will be used to reference gross tumor volume with a motion envelope included, in other words, where the *intent* was to capture motion. Most papers in the literature explore GTV delineation, not IGTV delineation. In fact, 4 of the 6 segmentation methods utilized in this study were not originally intended to form IGTVs. It is, however, our intention to include motion and compare with a motion-inclusive ROI, so all segmented ROIs in this chapter will be referred to as “IGTV.”

4.3.2 Development of the Regression Model

4.3.2.1 Phantom Scanning

The goal of the phantom scans was to determine the AC threshold on PET ($IGTV_{PET_n\%}$) which best matched the IGTV defined on cine CT ($IGTV_{CT}$) for a range of sphere sizes, motion extents, and SBRs. The best-matched thresholds would then be used to develop a segmentation model with linear regression techniques.

The NEMA IEC thorax phantom (Data Spectrum, Chapel Hill, NC) was used to form the regression function. The phantom has 6 spheres of varying size set inside a background tank. The 6 spheres had inner diameters equal to 10, 13, 17, 22, 28, 37 mm. These spheres and the background tank were filled to 6 SBRs: 5:1, 10:1, 15:1, 20:1, 30:1, and 50:1. A sinusoidal motion platform was placed on the flat couch of a General Electric Discovery VCT 64-slice PET/CT scanner (GE Health Care, Waukesha, WI). The phantom was placed on the motion platform (Figure 4.1) and moved sinusoidally with a range of motion amplitudes (0,

5, 10, 15, 20, 25, 30 mm peak-to-peak) and 4 second period. The amplitude and period of the sinusoidal motion were chosen to represent typical motion extent (Liu et al., 2007; Stevens et al., 2001) and respiratory frequency (Pan et al., 2006). To summarize, 6 spheres imaged per motion amplitude per SBR, with 7 amplitudes and 6 SBRs requires 42 PET scans to capture 252 combinations of the 3 variables.

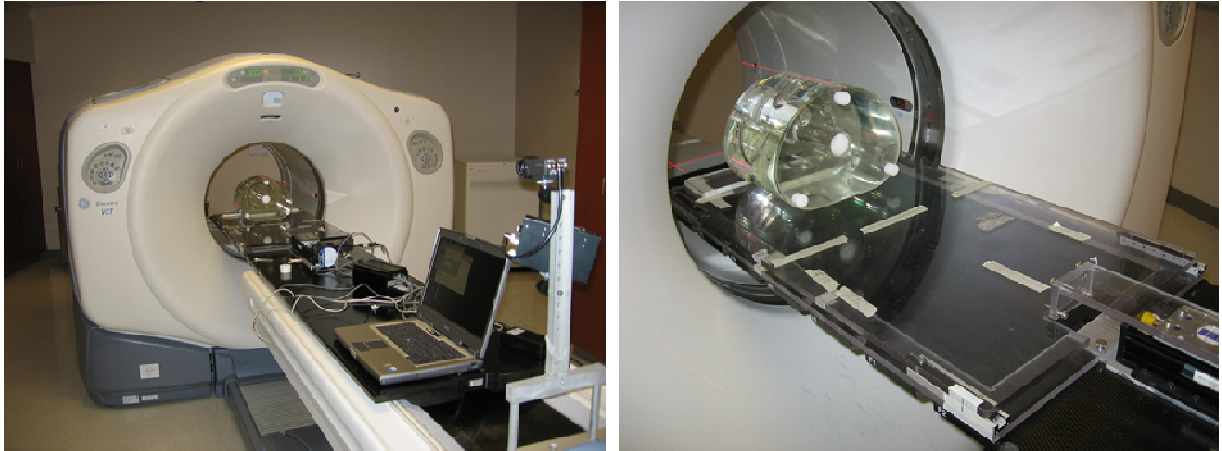


Figure 4.1: NEMA IEC thorax phantom on 1-D motion on flat couch of GE Discovery VCT PET/CT scanner. Reproduced with permission from Riegel *et al.* (Riegel *et al.*, 2010)

Coincidence data were collected for 18 minutes in 3-D mode and were recorded through list-mode acquisition at each motion extent and SBR. After completion of the scan, the volume imaging protocol (ViP) replay feature was used to split the 18 minute scan into three 6-minute scans for repeatability. Images were reconstructed using ordered-subsets expectation maximization (OSEM) reconstruction, 21 subsets and 2 iterations at 50 cm field of view. Using a 128×128 image matrix, voxel sizes were 3.9 by 3.9 by 3.3 mm. PET images were transferred to a commercial treatment planning system (Pinnacle³, version 8.1w, Philips Medical Systems, Milpitas, CA) for delineation of the 6 spheres.

Cine CT was used to capture motion envelopes at each extent to obtain the reference volume. The spheres were drained of liquid while the background tank was kept filled with water. The scan protocol utilized cine CT at 120 kV, 100 mA, x-ray collimation of 8×2.5 mm, CD of 4.8 s, cine interval of 0.4 s, and gantry rotation of 0.4 s. In order to contour the maximum motion extent, the minimum intensity projection was produced

directly from the cine CT data ($\text{min-IP}_{\text{cine}}$) with in-house software. Because the spheres were empty and the background tank was full, the $\text{min-IP}_{\text{cine}}$, which records the lowest pixel value over the image sequence, captured the motion path of the empty spheres (Figure 4.2). Furthermore, this method allowed us to capture the inner diameter of the moving sphere, which was consistent with the activity-filled volume imaged by the PET scan. All $\text{min-IP}_{\text{cine}}$ images were transferred to the commercial treatment planning system for contouring.

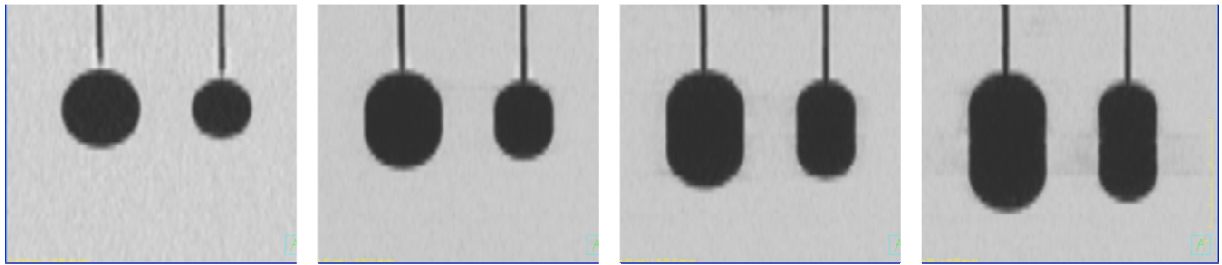


Figure 4.2: Minimum intensity projection from cine CT ($\text{min-IP}_{\text{cine}}$) for 37 and 28 mm diameter spheres of NEMA IEC phantom. From left to right: 0, 10, 20, and 30 mm motion amplitude.

4.3.2.2 Target Delineation

IGTVs of the 6 spheres on the $\text{min-IP}_{\text{cine}}$ images were auto-segmented using seed-based 3-D region growing. These ROIs, termed IGTV_{CT} for this chapter, served as the reference volumes to which PET threshold volumes would be optimized. A threshold of -425 HU was used to limit the region growing algorithm (Goo et al., 2005; Kemerink et al., 1998).

The motion-blurred spheres on PET imaging were segmented by determining AC_{max} in each sphere and auto-segmenting 10-20 ROIs at different percentage thresholds (in 1% intervals) of AC_{max} using seed-based region growing. These ROIs are termed $\text{IGTV}_{\text{PET}_n\%}$. Because PET acquisition occurred on different days for each SBR, care was taken to reposition the phantom on the scanner bed. To further ensure PET/CT registration and

mitigate the effects of phantom repositioning, the centroids of $IGTV_{PET_n\%}$ and $IGTV_{CT}$ volumes were registered.

When $IGTV_{CT}$ and $IGTV_{PET_n\%}$ were contoured for all spheres, motion extents, and SBRs, the ROIs were converted to mesh surfaces using a software tool in the treatment planning system. The mesh surfaces were exported from the treatment planning system and the separation between the surfaces was analyzed by in-house software.

4.3.2.3 Analysis

To assess differences between $IGTV_{CT}$ and each $IGTV_{PET_n\%}$, we developed an algorithm to measure the separation between two mesh surfaces similar to the method used by Pevsner *et al.* which can assess concave volumes (Pevsner et al., 2006). This method was a modification of the method put forth by Remeijer *et al.* (Remeijer et al., 1999) and was recently used by Rietzel *et al.* to compare GTVs drawn on MIP to the union of GTVs from 10-phase 4D-CT (Rietzel et al., 2008). Our technique was developed in MATLAB (Mathworks, Natick, MA) and was termed the “surface separation” algorithm. The main advantage of the surface separation method over simply comparing volume magnitudes (Nestle et al., 2005; Park et al., 2008) or concordance (Giraud et al., 2002) is that this method provides specific geometric information of where the volumes disagree. Furthermore, this information can be visualized in a polar-azimuthal plot (Figure 4.3).

A brief explanation of the surface separation analysis is provided here. For a more detailed description please see the Appendix. First, slice-by-slice contours were converted to a triangular mesh by the treatment planning system (this feature is commonly used in conjunction with model-based auto-segmentation, but is convenient for our purposes as well). Triangular meshes were created for the $IGTV_{CT}$ and $IGTV_{PET_n\%}$ volumes for all n . In the treatment planning system, region of interest (ROI) and mesh information are stored in text files called “plan.roi.” Mesh data are stored in Visualization ToolKit (VTK) format. These data consist of two matrices: First, 3 columns of x , y , and z coordinates which represent the vertices of the mesh; Second, 3 columns of indices which specify how the

vertices are connected to form the triangular mesh surface. Our software extracted this mesh information to recreate the mesh surface in MATLAB.

The software was designed to compare a “test” volume to a “reference” volume. In this particular application, $IGTV_{CT}$ was the reference volume and $IGTV_{PET_n\%}$ was the test volume. The surface separation “operator” will be signified by the “|” character in this chapter. For example, comparing $IGTV_{PET_{27\%}}$ (the test volume) to $IGTV_{CT}$ (the reference volume) is denoted “ $IGTV_{PET_{27\%}}|IGTV_{CT}$ ”. Rays were projected from the centroid of the reference volume at equally-spaced altitudinal and azimuthal angles (in our study, 5° spacing was used). For each ray, we calculated the intersection of the ray and every plane defined by the triangles of the mesh surface to “sample” the reference mesh surface. For each sampling point on the reference mesh, we calculated the closest distance to the test mesh by projecting the sampling point to the planes defined by the triangles of the test mesh surface. Our algorithm was validated using a series of low and high resolution spherical meshes of varying size (Figure 4.3).

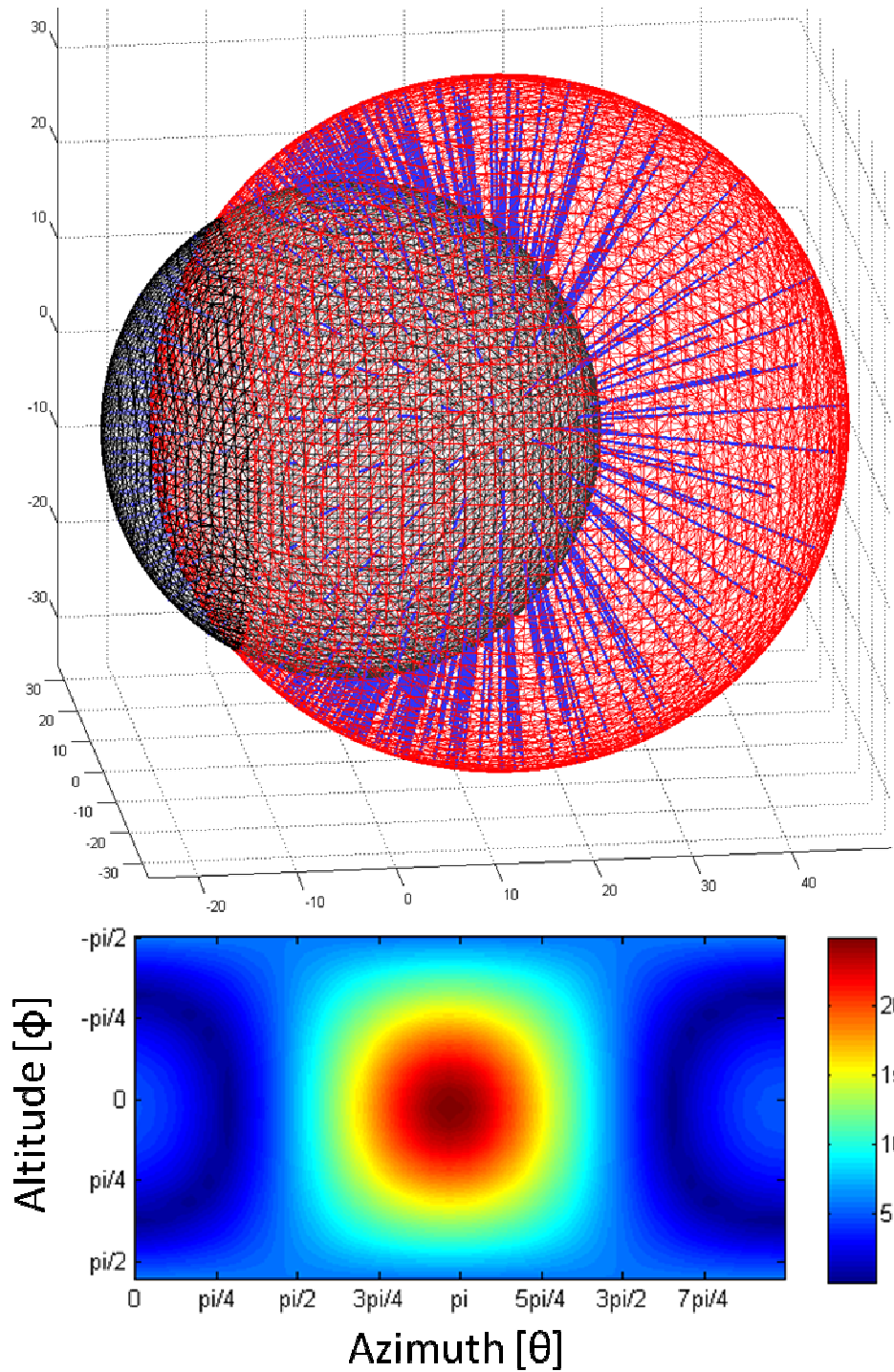


Figure 4.3: (Top) The test mesh (red) is compared with a reference mesh (black) with the surface separation algorithm. Blue lines represent shortest distances between sampling points on the reference mesh and the test mesh surface. (Bottom) Deviations are expressed in terms of altitudinal and azimuthal angles.

In our study, for each sphere volume, motion extent, and SBR, the surface separation algorithm was iterated to compare $IGTV_{CT}$ and $IGTV_{PET_n\%}$, a series of meshes created by different thresholds of AC_{max} . For each iteration, the deviations between the surfaces were squared and summed to determine which threshold $n\%$ produced the minimal sum of squared differences between $IGTV_{CT}$ and $IGTV_{PET_n\%}$. The resulting threshold $n\%$ was the “optimal” threshold for that sphere volume, motion, and SBR. The algorithm was repeated for each of 3 image sets per experimental condition and the average optimal threshold was used for regression.

Multiple regression was utilized to determine a model $f(x,y,z)$ that best described the relationship between volume, motion, and SBR (3 independent variables) and optimal threshold (1 dependent variable). This model was termed the “volume/motion/SBR” model. We first attempted to fit optimal threshold values normalized to AC_{max} , but quickly realized that AC_{max} was substantially degraded by partial-volume averaging (related to object size) and motion blur (related to motion extent). The normalization factor of the dependent variable, therefore, was a function of two independent variables we were fitting against. In order to avoid unnecessary complication in the regression procedure, we normalized the threshold AC values to a background measurement. The mean AC in a spherical ROI at the center of the phantom was used for the background measurement ($\overline{AC_{BG}}$).

Partial volume averaging and motion blur likewise affected the measurement of SBR. We therefore used the SBR measurement for the largest sphere (where the effect of partial volume averaging was minimal) without motion for regression. SBR was defined as the ratio of $\overline{AC_{80\%}}$ and the previously-described $\overline{AC_{BG}}$ as shown in equation (8).

$$SBR = \frac{\overline{AC_{80\%}}}{\overline{AC_{BG}}} \quad (8)$$

SBR was measured 3 times, once on each image set per experimental condition. The average of the 3 SBR measurements was used for regression. Sphere volume was measured

on the treatment planning system using the segmented ROIs from the 0 mm motion condition. Nominal motion values were used in the regression.

We also wanted to examine the relative influence of volume, motion, and SBR on optimal threshold. For this purpose, typical regression coefficients are unreliable; they have different units and different scales from each other and therefore cannot be compared. We can, however, transform the variables such that the mean of each variable is 0 and the standard deviation is 1 and re-run the regression. The resulting regression coefficients, often called *standardized* regression coefficients, allow us to infer relative importance of each variable (Kim et al., 1981). The transformation is shown in equation (9), where x is the unstandardized variable, \bar{x} and s_x are the mean and standard deviation of the unstandardized variable respectively, and x_{std} is the standardized variable. The magnitude of the standardized coefficients, denoted by β_n , represents the relative importance of each term in the regression function.

$$x_{std} = \frac{(x - \bar{x})}{s_x} \quad (9)$$

4.3.3 Application of the Regression Function to Patients

4.3.3.1 Imaging

Lung cancer patients who underwent 4D-CT and PET/CT simulation in the same imaging session were retrospectively included in the study under an IRB-approved protocol if the patient demonstrated one or more solid lesions with relatively homogeneous uptake on PET without invasion into the chest wall or mediastinal regions. PET/CT and 4D-CT simulations were performed on an 8-slice PET/CT scanner (General Electric Discovery ST, General Electric Medical System, Waukesha, WI). The 4D-CT protocol used 120 kV, 100 mA, 0.5 s gantry rotation, 0.25 s cine interval, and cine duration equal to 1 average breathing cycle plus 1 s. For PET imaging, patients were injected with 477 to 740 MBq and PET was acquired in 2-D mode for 3 minutes per bed position from the base of skull to mid-thigh.

Attenuation correction was performed with respiratory-averaged CT (Chi et al., 2007; Pan et al., 2005). Images were reconstructed with OSEM iterative reconstruction utilizing 30 subsets and 2 iterations, with a 3.91 mm FWHM loop filter, 5.45 mm FWHM post filter, and z-axis filtering applied. Both PET and CT imaging used a 50 cm field-of-view with a 128 × 128 and 512 × 512 image matrix respectively, producing pixel sizes of 3.9 mm and approximately 1 mm respectively. PET slice thickness was 3.27 mm and CT slice thickness was 2.5 mm. PET and 4D-CT images were transferred to treatment planning system for contouring.

4.3.3.2 Target Delineation

To form the “reference” IGTV_{CT}, the motion envelope was contoured on the MIP_{cine}. A seed-based 3-D region growing auto-segmentation algorithm was used to minimize observer variation and bias. As with the phantom scans used in model development, a threshold of -425 HU was used to limit the region growing algorithm (Goo et al., 2005; Kemerink et al., 1998). A radiation oncologist reviewed and adjusted the IGTV_{CT} contours if necessary.

Table 4.1: Tumor delineation methods on PET

Study	Delineation Technique	ROI Notation
Caldwell <i>et al.</i> (Caldwell et al., 2003)	15% of AC _{max}	IGTV _{15%}
Okubo <i>et al.</i> (Okubo et al., 2008)	35% of AC _{max}	IGTV _{35%}
Erdi <i>et al.</i> (Erdi et al., 2002)	42% of AC _{max}	IGTV _{42%}
Paulino <i>et al.</i> (Paulino et al., 2004)	SUV = 2.5 g/mL	IGTV _{2.5}
Nestle <i>et al.</i> (Nestle et al., 2005)	15% of $\overline{AC}_{70\%}$ + BG	IGTV _{15%+BG}
Black <i>et al.</i> (Black et al., 2004)	$0.307 \times \text{SUV}_{\text{mean}} + 0.588$	IGTV _{SUVmean}
Riegel <i>et al.</i> (Riegel et al., 2010)	Volume/motion/SBR model	IGTV _{V,M,SBR}

ROI = region of interest

AC_{max} = maximum activity concentration

AC_{mean} = mean activity concentration

SUV = standardized uptake value

BG = background

IGTVs were delineated on PET data sets based on 6 segmentation methods from the literature (collectively referred to as IGTV_{PET}). These methods are summarized in Table 4.1. IGTV_{15%}, IGTV_{35%}, IGTV_{42%}, and IGTV_{2.5} were all single thresholds of AC_{max} or SUV (Caldwell et al., 2003; Erdi et al., 2002; Okubo et al., 2008; Paulino et al., 2004). IGTV_{15%+BG} was more complex, as it was formed by calculating 15% of $\overline{AC}_{70\%}$, adding the result to a background measurement, and setting the threshold at this value. As described in Nestle *et al.*, \overline{AC}_{BG} was measured in a small ROI defined in the adjacent anatomical structure with the highest background activity (Nestle et al., 2005). Though IGTV_{SUVmean} only requires a measurement of SUV_{mean} as input for the linear function, the starting threshold required to measure SUV_{mean} is not specified. The authors address this circular problem by starting at an arbitrary threshold, taking the mean, (we used $\overline{SUV}_{70\%}$) and iterating through the regression function several times, each time producing a new SUV_{mean} for input into the next iteration (Black et al., 2004). As per the author's suggestion, we iterated 5 times. All IGTVs were formed using seed-based region-growing automatic segmentation in the treatment planning system.

IGTV was contoured using our motion-inclusive model by measuring the tumor volume, motion, and SBR and plugging them into the model. Tumor volume and motion were determined by auto-segmenting the end-inspiration and end-expiration phases of the 4D-CT. Volume was measured at end-expiration, and motion was measured as the distance between the end-inspiration and end-expiration centroids. SBR was calculated by equation (8) where \overline{AC}_{BG} was measured by segmenting the ipsilateral lung, removing any areas of high uptake (tumors, inflammation, imperfect segmentation near the mediastinum, etc.), and measuring mean AC in the remaining lung voxels (van Baardwijk et al., 2007). IGTV produced using the volume/motion/SBR model (IGTV_{V,M,SBR}) was created by seed-based region-growing auto-segmentation of the PET images. Prior to threshold calculation, however, a recovery coefficient (described in the next section) was applied to the SBR.

4.3.3.3 Recovery Coefficient

The measured SBR value was degraded by partial volume averaging (Soret et al., 2007) and tumor motion (Boucher et al., 2004). Recall that *true* SBR was used for multiple regression to develop our model (section 4.3.2.3). We therefore corrected for size and motion degradation by multiplying the degraded SBR by a recovery coefficient (RC). The RC was developed from the phantom data. $\overline{AC}_{80\%}$ for each sphere size and motion condition was compared with the largest stationary sphere, such that the RC for each size and motion condition was defined as:

$$RC(x, y) = \frac{\overline{AC}_{80\%}(26.5, 0)}{\overline{AC}_{80\%}(x, y)} \quad (10)$$

where x is volume in cubic centimeters and y is extent of motion in millimeters. RCs were averaged over the 3 phantom trials. The largest nominal sphere volume is 26.5 cm^3 and “0” represents the stationary scan condition. Multiple regression was used to fit an RC function of volume and motion. Recovered SBR is simply the product of the degraded SBR and the RC for the size and motion of the object of interest.

4.3.3.4 Analysis

The AC thresholds that best matched $IGTV_{CT}$ were determined for each patient in the same manner as the phantoms. ROIs were segmented on PET images at a range of $AC_{n\%}$ at 1% intervals of AC_{max} . Each threshold volume was compared with $IGTV_{CT}$ using the surface separation tool. The threshold that produced the minimal sum of squares was considered the “best fit” threshold. This provided an independent standard to compare against performance of the segmentation techniques. AC thresholds produced by each of the 7 segmentation methods were correlated with the measured “best fit” AC threshold.

Each $IGTV_{PET}$ was geometrically compared with $IGTV_{CT}$ two ways: First, by measuring the magnitude of each $IGTV_{PET}$ and $IGTV_{CT}$ volume, and second, by measuring the surface

separation between each $IGTV_{PET}$ and $IGTV_{CT}$ using the algorithm described in section 4.3.2.3. Using this tool, we calculated the mean surface separation between $IGTV_{CT}$ and each $IGTV_{PET}$ ($IGTV_{PET}|IGTV_{CT}$). We were, essentially, comparing radius (via surface separation) and volume of the IGTVs, similar to the analysis of Nestle *et al.* in which the authors calculated the virtual radius of the tumor from the measured volume assuming a spherical shape (Nestle et al., 2005). $IGTV_{PET}$ volume magnitudes were compared with $IGTV_{CT}$ for statistically significant differences by log-transforming the data to ensure normality (Limpert et al., 2001) and performing a paired t-test ($\alpha=0.05$). Surface separation for each $IGTV_{PET}|IGTV_{CT}$ pair was compared with $IGTV_{V,M,SBR}|IGTV_{CT}$ using a paired t-test ($\alpha=0.05$).

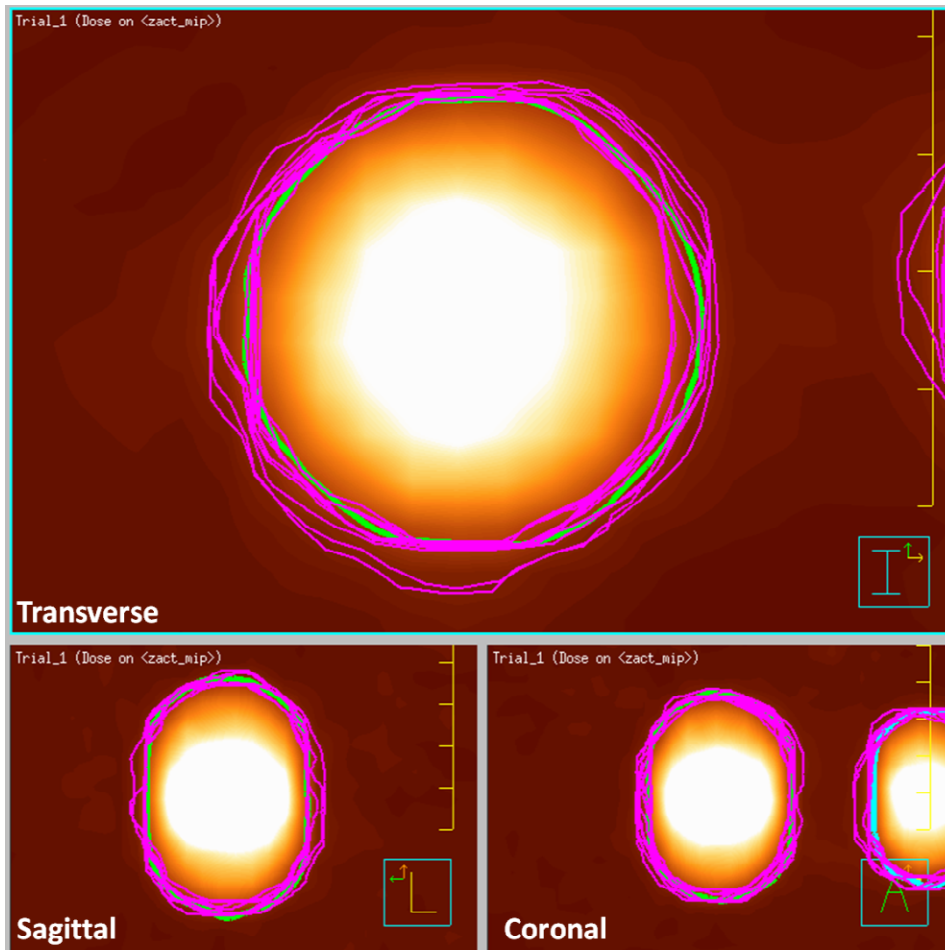


Figure 4.4: Transverse, sagittal, and coronal PET images of the 37 mm inner diameter sphere moving at 20 mm sinusoidal motion amplitude. The green contour represents $IGTV_{CT}$ derived from cine CT. Purple contours represent $IGTV_{PET_n\%}$ at a range of activity concentration thresholds. The optimal threshold (the threshold that created the purple ROI most similar to the green ROI) was determined with the surface separation algorithm. Reproduced with permission from Riegel *et al.* (Riegel et al., 2010)

4.4 Results

4.4.1 Volume/Motion/SBR Segmentation Model

PET images for each of the 252 combinations of volume, motion, and SBR were segmented as described in section 4.3.2.2. An example of these contours is shown in Figure 4.4. Approximately 20 percentage thresholds were contoured for each volume/motion/SBR combination, resulting in approximately 5000 ROIs to analyze with the surface separation algorithm. Optimal thresholds were unable to be determined for 5 volume/motion combinations at SBR of 5:1 (1.2 cm³ at 30 mm motion, 0.5 cm³ at 15-30 mm motion). The substantial motion blurring caused the spheres to be indiscernible from background. Nominal sphere volume and SBR versus measured values used for regression are shown in Table 4.2. Note that ROIs segmented with a -425 HU threshold are within ± 1 mm (approximately 1 CT pixel) of the sphere's true inner radius.

Table 4.2: Nominal and actual volumes and SBRs

Volume (cm ³)		SBR (unitless)	
Nominal	Measured	Nominal	Measured
26.5	28.6	5	4.33 \pm 0.02
11.5	12.7	10	8.12 \pm 0.25
5.6	6.4	15	14.88 \pm 0.22
2.6	3.1	20	19.91 \pm 0.73
1.2	1.4	30	28.88 \pm 1.40
0.5	0.7	50	52.15 \pm 1.95

SBR = source-to-background, measured in the largest stationary sphere

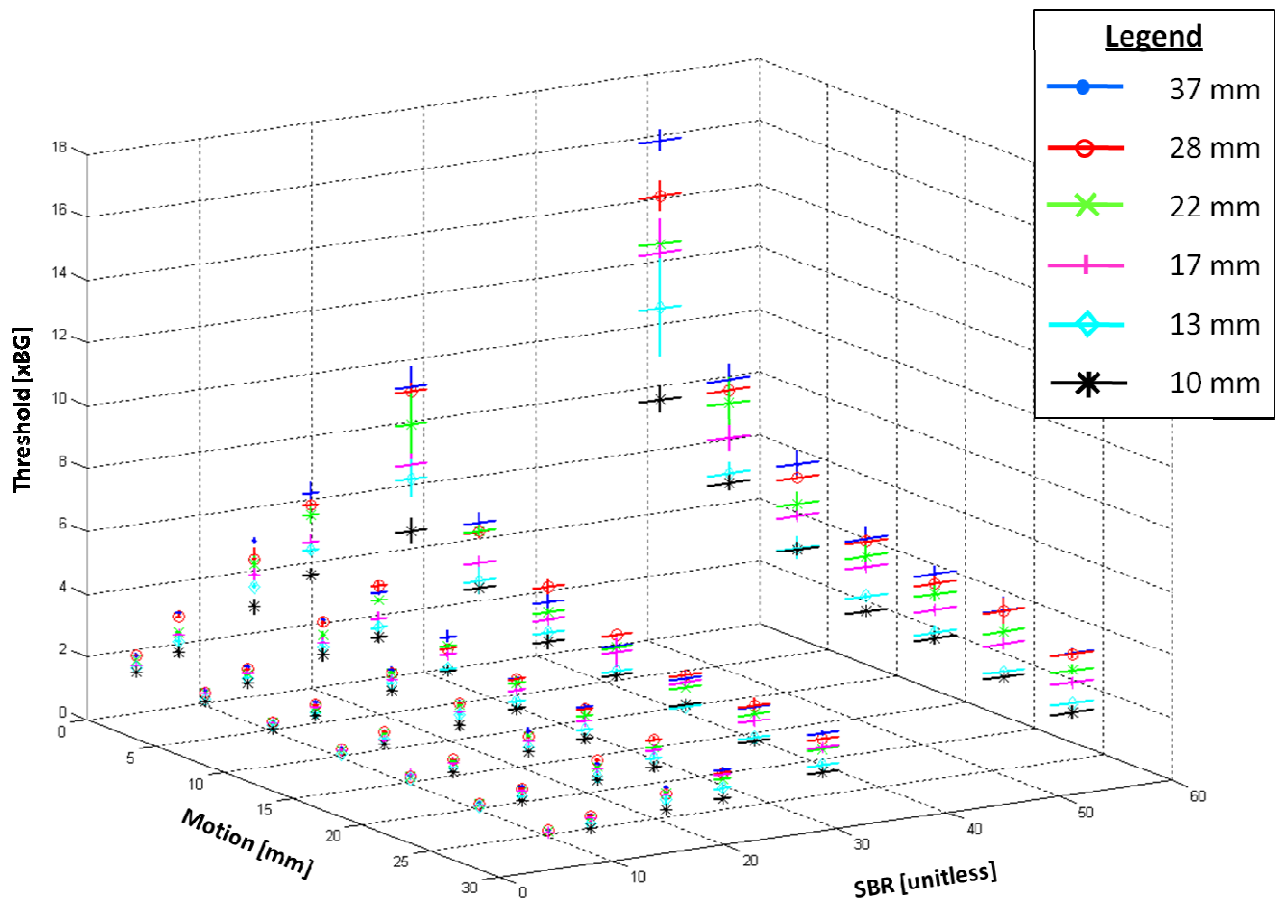


Figure 4.5: Optimal thresholds (normalized to background) versus motion, source-to-background (SBR), and sphere volume. Volume is denoted by the different colors and symbols shown in the legend (which lists nominal sphere diameters). Error bars represent 1 standard deviation. Reproduced with permission from Riegel *et al.* (Riegel *et al.*, 2010)

Figure 4.5 is a 3-D scatter plot of the optimal thresholds for each of the 252 combinations of volume, motion, and SBR. Since our data is four-dimensional and is therefore difficult to visualize, motion, SBR, and optimal threshold were placed on separate axes, with sphere inner diameter represented by different symbols and color for each value. There are clear patterns to the data and isolating the patterns by keeping one variable constant is helpful to suggest terms for the regression model. The relationship of optimal threshold with SBR, for example, is close to linear (Figure 4.6). Optimal threshold versus motion and volume, however, are more complicated (Figure 4.7 and Figure 4.8). After trying several combinations of functions that were physically appropriate to the phenomena (quadratic functions, for example, were not considered because there is no reason to expect maxima or minima, and therefore do not make sense physically), we settled on the model shown in equation (11). Threshold normalized to background is denoted by w , x is volume in cubic centimeters, y is motion in millimeters, z is SBR (unitless), and B_n are the regression coefficients.

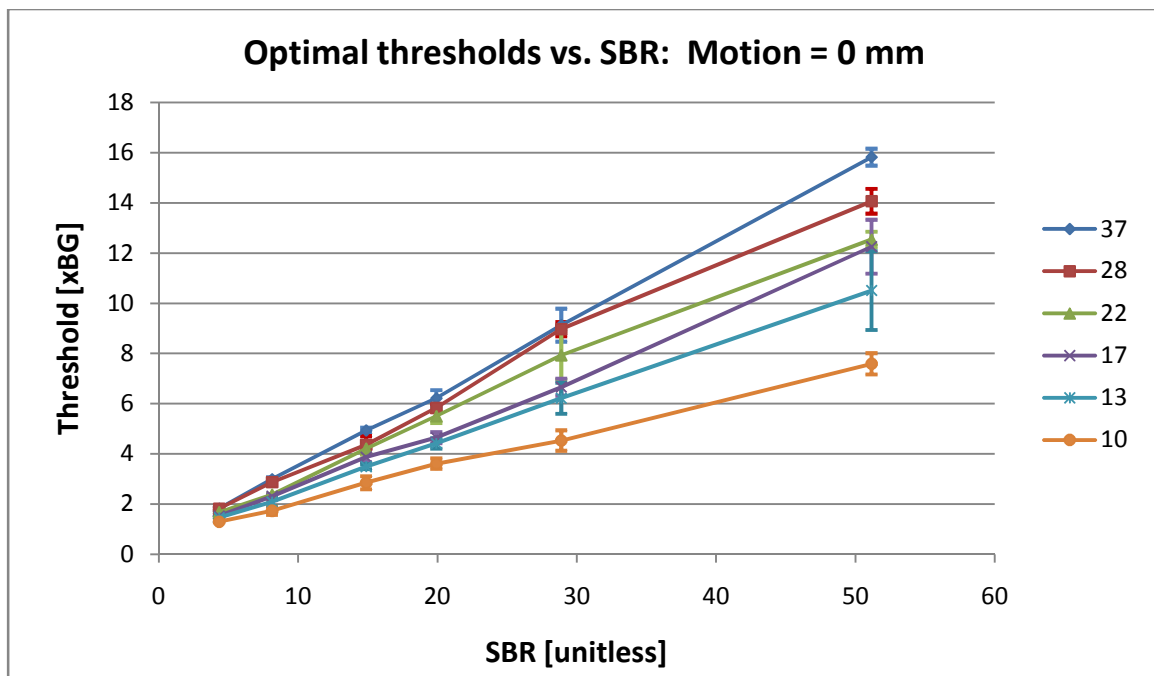


Figure 4.6: Optimal threshold versus source-to-background for stationary spheres. Each line represents a different sphere diameter as denoted in the legend. Note the linear nature of the relationship. Error bars are 1 standard deviation (3 measurements). Reproduced with permission from Riegel *et al.* (Riegel et al., 2010)

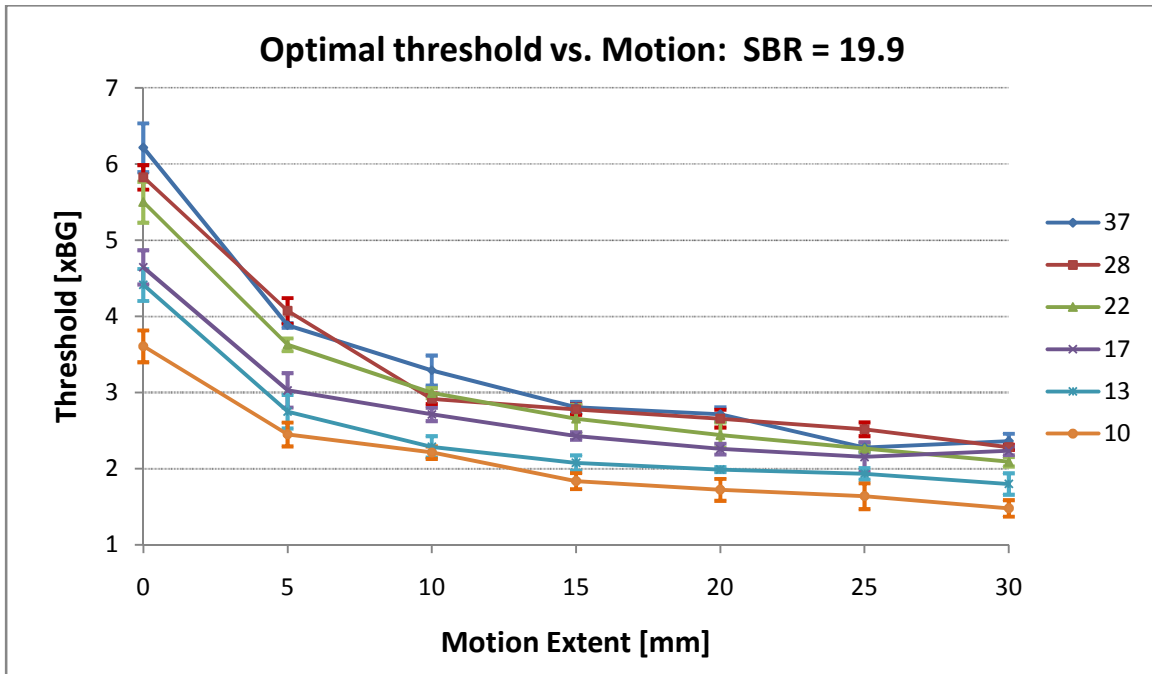


Figure 4.7: Optimal threshold versus motion for source-to-background = 19.9. Each line represents a sphere diameter as shown in the legend. Error bars are 1 standard deviation (3 measurements). Reproduced with permission from Riegel *et al.* (Riegel *et al.*, 2010)

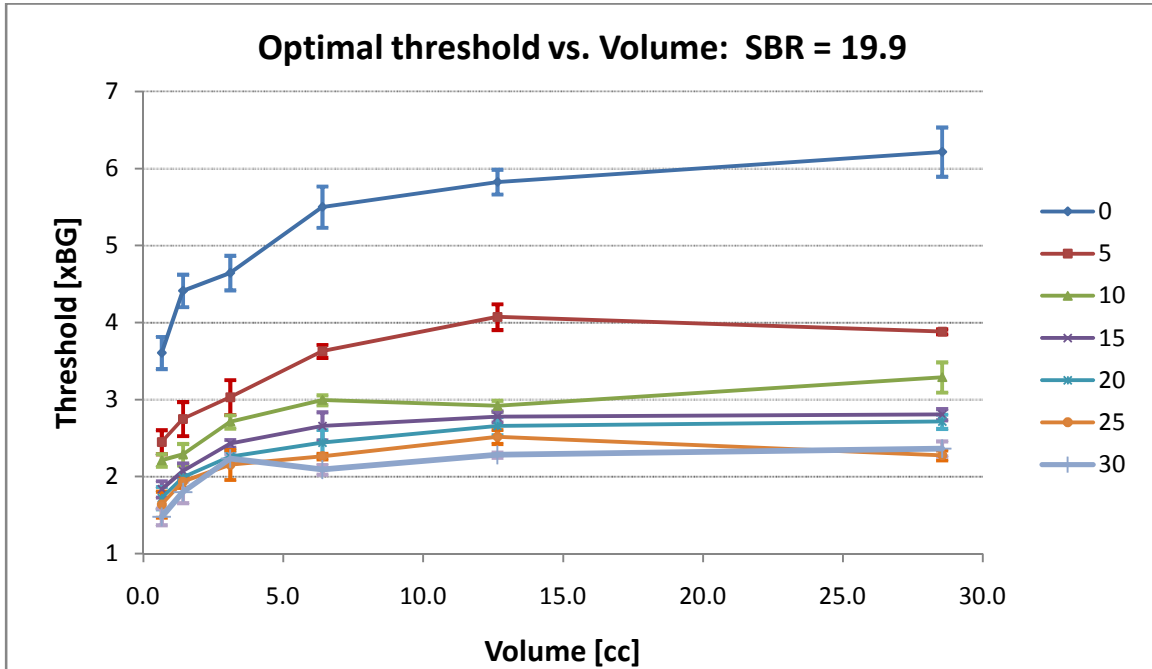


Figure 4.8: Optimal threshold versus volume for source-to-background = 19.9. Each line represents motion extent (0 mm to 30 mm). Error bars are 1 standard deviation (3 measurements). Reproduced with permission from Riegel *et al.* (Riegel *et al.*, 2010)

$$\ln(w) = B_1x^{1/3} + B_2y^{1/3} + B_3 \ln(z) + B_4 \left(x^{1/3} \ln(z)\right) + B_5 \left(y^{1/3} \ln(z)\right) + B_6(xy)^{1/3} + B_7 \quad (11)$$

There are a few noteworthy aspects of this equation. First, because the residuals increased with increasing SBR, we took the natural logarithm of the threshold values w . We therefore took the natural log of SBR in the model to maintain the previously linear relationship with optimal threshold. For volume, the choice of cube root is not entirely surprising because radius is proportional to the cube root of volume. For motion, we originally tried a logarithmic function. We measured optimal threshold, however, at a motion extent of 0 mm and log is undefined at zero. A cube root, therefore, was chosen because it behaves similarly to natural log but is defined at zero. The second three terms in the equation are interaction terms and were included in the model because we found their inclusion created a substantially better fit to the data.

$$\ln(w) = 0.0634x^{1/3} + 0.12y^{1/3} + 0.7327 \ln(z) + 0.0597 \left(x^{1/3} \ln(z)\right) - 0.12 \left(y^{1/3} \ln(z)\right) - 0.025(xy)^{1/3} - 0.9504 \quad (12)$$

The volume/motion/SBR model with regression-determined coefficients is shown in equation (12). This function produced an R^2 value of 0.96 and an adjusted R^2 value (which accounted for increasing R^2 due to additional terms in the fitting function) of 0.96. Several surfaces of the regression function (because the function is a family of surfaces) are shown in Figure 4.9.

The standardized regression coefficients, often denoted as β_n , are listed in Table 4.3. Of the 3 independent variables, SBR was the most influential ($\beta_3 = 1.0606$), followed by motion ($\beta_2 = 0.2114$), then volume ($\beta_1 = 0.0841$). Both interaction terms with SBR, however, were more influential than motion and volume alone.

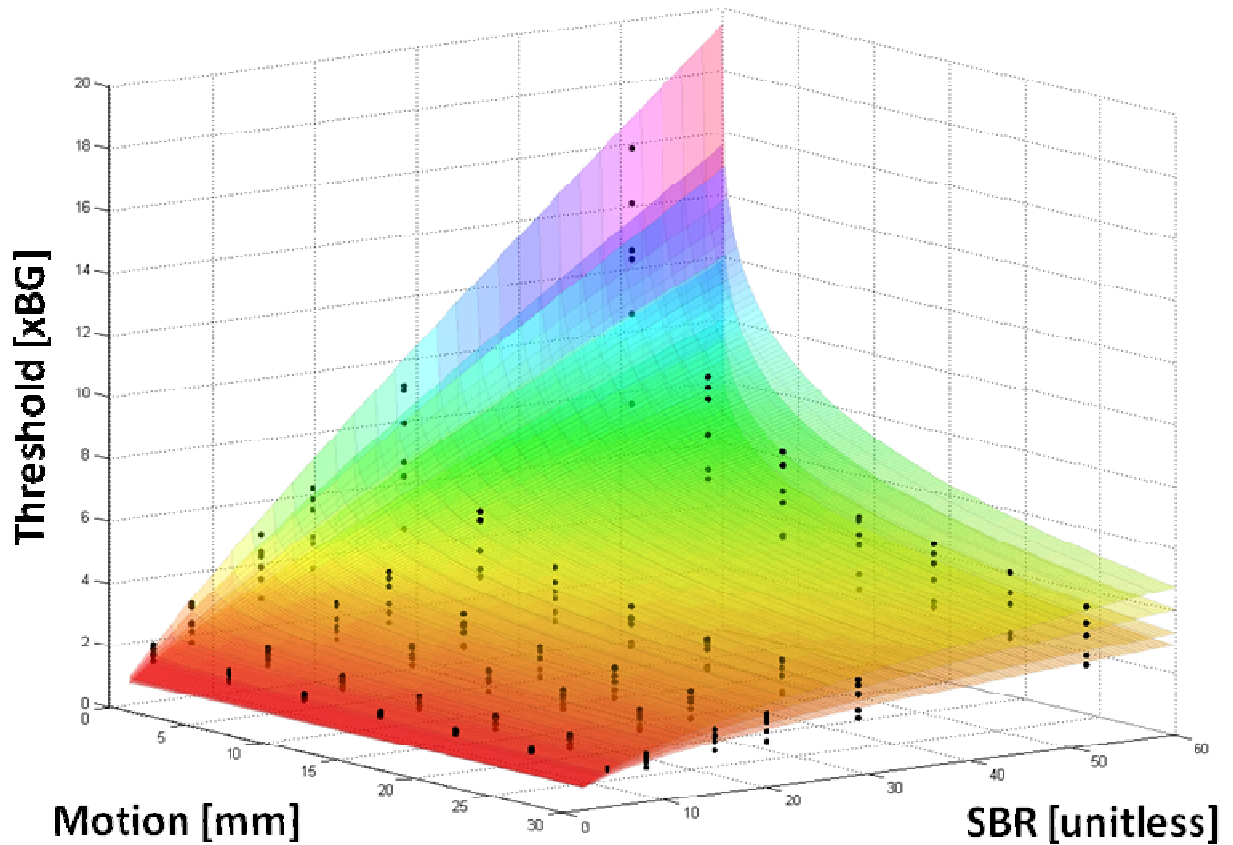


Figure 4.9: Surfaces of regression function defined in equation (12). Each of the 4 surfaces displayed is calculated for spheres of inner diameter 10, 17, 28, and 37 mm. Reproduced with permission from Riegel *et al.* (Riegel et al., 2010)

Table 4.3: Regression coefficients for model in equation (11).

Variable	B_n	β_n
Volume	0.0634	0.0841
Motion	0.12	0.21
SBR	0.7327	1.0606
Volume • SBR	0.0597	0.275
Motion • SBR	-0.12	-0.73
Volume • Motion	-0.025	-0.110
Constant	-0.9504	-0.0321

B_n = unstandardized regression coefficients

β_n = standardized regression coefficients

“•” denotes interaction term

4.4.2 Application to Patient Studies

The RC function developed from phantom data ($R^2=0.95$) is shown in equation (13). Again, x is volume in cubic centimeters and y is motion extent in millimeters. Volume and motion measurements were plugged into equation (13), and the degraded SBR and RC were multiplied to obtain the recovered SBR.

$$RC(x, y) = 0.199x^{-1} + 0.014y + 0.073x^{-1}y + 0.8839 \quad (13)$$

Twenty-four tumors (23 patients) scanned from May 2004 to February 2009 fit our criteria, were adequately registered, and were included in the analysis. $IGTV_{15\%}$ could not be segmented for 6 tumors because $AC_{15\%}$ fell below background AC. Similarly, $IGTV_{2.5}$ could not be segmented for 2 tumors for the same reason. As such, t-tests were performed with paired values, limiting the sample to 18 and 22 tumors respectively.

Volume, motion, and SBR measurements for the 24 tumors as well as threshold values calculated from the volume/motion/SBR model are shown in Table 4.4. Linear correlations ($y = mx+b$) of the measured “best fit” threshold value and the threshold predicted by each segmentation technique for every patient are shown in Figure 4.10. The correlation of $IGTV_{V,M,SBR}$ thresholds with measured values has the slope closest to 1 ($m = 0.8991$) implying good correlation of predicted with best-fit values, the y-intercept closest to 0 ($b = 1.3963$) implying little systematic over- or underestimation, and the highest R^2 value ($R^2 = 0.8577$).

Table 4.4: Volume, motion, and source-to-background characteristics of 24 lung tumors, with model-produced threshold

Tumor	Volume (cm³)	Motion (mm)	Corrected SBR	Threshold
1	21.1	10.8	30.07	4.3685
2	15.3	7.8	26.37	4.1071
3	1.1	10.3	7.21	1.4395
4	0.8	6.2	48.19	4.3495
5	1.0	6.6	19.63	2.6316
6	28.0	1.5	13.47	3.6915
7	2.5	13.6	18.38	2.3723
8	1.5	2.4	25.08	3.6546
9	0.7	4.6	20.17	2.7718
10	0.6	2.2	13.05	2.3129
11	13.6	1.0	39.76	7.6571
12	1.1	8.0	5.49	1.2723
13	10.3	8.6	25.90	3.7288
14	0.4	8.8	13.41	1.9457
15	3.6	4.0	7.87	1.7821
16	2.2	15.0	8.57	1.5572
17	4.8	3.1	9.19	2.0621
18	2.7	2.7	25.17	3.8271
19	0.7	1.5	20.59	3.2432
20	1.6	6.3	29.31	3.4625
21	1.5	2.7	14.60	2.5703
22	5.2	0.6	17.73	3.7687
23	0.1	1.0	11.52	2.1201
24	0.5	5.1	23.55	2.9347

SBR = source-to-background ratio

Threshold is normalized to background and is therefore unitless.

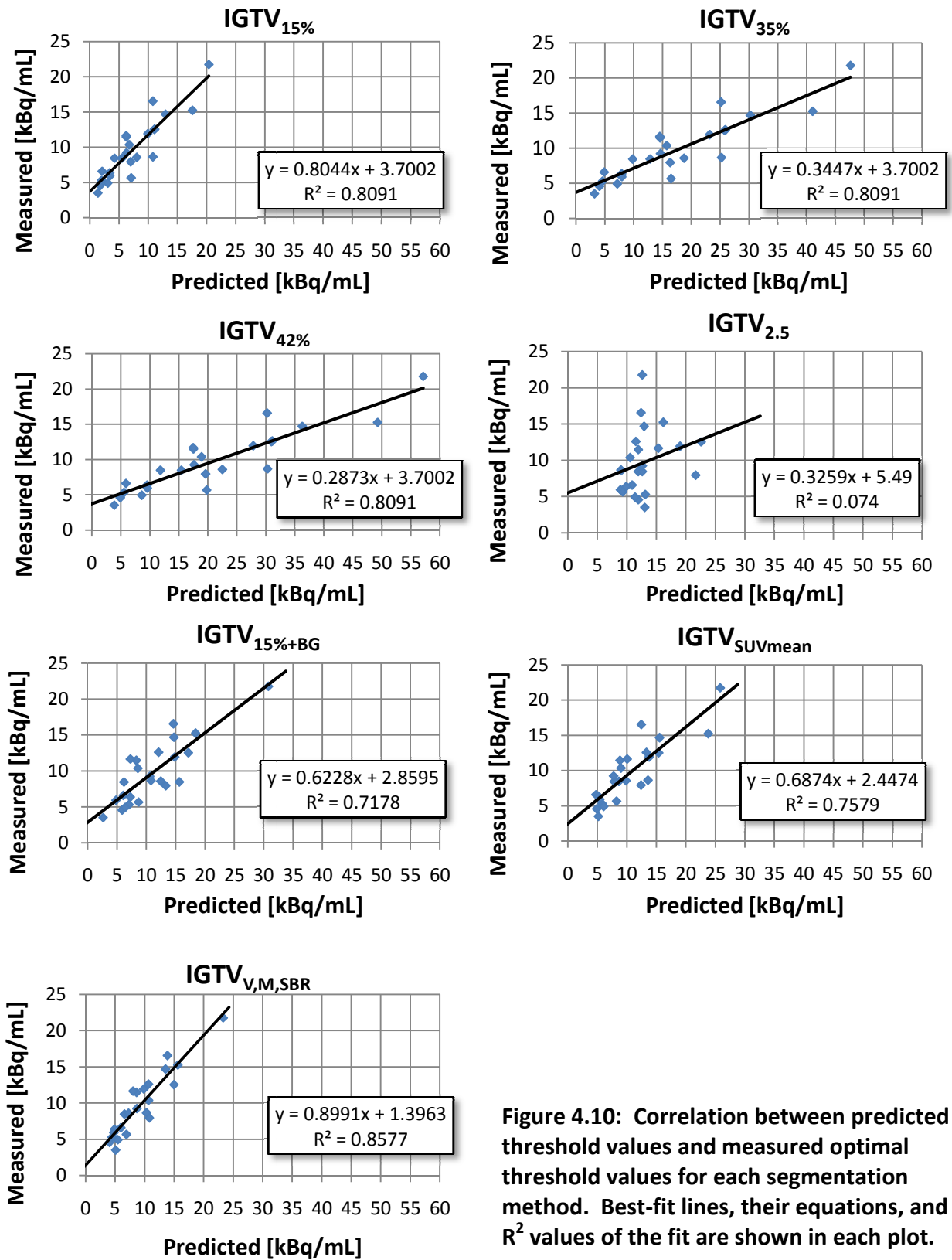


Figure 4.10: Correlation between predicted threshold values and measured optimal threshold values for each segmentation method. Best-fit lines, their equations, and R^2 values of the fit are shown in each plot.

Figure 4.11 shows IGTVs contoured for each delineation method for tumor 13, a typical case. $IGTV_{CT}$ is denoted by the thick red line. For this patient, the volume magnitude of $IGTV_{V,M,SBR}$ most accurately matched $IGTV_{CT}$ (-1.1%) followed by $IGTV_{15\%}$ (-10.1%). Surface separation was less than 2 mm for $IGTV_{15\%}$, $IGTV_{2.5}$, $IGTV_{15\%+BG}$, $IGTV_{SUVmean}$, and $IGTV_{V,M,SBR}$.

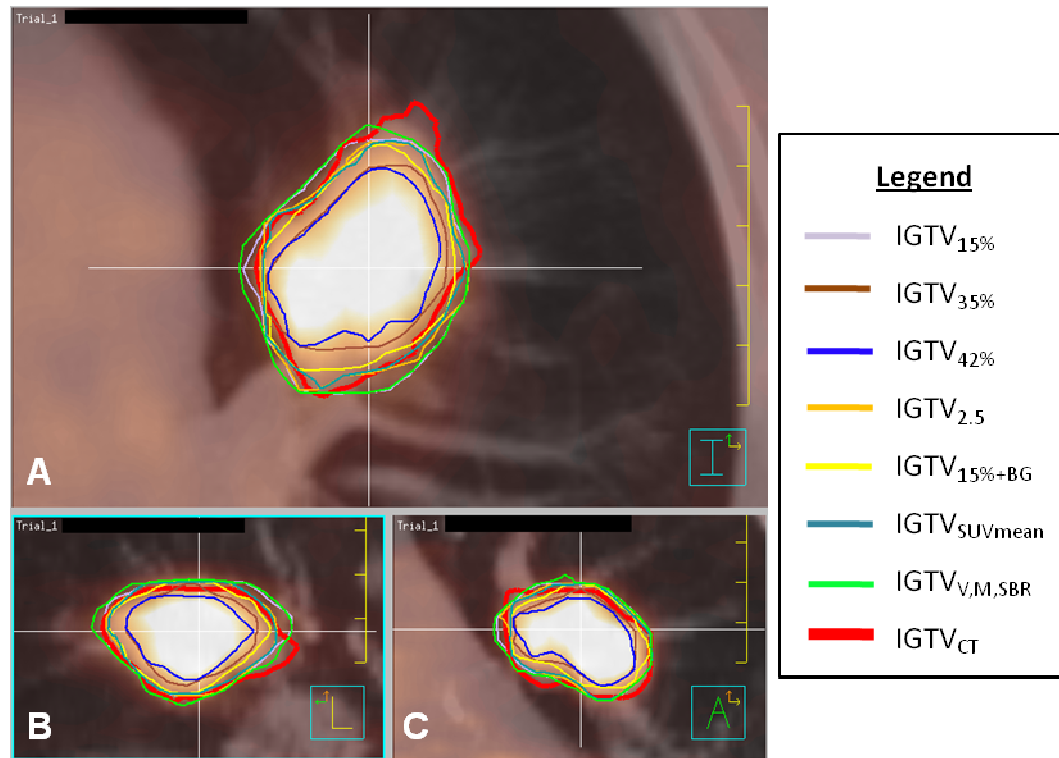


Figure 4.11: (A) Transverse, (B) sagittal, and (C) coronal PET/CT images of tumor 13 with internal gross tumor volume (IGTV) contours. PET is displayed with a “thermal” colormap. $IGTV_{CT}$, shown in red, was delineated on MIP_{cine} . Other IGTVs were delineated on PET using methods described in Table 4.1. The contour from the volume/motion/SBR model ($IGTV_{V,M,SBR}$) is shown in green.

Figure 4.12 provides another patient example, tumor 1. For this patient, the volume magnitude of $IGTV_{V,M,SBR}$ most accurately matched $IGTV_{CT}$ (-11.0%) followed by $IGTV_{2.5}$ (-12.2%). Surface separation was again less than 2 mm for $IGTV_{15\%}$, $IGTV_{2.5}$, $IGTV_{15\%+BG}$, $IGTV_{SUVmean}$, and $IGTV_{V,M,SBR}$. $IGTV_{V,M,SBR}$ had the lowest mean surface separation at 1 mm.

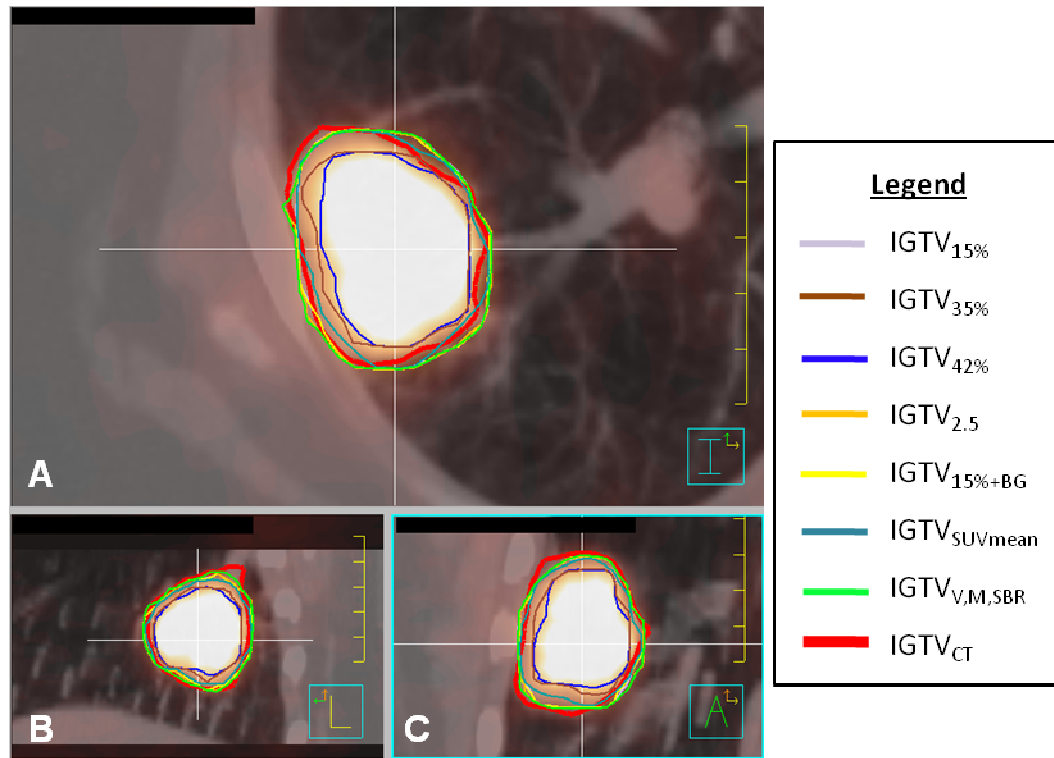


Figure 4.12: (A) Transverse, (B) sagittal, and (C) coronal PET/CT images of tumor 1 with internal gross tumor volume (IGTV) contours. PET is displayed with a “thermal” colormap. $IGTV_{CT}$, shown in red, was delineated on MIP_{cine} . Other IGTVs were delineated on PET using methods described in Table 4.1. The contour from the volume/motion/SBR model ($IGTV_{V,M,SBR}$) is shown in green.

Volume and surface separation analyses for all patients are summarized in Table 4.5 and illustrated in Figure 4.13 (volume analysis) and Figure 4.14 (surface separation analysis). Of the 7 segmentation methods, 6 underestimated mean volume compared to the motion-inclusive $IGTV_{CT}$. $IGTV_{15\%}$, $IGTV_{35\%}$, $IGTV_{42\%}$, and $IGTV_{2.5}$ were significantly smaller than $IGTV_{CT}$. $IGTV_{15\%+BG}$, $IGTV_{SUVmean}$, and $IGTV_{V,M,SBR}$ volumes were not significantly different from $IGTV_{CT}$. $IGTV_{V,M,SBR}$ produced the smallest difference with $IGTV_{CT}$ (-5.15%). Note that Figure 4.13 shows $IGTV_{2.5}$ slightly closer to $IGTV_{CT}$ than $IGTV_{15\%+BG}$, which was not

significantly different than IGTV_{CT}. Though this appears contradictory, IGTV_{CT} displayed on the graph is the average of all patients whereas the statistical comparison with IGTV_{2.5} used only the tumors that could be contoured (in this case, N=22). The same is true for IGTV_{15%} (N=18).

Mean surface separation (Figure 4.14) produced results consistent with the volume comparison. IGTV_{15%}|IGTV_{CT}, IGTV_{35%}|IGTV_{CT}, IGTV_{42%}|IGTV_{CT}, and IGTV_{2.5}|IGTV_{CT} produced surface separations significantly larger than IGTV_{V,M,SBR}|IGTV_{CT}. IGTV_{15%+BG}|IGTV_{CT} and IGTV_{SUVmean}|IGTV_{CT} were not significantly different from IGTV_{V,M,SBR}|IGTV_{CT}.

Table 4.5: Comparison of IGTV_{PET} with IGTV_{CT} for different segmentation methods

Notation	Volume ± SEM (cm ³)	<i>p</i>	(IGTV _{PET} - IGTV _{CT}) ± SEM	Percent Difference (%)	Mean Surface Separation (mm)	<i>p</i>
IGTV _{15%} *	10.93±2.71	0.01	+1.05±0.89	+10.7%	1.9±0.7	0.02
IGTV _{35%}	4.15±0.99	<0.01	-4.17±1.24	-50.1%	2.4±0.8	<0.01
IGTV _{42%}	3.12±3.93	<0.01	-5.21±1.38	-62.5%	3.0±1.1	<0.01
IGTV _{2.5} †	6.93±2.14	<0.01	-1.99±0.73	-22.3%	2.4±1.7	0.04
IGTV _{15%+BG}	6.36±1.67	0.14	-1.96±0.60	-23.6%	1.7±0.5	0.44
IGTV _{SUVmean}	7.02±1.67	0.33	-1.30±0.65	-15.7%	1.6±0.5	0.98
IGTV _{V,M,SBR}	7.89±1.76	0.39	-0.43±0.55	-5.15%	1.6±0.5	---
IGTV _{CT}	8.32±2.16	---	---	---	---	---

Statistically significant differences are in green print. Non-significance p-values are in red.

SEM = standard error of the mean

*N = 18. Statistics were calculated using paired values.

†N = 22. Statistics were calculated using paired values.

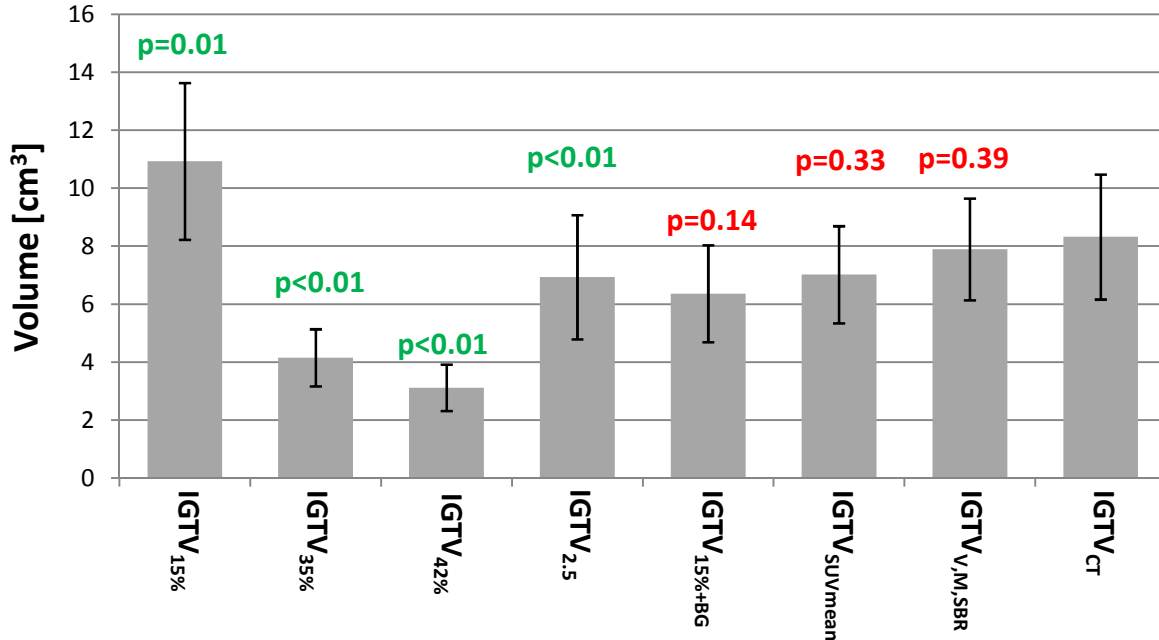


Figure 4.13: Volumes (in cubic centimeters) of IGTV_{PET} and IGTV_{CT}. Error bars represent standard error of the mean (N = 24 tumors for IGTV_{35%}, IGTV_{42%}, IGTV_{15%+BG}, IGTV_{SUVmean}, IGTV_{V,M,SBR}, N = 22 for IGTV_{2.5}, N = 18 for IGTV_{15%}). p-values are shown with each column (green = significant, red = non-significant).

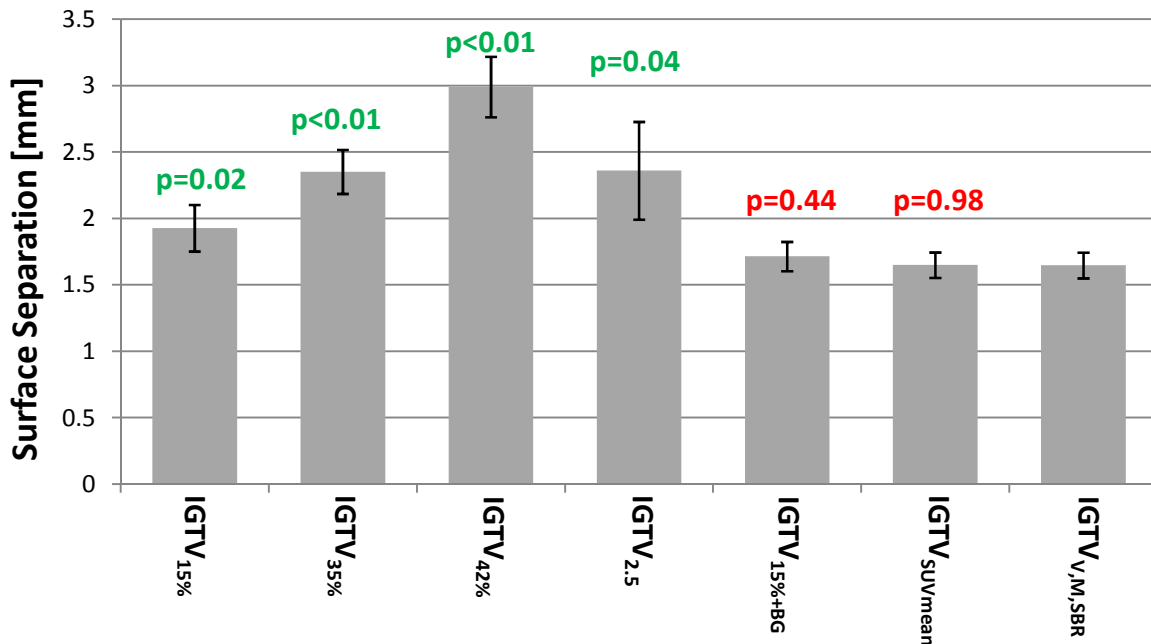


Figure 4.14: Surface separation (in millimeters) between IGTV_{PET} and IGTV_{CT}. Error bars represent standard error of the mean (N = 24 tumors for IGTV_{35%}, IGTV_{42%}, IGTV_{15%+BG}, IGTV_{SUVmean}, IGTV_{V,M,SBR}, N = 22 for IGTV_{2.5}, N = 18 for IGTV_{15%}). p-values are shown with each column (green = significant, red = non-significant).

4.5 Discussion

We successfully developed an expression for optimal AC threshold as a function of object volume, motion, and SBR. The volume/motion/SBR model, described in equation (12), fit the data well (adjusted $R^2 = 0.96$). By determining standardized regression coefficients, we found that SBR was the most influential variable in the model. In applying this model to 24 lung tumors, we found the volume/motion/SBR model generated an $IGTV_{PET}$ that accurately matched $IGTV_{CT}$ in volume magnitude (mean of 5.15% underestimation) and surface separation (mean of 1.6 mm). The volume/motion/SBR model produced the smallest volume differences and tied for the smallest surface separation compared with 6 other segmentation techniques.

This investigation is the most comprehensive examination of threshold-based segmentation of PET imaging of moving targets to date. It is the first to investigate the relationship between motion, size, and SBR for large ranges of SBR (5:1 to 50:1) and motion (0-30 mm), and the first to use the surface separation algorithm to determine optimal threshold volume. Several studies have explored elements of the current work, but not to the same depth. Yaremko *et al.* determined optimal thresholds for moving and static spheres in air, sizes ranging from 0.56 mL to 57.37 mL with 25 mm motion amplitude (Yaremko et al., 2005). Caldwell *et al.* investigated feasibility of using PET to delineate ITV by assessing PET images of 3 moving spheres (inner diameters = 1.3, 2.9, 6.6 cm) at 3 motion amplitudes (7, 16, 27 mm). The authors did not, however, determine optimal thresholds for each experimental condition but qualitatively found 15% of AC_{max} produced an adequate ITV (Caldwell et al., 2003). Black *et al.* examined the influence of size and, indirectly, SBR by developing a linear function of mean SUV, but motion was not included (Black et al., 2004).

There are several recent studies of moving phantoms that are similar to the model-development portion of this investigation. Park *et al.* examine the effects of target size, motion, and background activity on optimal thresholds in a phantom (Park et al., 2008). The authors use the NEMA IEC phantom (sphere diameters identical to the current work), sinusoidal motion with amplitudes of 0, 10, 20 mm (adjusted with an exponential shaping

parameter), and SBRs of 4.0, 8.3, and infinite (no background) to determine optimal thresholds for these varying conditions. After re-normalizing the threshold values in Figure 4.5 to AC_{max} for comparison, we found that the optimal thresholds in our study were generally lower than those determined by Park *et al.*

One significant difference between the two studies was the purpose of determining optimal thresholds. Park *et al.* intended to show the difficulty of obtaining the “true target volume” without gated (4-D) PET, which required comparing PET volumes to the known sphere volume, i.e. the *stationary* sphere. This explains the large difference in thresholds at 2 cm motion (90% in Park *et al.* vs. 18% in the current study for the smallest sphere with SBR = 8) (Park *et al.*, 2008). The goal of this chapter was to match PET threshold volumes with motion-inclusive IGTV often used in 4D-CT-based simulation, not the volume of the spheres themselves. Our values, however, were lower for the stationary spheres as well, especially for the smallest sphere (75% in Park *et al.* vs. 40% in the current study with SBR = 8). This difference can most likely be explained by the fact that Park *et al.* compared volume magnitudes and we compared surfaces. Volume was estimated by summing the number of voxels above the threshold and multiplying by voxel volume, which, for Park *et al.*, was $4.7 \times 4.7 \times 3.27$ mm. The width of one voxel was almost one half the inner diameter of the smallest sphere, which causes partial volume averaging and inaccurate calculation of the volume. The surface separation algorithm essentially measures between meshes interpolated from the voxel-based contours. Though not technically higher resolution, the interpolated meshes give us a finer estimation of the best-fit threshold volume.

Brambilla *et al.* investigated target volume delineation in the NEMA IEC thorax phantom as a function of several variables, including SBR, sphere diameter, injected activity, and emission scan duration (motion was not examined) (Brambilla *et al.*, 2008). Using multiple linear regression and standardized regression coefficients, the authors found that for sphere diameters less than 10 mm (additional microspheres of inner diameter 4.1, 4.7, 6.5, and 8.1 mm were added to the phantom for analysis), sphere diameter and SBR were significant predictors of optimal target threshold (as a percentage of AC_{max}). SBR dependence, however, could be neglected with little effect on optimal threshold to a first

approximation. For sphere diameters greater than 10 mm, again sphere diameter and SBR were significant predictors of optimal target threshold, but the opposite relationship between the two was observed: Sphere diameter was less significant and, to a first approximation, could be neglected. Injected activity and emission scan duration were not included in the current work because Brambilla *et al.* found both to be non-significant predictors of optimal threshold.

The multiple regression techniques used in the current study are similar to those used in Brambilla *et al.* In selecting their regression model, the authors determined from previous studies that optimal threshold normalized to AC_{max} is related to $1/SBR$ (Brambilla *et al.*, 2008). In the present study, we found a nearly linear relationship between SBR and optimal threshold normalized to background. These findings are consistent: An inverse relationship between SBR and threshold normalized to “signal” is equivalent to a linear relationship between SBR and threshold normalized to “background.” Brambilla *et al.* also used standardized regression coefficients in their study and found that SBR is the most influential variable for sphere diameters greater than 10 mm, which is consistent with the findings of the current study.

Okubo *et al.* used the NEMA IEC body phantom on a motion platform to examine optimal thresholds of moving spheres. In a stationary phantom at SBRs of 10:1, 15:1, and 20:1, the authors found 35% of AC_{max} was a reasonable threshold (Okubo *et al.*, 2008) after excluding the smaller spheres (inner diameter 10-17 mm) due to partial volume averaging. The 35% of AC_{max} threshold was applied to PET images of moving spheres at an SBR of 20:1. Motion was characterized as sinusoidal with a 4-sec period to 10, 20, and 30 mm amplitudes (peak-to-peak). The authors found that a 35% threshold overestimated actual sphere size in the sagittal plane and underestimated the actual sphere size in the axial plane. The extent in the sagittal plane, however, was smaller than the ideal IGTV. For comparison, we segmented the 28 mm inner diameter sphere, at 30 mm motion extent, and $SBR = 19.9$, at 35% of AC_{max} and compared with the stationary sphere (Figure 4.15). Axial extent was underestimated and sagittal extent was overestimated compared with the stationary sphere, consistent with the findings of Okubo *et al.* The motion envelope

(IGTV_{CT}), however, was underestimated in both axial and sagittal directions, suggesting that 35% of AC_{max} is too high a threshold to capture the entire extent of motion.

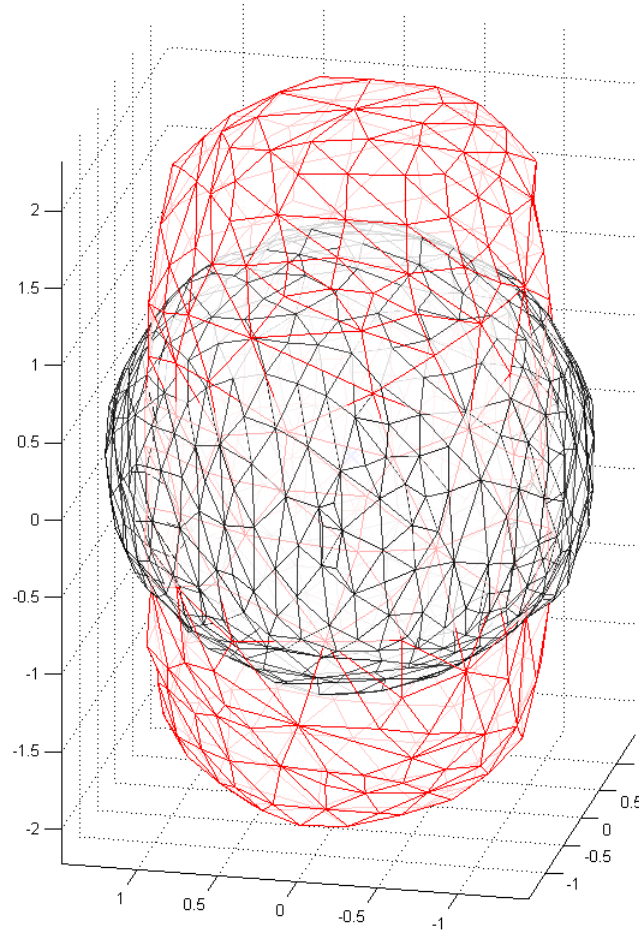


Figure 4.15: Reference volume for stationary sphere (black mesh, inner diameter = 28 mm) compared with 35% maximum activity concentration of same volume sphere at 30 mm motion extent and source-to-background = 19.9 (red mesh). Note that the 35% threshold underestimates the axial and overestimates the sagittal extent of the sphere, but underestimates the full motion envelope of the tumor. Reproduced with permission from Riegel *et al.* (Riegel *et al.*, 2010)

Several contouring methods, including those of Okubo *et al.* and Caldwell *et al.* discussed above, were applied to 24 lung tumors along with our volume/motion/SBR model. Our patient validation study is similar to a study by Nestle *et al.* which focused on a comparison of PET segmentation techniques for NSCLC (Nestle *et al.*, 2005) but there are several key differences. First, in the previous study, PET was acquired using a standalone

PET scanner with ^{137}Cs transmission scanning for attenuation correction. The current study utilizes an integrated PET/CT scanner with RACT attenuation correction. Second, the previous study contained 5 tumors able to be fully delineated on CT, whereas 24 tumors in our study were delineated on CT. Third, free-breathing CT was used to delineate the GTV in the previous study (which required additional coregistration because the PET and CT were not hardware-fused) and a margin was applied to account for breathing motion (1.5 mm lateral, 2 mm anterior-posterior, 3 mm superior-inferior). We explicitly determined the “motion envelope” of the tumor (IGTV) using 4D-CT.

The PET segmentation methods used in this study can be roughly split into two groups: The “first order” methods, which utilize a single threshold of activity concentration or SUV to form IGTV, and the “second order” methods, which incorporate additional variables into threshold determination. $\text{IGTV}_{15\%}$, $\text{IGTV}_{35\%}$, $\text{IGTV}_{42\%}$, and $\text{IGTV}_{2.5}$ fall into the first category, while $\text{IGTV}_{15\%+\text{BG}}$, $\text{IGTV}_{\text{SUVmean}}$, and $\text{IGTV}_{\text{V,M,SBR}}$ fall into the second. Our analysis suggests there are advantages to using more complex methods. $\text{IGTV}_{\text{V,M,SBR}}$, $\text{IGTV}_{15\%+\text{BG}}$, and $\text{IGTV}_{\text{SUVmean}}$ produced smaller surface separations than all first order methods and volume magnitude differences smaller than all but 1 first order method ($\text{IGTV}_{15\%}$) when compared with IGTV_{CT} . Though $\text{IGTV}_{15\%}$ performed relatively well in the volumetric analysis (the percent difference with CT was second smallest), 6 tumors (25%) were unable to be contoured because 15% of AC_{max} was below the background activity concentration in those patients. The paired t-test with the remaining pairs showed $\text{IGTV}_{15\%}$ being significantly larger than IGTV_{CT} and the inability to contour $\text{IGTV}_{15\%}$ in high background limits the applicability of such a method.

Of the second order techniques, $\text{IGTV}_{\text{V,M,SBR}}$ produced the smallest average volume difference with IGTV_{CT} (-5.15%) and tied $\text{IGTV}_{\text{SUVmean}}$ for the smallest average surface separation (1.6 mm). The differences, however, were not statistically significant. The second order methods had the smallest standard deviations in both volume difference and surface separation, suggesting they are more adaptable and more consistently delineate tumor over a sample of patients with varying characteristics. $\text{IGTV}_{\text{V,M,SBR}}$ demonstrated the

best adaptability by producing the lowest standard error of the mean in volume difference from CT.

The lack of statistical superiority of our segmentation technique (that includes motion) over the other second-order methods (that neglect motion) may indicate the importance of SBR relative to the other variables in the segmentation procedure in a clinical setting. Recall that we demonstrated SBR was the most influential variable in the model via the standardized regression coefficients. The fact that both $IGTV_{15\%+BG}$ and $IGTV_{SUV_{mean}}$ explicitly or implicitly account for SBR (the former by simply forming a threshold above a background measurement and the latter by using SUV_{mean} , a value normalized to injected activity divided by patient weight which is essentially “background” if one assumes the patient is uniform) and both perform nearly as well as a method that accounts for size, motion, and SBR seems to suggest that considering SBR in segmentation is essential and the other variables could be neglected. Our results, however, indicate that including size and motion in the segmentation technique can further increase the accuracy of the PET contour when compared with CT, though the improvement was not statistically significant.

The current manifestation of the volume/motion/SBR model represents a first approximation to modeling real moving tumors and there are several ways the model can be improved. The measurement of SBR, and particularly the measurement of background, is evidently critical for segmentation and the various factors that affect SBR should be further investigated. The selection of the background ROI for tumors bordering two tissues with different uptake such as lung and chest wall, for example, should be evaluated. Since the model is normalized to background, the selection of background ROI can substantially affect the resulting threshold. The size- and motion-dependent recovery coefficient to restore degraded SBR could also be further refined. Additionally, several assumptions were made in the development of the volume/motion/SBR model that should be explored further: First, the model was developed using one-dimensional sinusoidal motion, which is obviously not the case for many lung tumors (Boldea et al., 2008; Mageras et al., 2004). An asymmetric breathing pattern may be more appropriate (Lujan et al., 1999). Second, the model was developed with spherical objects; tumors with spiculations or substantial

asymmetry may not conform to the model. Third, we assumed that motion during the 4D-CT exam was essentially the same as motion during the PET exam. Motion patterns, including amplitude, frequency, and baseline position, can change over time (Nehmeh et al., 2004) leading to mismatching motion envelopes or misregistration. Fourth, the model was developed assuming homogeneous uptake, which is a reasonable assumption for smaller tumors, but not for larger tumors where heterogeneity, hypoxia, or necrosis often occur. The impact of AC heterogeneity on the volume/motion/SBR model should be evaluated.

Nevertheless, the volume/motion/SBR model has produced promising results and could be fine-tuned to produce more accurate contours. Though the model itself is somewhat complex, application is relatively simple. Only 4 measurements are required: Tumor volume, motion extent, $\overline{AC}_{80\%}$ of the tumor, and \overline{AC}_{BG} . First order techniques may be simpler, but the findings of Biehl *et al.* suggest that a single threshold is inappropriate for target delineation (Biehl et al., 2006) and, given the results of our validation, we must concur. Nestle *et al.* found that 40% threshold of AC_{max} underestimates GTV_{CT} with a population-based expansion to account for motion (Nestle et al., 2005). We had similar findings for both $IGTV_{42\%}$ and $IGTV_{35\%}$ when compared with a motion envelope explicitly determined on 4D-CT (as illustrated qualitatively in Figure 4.15 for $IGTV_{35\%}$ and quantitatively in Figure 4.13 and Figure 4.14). Sura *et al.* found high local failure rates when using PET to visually aid delineation of GTV (Sura et al., 2008), so caution must be exercised when using methods which substantially underestimate gross tumor.

Segmentation by threshold is a common method of target delineation with PET, but gradient methods have been investigated as well. Drever *et al.* compared threshold-based segmentation with Sobel edge-detection and a watershed technique (Drever et al., 2007). Sobel edge-detection operates by finding the maximum gradient values in the image and the watershed technique combines edge detection and region-growing (Drever et al., 2007). The authors found that both gradient techniques failed to accurately segment stationary targets in a phantom and that a threshold-based technique was most successful. Though gradient segmentation is beyond the scope of this work, exploration of gradient-based segmentation is important and should be pursued in future studies. For moving lung

tumors, however, we anticipate that a gradient-based approach will be problematic. Motion blur substantially decreases the AC gradient in the direction of motion, creating a situation where the edge of the tumor produces a high gradient in planes perpendicular to motion but a low gradient in planes parallel to motion. A single gradient threshold may be inadequate.

4.6 Conclusions

A segmentation model for moving lung lesions in PET was developed that incorporates tumor volume, motion, and SBR into determination of optimal activity concentration threshold (volume/motion/SBR model). The model, calibrated with an extensive series of phantom scans at varying size, motion, and SBR, was applied to 24 lung tumors to form IGTVs. These IGTVs, as well as IGTVs generated from 6 segmentation methods published in the literature, were compared with IGTV defined on cine CT. The volume/motion/SBR model produced IGTVs that correlated well with IGTV defined on cine CT. Segmentation techniques that used a single threshold produced significantly different IGTVs than the reference CT.

One significant objection to the clinical validation of the volume/motion/SBR model with respect to the over-arching purpose of this dissertation is the use of 4D-CT to determine motion extent. Recall that a primary motivation for incorporating PET into treatment planning in this work was to *avoid* using 4D-CT for complicated tumors. Measuring motion with 4D-CT defeats this purpose. We have shown in Chapter 2, however, that substantial motion information can be gleaned from MIP_{cine} and RAC_{cine} (image sets processed directly from cine CT), so it is probable that estimates of motion extent could be made with cine CT image sets.

The final chapter combines elements of Chapter 2 and Chapter 4 to contour more complex tumors.

Chapter 5 FEASIBILITY OF TARGET DELINEATION OF STAGE III NON-SMALL CELL LUNG CANCER WITH CINE PET/CT

5.1 Introduction

We have, thus far, focused on early stage lung cancer. We demonstrated the utility of contouring stage I NSCLC with MIP_{cine} and $RACT_{\text{cine}}$ in Chapter 2. We developed and validated a motion-inclusive PET contouring technique for relatively simple lesions in Chapter 4. In the final chapter, we assess the feasibility of combining these techniques to contour locally advanced NSCLC with “cine PET/CT” imaging.

Ultimately, application of this contouring technique to stage III NSCLC would impact the greatest number of patients because a combination of chemotherapy and radiation therapy is a standard of care for stage III NSCLC (along with surgical resection for stage IIIA). There are several differences between stage I and stage III NSCLC, including tumor size, shape, uptake heterogeneity in PET imaging, and nodal involvement, which make applying the cine PET/CT contouring technique non-trivial. These different aspects of stage III disease were not considered during development of the volume/motion/SBR segmentation model. The largest sphere volume, for example, was approximately 27 cm^3 , whereas many stage III GTVs can be greater than 100 cm^3 . Extrapolation from the model may be necessary. Such differences may cause problems when the model is applied to more complex cases.

5.2 Purpose

The purpose of this final study was to explore the feasibility of using PET together with MIP_{cine} and $RACT_{\text{cine}}$ for target delineation of stage III NSCLC by qualitatively assessing target volumes formed by the PET-based volume/motion/SBR model in stage III NSCLC.

5.3 Methods

Five patients were included in the feasibility study. Four patients had stage III NSCLC and each underwent 4D-CT and PET/CT as part of their treatment simulation. One patient had stage I NSCLC. The patient with stage I NSCLC was previously contoured in Chapter 2 as “patient 26” and was 1 of 3 patients with a tumor near the diaphragm who demonstrated substantial differences between contouring on cine CT image sets and 4D-CT. The patient did not receive a PET/CT at time of simulation but did receive a diagnostic PET/CT two weeks prior which was used for the feasibility study.

Table 5.1: Patients for cine PET/CT feasibility study

Patient	Stage	T	N	M	Volume (cm ³)	Motion (mm)	Corrected SBR	Tx
1	IA	1	0	0	10.7	17.8	23.2	SBRT
2	IIIB	3	3	0	215.0	8.1	25.0	IMRT
3	IIIB	4	0	0	5.8	2.9	17.7	SBRT
4	IIIA	3	1	0	20.0	8.9	25.4	PROTON
5	IIIB	4	2	0	86.3	1.0	64.7	IMRT

T = tumor grade based on tumor size

N = regional nodal status

M = distant metastasis

SBR = source-to-background ratio

Tx = Treatment modality

SBRT = stereotactic body radiation therapy

IMRT = intensity modulated radiation therapy

Tumor volume and motion were estimated using 4D-CT. If volumes could not be adequately defined using CT alone, volume estimates were made with rough threshold segmentation of PET. $\overline{AC}_{80\%}$ was measured as described in Chapter 4 and \overline{AC}_{BG} was measured by manually drawing an ROI in the lung and taking the mean activity concentration. Volume, motion, $\overline{AC}_{80\%}$, and \overline{AC}_{BG} served as input for the volume/motion/SBR model. Threshold calculations were performed on a simple spreadsheet (Excel, Microsoft, Inc., Redmond, WA), which included the recovery coefficient (Figure 5.1). $IGTV_{PET}$ formed from volume/motion/SBR thresholds were applied and

qualitatively compared with fused MIP_{cine} imaging to assess feasibility of using the model to contour in tandem with CT imaging. In particular, we looked for concordance of IGTV_{PET} with high contrast tumor/lung boundaries on CT.

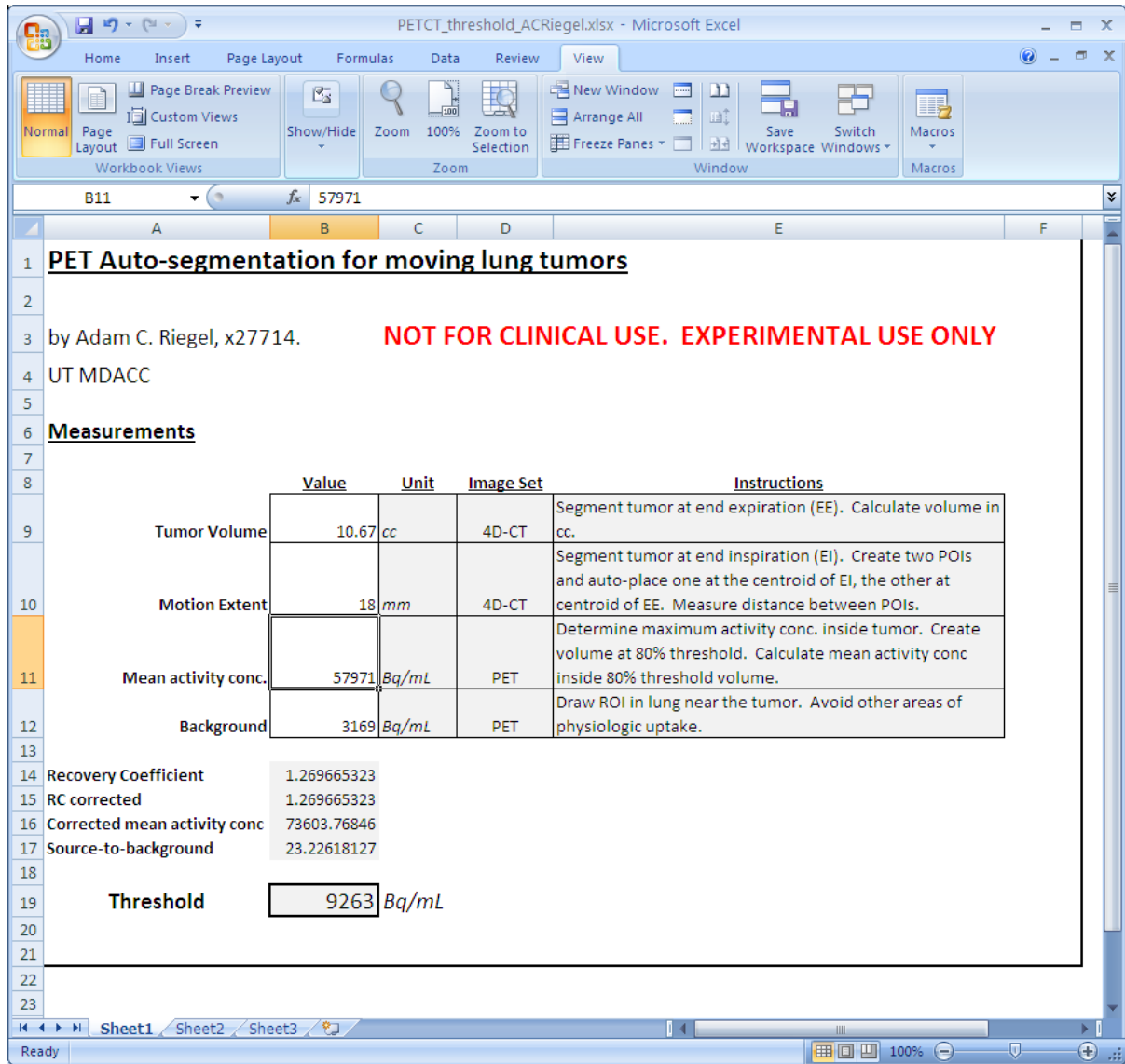


Figure 5.1: Microsoft Excel spreadsheet used to calculate thresholds using volume/motion/SBR model.

5.4 Results

5.4.1 Patient 1

This patient is the only stage I NSCLC patient and was contoured in Chapter 2 as patient #26. The PET data set, acquired two weeks prior to 4D-CT simulation, was manually registered to the tumor. The fused PET/CT data set, along with volume/motion/SBR model contour, is shown in Figure 5.2. Note the excellent agreement between anterior, posterior, and superior borders of the model-produced threshold and the MIP data set. The inferior border is well-described by the volume/motion/SBR model threshold. It is difficult, however, to say for certain whether or not the model is performing well because PET and CT were acquired on different days and there is no guarantee the patient was breathing similarly from day to day. The coincidence of the contour with the CT data set, however, is striking.

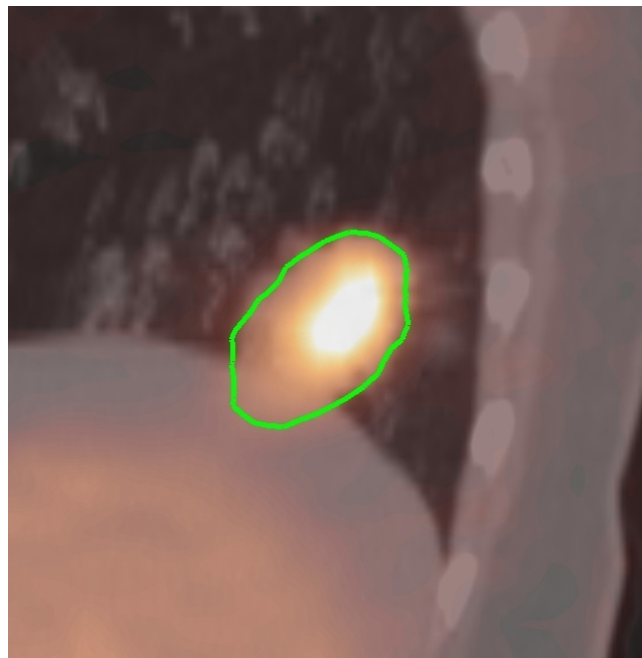


Figure 5.2: Sagittal PET/CT data set and volume/motion/SBR contour (green line) for patient 1. For this particular patient, PET was performed prior to 4D-CT simulation and was manually registered to the maximum intensity projection.

5.4.2 Patient 2

The primary in patient 2 was a large tumor adjacent to the chest wall and aorta. The tumor demonstrated significant AC heterogeneities, which contributed to an underestimated tumor boundary compared with CT (green contour, Figure 5.3). In this case, $\overline{AC}_{80\%}$ produced a mean value too high to segment the tumor. Manually drawing an ROI and taking the mean within the tumor produced a better result (blue contour), but the maximum motion extent is still underestimated.

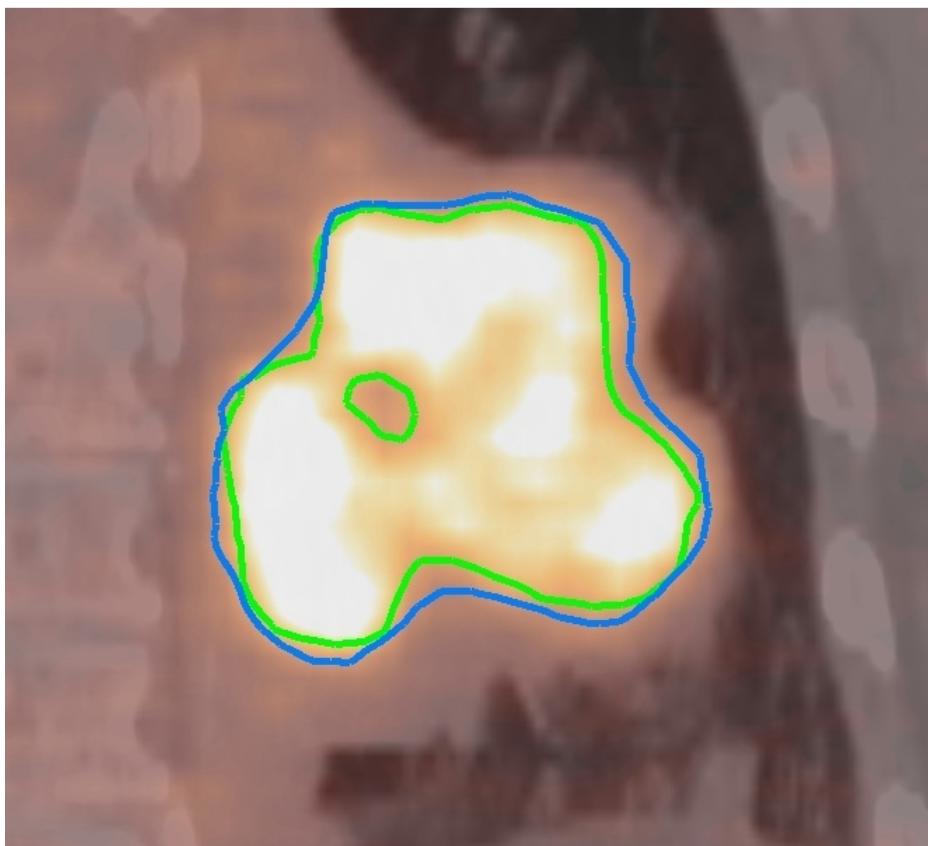


Figure 5.3: Coronal PET/CT data set and volume/motion/SBR contours for patient 2. Green line represents contour when $\overline{AC}_{80\%}$ is used in volume/motion/SBR model. Blue line represents contour when mean AC in manually drawn contour in middle of tumor is used in volume/motion/SBR model.

5.4.3 Patient 3

This patient had two lesions, one of which was invading the anterior chest wall and demonstrated 3 mm motion in the anterior-posterior direction. The result was a masking of the anterior extent of the tumor by the moving chest wall. We applied the model to this lesion and obtained the contour shown in Figure 5.4. Note that the posterior extent is slightly overestimated by the model, which may suggest overestimation in the anterior direction. There is, however, an asymmetric blur to the PET activity concentration gradient that can be explained by the asymmetric breathing pattern observed when scrolling through the 4D-CT phase imaging. The tumor spends more time in the posterior part of the motion envelope, resulting in sharper AC gradients on the posterior edge. For this patient, we obtained a better result using \overline{AC}_{BG} in the chest wall rather than the lung.

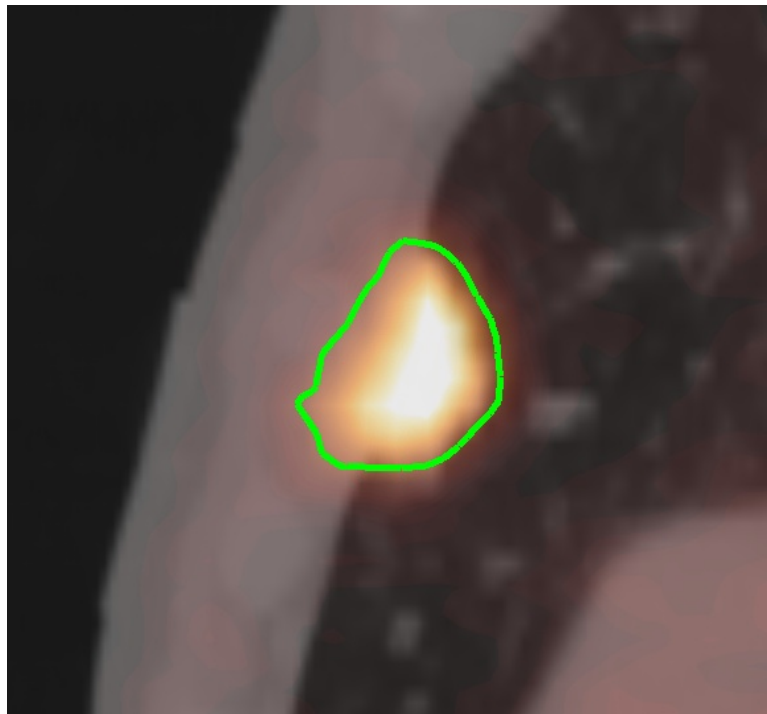


Figure 5.4: Sagittal PET/CT data set and volume/motion/SBR contour (green line) for patient 3.

5.4.4 Patient 4

The tumor in patient 4 demonstrates substantial mediastinal involvement. The resulting volume/motion/SBR threshold volume correlates well with the lateral border on CT and provides a good example of the ability of PET to distinguish between malignant tissue and atelectasis (which was noted in the nuclear medicine report of the PET/CT scan). PET/CT data set and threshold contours are shown in Figure 5.5.

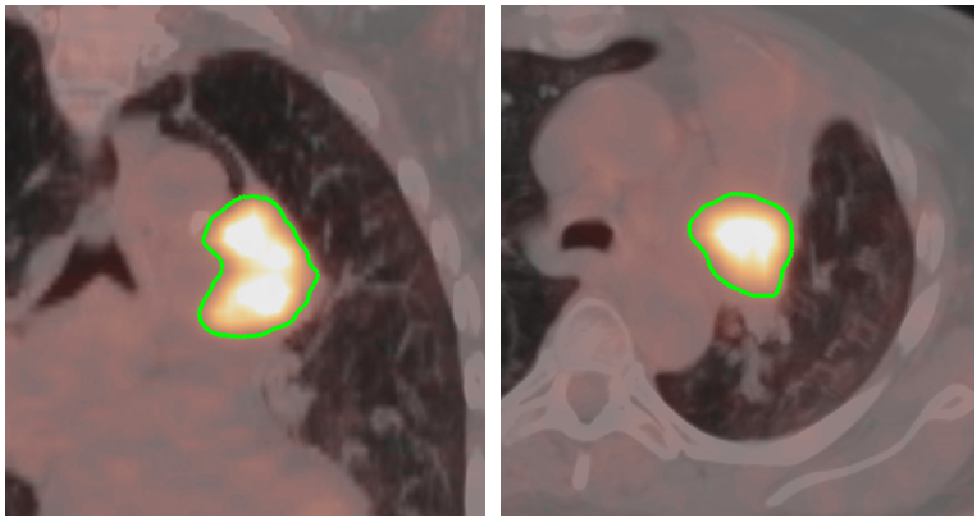


Figure 5.5: Coronal (left) and transverse (right) PET/CT data set and volume/motion/SBR contour (green line) for patient 4. Note the atelectasis present in the left upper lobe on the transverse CT image.

5.4.5 Patient 5

A similar case to patient 4, the tumor in patient 5 demonstrates substantial mediastinal involvement with more heterogeneity in the metabolic uptake of FDG. Again, the volume/motion/SBR model produces a volume that agrees well with the lateral border on CT. The superior-anterior border also matches well. PET/CT data set and threshold contours are shown in Figure 5.6.

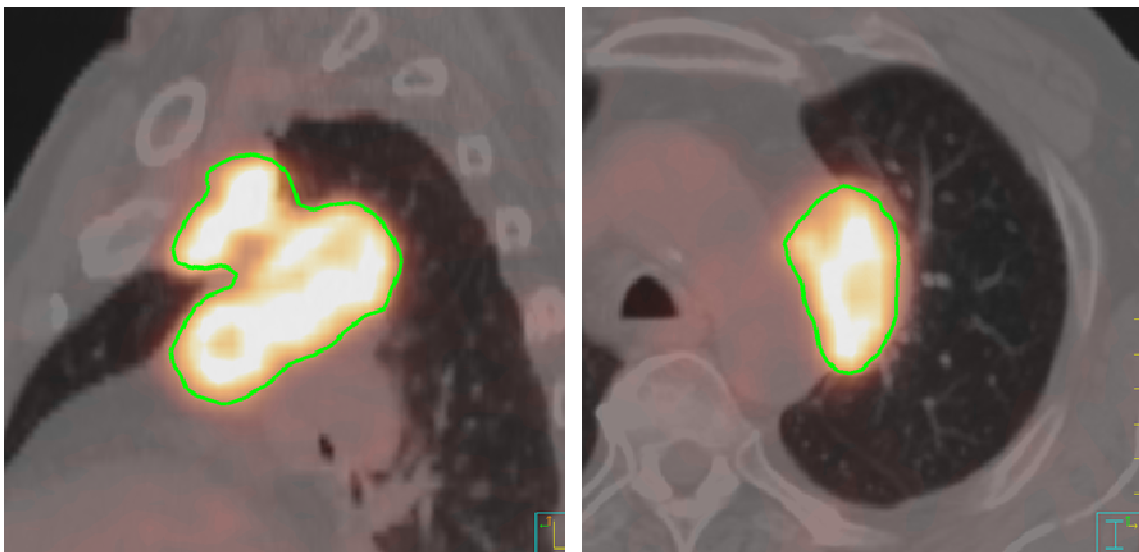


Figure 5.6: Sagittal (left) and transverse (right) PET/CT data set and volume/motion/SBR contour (green line) for patient 5.

5.5 Discussion

The current chapter explored the feasibility of applying the volume/motion/SBR model, which was developed using phantom scans and validated with reasonably simple tumors, to more complicated stage III NSCLC tumors. The results were mixed: The volume/motion/SBR model produced qualitatively good thresholds for some tumors (patients 1, 4, and 5) but not in others (patients 2 and 3). Obviously, further study will be needed to validate the use of the volume/motion/SBR method in this application.

There are several differences between stage I and stage III NSCLC that could be obstacles to full clinical use. First, stage III NSCLC tumors are larger and often display heterogeneous uptake on PET. As we saw in patient 2, this could cause problems for the volume/motion/SBR algorithm, which was not developed with heterogeneous tumors. Second, larger tumors are often adjacent to different kinds of tissue, which makes the selection of “background” for the segmentation algorithm tricky. The background ROI for patient 3 is a good example; placing the ROI in the chest wall gave a better threshold value than placing the ROI in the lung. Third, and probably most importantly, stage III NSCLC by definition has nodal involvement. Mediastinal and hilar lymph nodes have been shown to move substantially with respiratory motion (Donnelly et al., 2007; Pantarotto et al., 2009; Sher et al., 2007) and therefore could benefit from the volume/motion/SBR model, but we have not validated the model for this application. Furthermore, GTVs for stage III NSCLC often encompass large regions of the mediastinum if multiple nodes are present. A localized threshold-based segmentation technique such as the volume/motion/SBR model may be inappropriate for such an application.

5.6 Conclusions

Applying the volume/motion/SBR model to stage III NSCLC may be feasible, but further study into the appropriateness of the application and effectiveness of the model must be performed.

Chapter 6 DISCUSSION

6.1 Significance and Impact

Radiation therapy is becoming increasingly important for NSCLC. SBRT has been shown to be as effective as resection for inoperable stage I NSCLC (Chang et al., 2007; Timmerman et al., 2007). Retrospective studies have shown promising results for the use of SBRT in operable stage I NSCLC (Onishi et al., 2007) and investigations are currently underway to prospectively evaluate SBRT in operable stage I NSCLC (including a multicenter clinical trial led by M. D. Anderson.) Chemoradiation substantially benefits patients with stage III NSCLC (Govindan, 2003).

Considering the high dose gradients associated with IMRT and high biologically equivalent doses in SBRT, imaging is becoming ever more critical for target definition of lung tumors. One of the more recent technologies for imaging lung cancer is 4D-CT, which can capture the motion of the tumor during the patient's respiratory cycle. This information can be used to define a "motion envelope" of the tumor, what M. D. Anderson has dubbed the "internal gross tumor volume" or IGTV. Implementation of 4D-CT, however, can be costly and we have developed a simpler, more cost-effective alternative which provides significant motion information by generating MIP and RACT, image sets commonly used in target delineation, directly from cine CT. The purpose of this dissertation was to investigate the feasibility of using these image sets in conjunction with PET imaging to define IGTV on tumors of varying complexity.

We began in Chapter 2 by examining small, mobile stage I NSCLC tumors. We considered 2 groups of tumors: "High-contrast" tumors located in the middle of the lung parenchyma and "low-contrast" tumors adjacent to structures of equal or greater density. The average volume ratios for high-contrast and low-contrast tumors were 1.05 ± 0.14 and 0.97 ± 0.13 respectively. It was therefore shown that IGTVs contoured with MIP_{cine} and $RACT_{cine}$ are similar to or slightly larger than IGTVs contoured with 4D-CT (Riegel et al., 2009). In both phantom and patient studies, we found that MIP_{cine} captured the maximum

extent of motion more effectively than MIP_{4D-CT} . In Chapter 3, we turned to calculation of dose, another important aspect of treatment planning. Because $RACT_{cine}$ utilizes all the images in the cine CT image sequence, there is the possibility of weighting the average towards one phase of the breathing cycle. By calculating dose on RACT image sets formed by averaging 1, 1.5, and 2 breathing cycles, we showed that discrepancies between dose distributions calculated on $RACT_{cine}$ and $RACT_{4D-CT}$ were minimal (71 of 73 patients had all points within the PTV pass 2%/1mm γ index criteria). Including more breathing cycles reduced discrepancies even further (Riegel et al., 2008). Once dose calculation with $RACT_{cine}$ and stage I NSCLC contouring with MIP_{cine} and $RACT_{cine}$ were shown to be feasible alternatives to 4D-CT, we tackled tumor contouring using PET in the hopes that it would provide sufficient motion-inclusive targeting information to use with MIP_{cine} and $RACT_{cine}$ for more complex tumors, such as stage III NSCLC which have been shown to cause difficulties in MIP contouring (Muirhead et al., 2008). A threshold-based segmentation model was developed in Chapter 4 using an extensive series of phantom scans at varying sphere volume, motion amplitude, and SBR (Riegel et al., 2010). This model was applied to 24 lung tumors and performed better than 6 commonly-used segmentation methods at defining IGTV (-5.15% volume underestimation compared with CT), though the difference was only significant when compared with “first order” methods (simple thresholds of AC_{max} or SUV). Finally, we combined the cine CT contouring technique from Chapter 2 with the segmentation model from Chapter 4 to assess the feasibility of using structural and functional image modalities together to contour tumor on stage III NSCLC and a complex stage I NSCLC in Chapter 5. The results were mixed in that the volume/motion/SBR model was applicable and effective in some patients but not in all. With further research, the integration of cine CT and PET could prove to be a useful tool for physicists and radiation oncologists to accurately define motion-inclusive target volumes for lung tumors.

Though much work remains before clinical implementation, it is worthwhile to consider how a “cine PET/CT” simulation could be implemented in the clinic. The typical workflow for CT simulation begins at the scanner and ends at the treatment planning workstation. At M. D. Anderson, several pieces of hardware and software are utilized to

perform PET/CT and 4D-CT in the same imaging session: A PET/CT scanner, respiratory surrogate, respiratory surrogate computer and accompanying tracking software, a picture archiving and communication system (PACS) workstation (Advantage Window [AW], General Electric Medical Systems, Waukesha, WI), and 4D-CT sorting software (Advantage 4-D, General Electric Medical Systems, Waukesha, WI). At M. D. Anderson, 4D-CT images are generated on the AW workstation and transferred directly to treatment planning servers (they are not interpreted diagnostically). PET images are interpreted diagnostically by nuclear medicine physicians and, due to the inability to interactively view PET/CT imaging on our institution-wide PACS system, physicians utilize the AW as a “mini-PACS” to interpret PET images. They are then sent to the treatment planning servers for planning.

To perform PET/CT and cine CT, only two pieces of hardware are required: A PET/CT scanner and a personal computer networked to the scanner console. The only additional piece of software required is the relatively simple code to process cine CT image sets, which can be implemented on a standard Windows-based personal computer. If one is only concerned with using imaging for radiation therapy treatment planning (and not diagnostic value), 4D-CT and PET images can be sent directly to treatment planning servers, bypassing the need for a mini-PACS (though some digital storage back-up mechanism obviously must be in place). If the patient has not received a diagnostic PET/CT scan, however, it is beneficial to use the PET for staging purposes due to the ability to detect distant metastasis and the potential to change treatment intent from curative to palliative (Brink et al., 2004; Ciernik et al., 2003; Dizendorf et al., 2003; Mah et al., 2002). The different workflows are shown diagrammatically in Figure 6.1.

Three imaging exams should be performed in the treatment position (flat table top, wing-board to support arms above the head, etc.) in order to gain adequate information for treatment planning: (1) Cine CT of the thoracic cavity near the tumor using a long cine duration (approximately 2 average breathing cycles) to maximize respiratory waveform sampling for MIP_{cine} (Riegel et al., 2009) and minimize weighting for $RACT_{cine}$ (Riegel et al., 2008), (2) PET from base of skull to mid-thigh, and (3) free-breathing helical CT from the skull to the knees. Cine CT is acquired to produce MIP_{cine} and $RACT_{cine}$, which are used for

contouring purposes in high-contrast regions and motion measurement for the volume/motion/SBR model. $RAC_{T_{cine}}$ is additionally used for dose calculation and, together with the free-breathing helical CT, PET attenuation correction (Pan et al., 2006). PET is used to assess distant metastasis and is utilized for contouring with the volume/motion/SBR model (SBR is measured on the PET scan). Though helical CT of moving tumors does produce artifacts, it could be used to roughly estimate tumor volume for the volume/motion/SBR model input. The robustness of the model with respect to this input should be studied further.

One counterargument to cine PET/CT as a cost-saving measure compared with 4D-CT is the expense of the PET scan itself, both in the cost of the PET/CT scanner and FDG for each patient. Any costs cut by excluding 4D-CT, the argument goes, would be offset by costs of the PET scan. While it is true that the cost of PET scanning is by no means trivial, the utility of PET imaging versus 4D-CT imaging is greater. Currently, the use of 4D-CT is restricted to treatment planning and, in some limited cases, assessment of ventilation (Guerrero et al., 2006). PET, however, has significant utility in diagnosis in addition to applications in radiation oncology. It is feasible that the cooperative purchase of a PET/CT scanner shared by departments of radiology, nuclear medicine, and radiation oncology could defray the costs, making the cost of cine PET/CT to the radiation oncology department manageable. Diagnostic scans could increase patient throughput on the machine and help recoup costs.

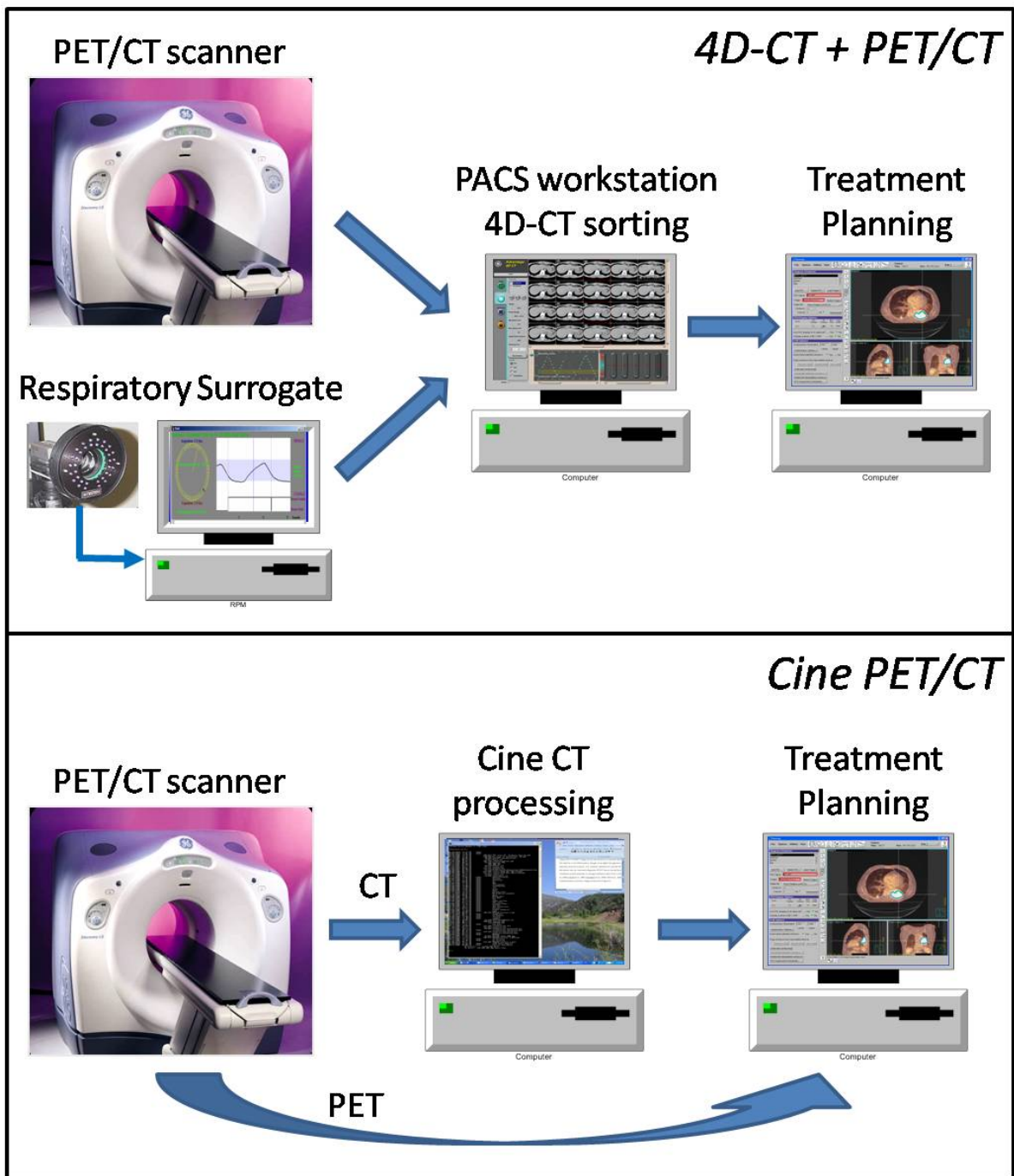


Figure 6.1: Workflow for (top) 4D-CT and PET acquisition versus (bottom) cine CT and PET acquisition.

6.2 Future Work

6.2.1 Weighted Maximum Intensity Projection (wMIP)

One of the findings of Chapter 2 was that some tumors near the diaphragm demonstrated substantial IGTV differences when contouring with MIP_{cine} and $RACT_{\text{cine}}$. This was mostly caused by the motion of the liver obscuring the inferior extent of the tumor's motion envelope. We developed an image processing technique called "weighted MIP" to solve this problem. Essentially, the weighted MIP or "wMIP" is formed by taking the MIP of a subset of images from the cine CT image sequence at the lung/liver junction. These images can be processed to include images of the tumor but exclude images of the liver, thereby discarding images that would overwrite inferior motion extent of the tumor.

Future work with wMIP will consist of contouring lesions that would otherwise be difficult to contour with cine CT alone and automating the image selection process. Automation could be achieved by using the liver itself as a respiratory surrogate. Since we are only concerned with the images at the lung/liver interface (which, of course, moves during the respiratory cycle), we could segment the lung at each slice in this region using a CT number threshold and derive a respiratory trace by measuring the changing lung area over the temporal cine CT sequence. Increasing and decreasing lung area would indicate end inspiration (no liver in slice) and expiration (liver in slice) respectively.

6.2.2 Improvement in PET Uptake Quantification

An interesting byproduct of Chapter 4 was the development of the recovery coefficient (RC) to correct for partial volume averaging and motion blur of the PET image. Though RCs based on object size have been explored, few publications of size- and motion-based RCs exist (Park et al., 2008).

Though the function used to model the RC fit the data well overall, there were regions of inaccuracy. Further research, including validation with gated 4D-PET/CT as the gold standard, is warranted.

In diagnostic PET for NSCLC, the commonly-accepted SUV for malignancy is 2.5 g/mL (Patz et al., 1993). This value, however, was determined by correlating SUV (without any size or motion correction) with histological results. For large, stationary tumors, SUV was likely not affected. For small, mobile tumors, however, SUV would have been underestimated. This may have caused dispersion in the data, clouding the relationship between SUV and histology. It may be worthwhile, therefore, to update the study using current technology. We intend to retrospectively recruit a large number of lung cancer patients who have received PET and 4D-CT, measure the motion and size via 4D-CT, apply a size- and motion-dependent RC to correct for partial volume averaging and motion blur, and compare corrected SUVs with histology to determine an appropriate benign/malignant SUV threshold.

6.2.3 Fine-Tuning the Volume/Motion/SBR Model

The volume/motion/SBR model is far from perfect for all the reasons listed in section 4.5. Ultimately, we hope to use this model in situations where CT cannot adequately define tumor boundaries, such as the stage III patients in the feasibility study described in Chapter 5. In order to do that, the model must be robust enough to work under a variety of conditions. Investigating asymmetry of the breathing cycle, irregular tumor geometry, the effect of heterogeneous uptake, and improvements to the recovery coefficient model are a few of several avenues to pursue to further refine the segmentation model for this purpose.

6.2.4 Nodal Involvement in Stage III Non-Small Cell Lung Cancer

Perhaps the biggest difference between stage I and stage III NSCLC is the presence of regional lymph node metastasis. As briefly discussed in Chapter 5, it is worthwhile to consider the appropriateness of using a localized threshold-based segmentation technique for contouring mobile hilar and mediastinal lymph nodes. Regardless of whether or not the volume/motion/SBR model is used, the efficacy of PET in contouring nodal involvement in conjunction with MIP_{cine} and $RACT_{\text{cine}}$ should be evaluated by comparing with 4D-CT. We

should, in essence, repeat the experimental setup detailed in Chapter 2, this time comparing IGTVs delineated on $MIP_{\text{cine}} + RACT_{\text{cine}} + PET$ versus IGTVs delineated on $MIP_{4D-CT} + 4D-CT \text{ phases} + PET$. In addition to intraobserver variation, interobserver variation should be assessed.

Chapter 7 CONCLUSIONS AND RECOMMENDATIONS

The results of this work are promising. We have shown that $RACT_{\text{cine}}$ is a viable alternative to $RACT_{4\text{D-CT}}$ for the purposes of dose calculation and can be implemented reasonably. We have shown MIP_{cine} and $RACT_{\text{cine}}$ can be used to contour moving stage I NSCLC located in the lung parenchyma and we have presented evidence that PET (via the segmentation model) can be used in conjunction with MIP and RACT to contour smaller tumors adjacent to structures of equal or greater density. Though more research is required to assess the efficacy of PET in stage III disease, the work presented here provides a solid foundation for future investigations.

The cine PET/CT workflow in Figure 6.1 reduces the complexity of the motion-inclusive simulation process and could substantially reduce the costs of motion-inclusive imaging for radiation therapy simulation. Though more research is required to fine-tune the technique, we have 4 recommendations:

- If 4D-CT is not available, we recommend acquiring cine CT and free-breathing helical CT for treatment simulation of lung cancer patients, including the use of MIP_{cine} and $RACT_{\text{cine}}$ for contouring and $RACT_{\text{cine}}$ for dose calculation. Any motion information is better than none.
- If 4D-CT is available, we recommend that MIP_{cine} be used with phase imaging because it more accurately captures the maximum motion extent of the tumor than $MIP_{4\text{D-CT}}$. Dose calculation with either $RACT_{4\text{D-CT}}$ or $RACT_{\text{cine}}$ is recommended.
- If PET/CT is available, we recommend that IGTV be contoured primarily on CT (cine CT or 4D-CT) using volume/motion/SBR model as a supplemental guide when contouring small, mobile tumors with relatively homogenous uptake on PET. Further research is required to recommend use in larger, more complex lesions.
- If cine CT is acquired, we recommend that cine duration be set as long as possible (2 average breathing cycles is a good target) to maximize sampling of the respiratory waveform and minimize density weighting effects.

Chapter 8 APPENDIX

A detailed description of the surface separation algorithm is provided here. The code is basically split into two main parts: First, the “reference” surface mesh is sampled by calculating the intersection of equally-spaced vectors projected from the center of the reference ROI and the triangular mesh surface; second, the shortest distance between the sampling point on the reference mesh and the test mesh surface is calculated.

8.1 Sampling the Reference Surface

The centroid (the center of mass assuming unit density) of the reference ROI is determined by averaging the pixel coordinates inside the ROI. Vertices of the reference mesh are transformed such that the reference ROI centroid is the origin of the coordinate system. Rays are projected from the origin (the centroid) at regular azimuthal and altitudinal angles. For our study, we used an angular interval of 5°.

The mesh surface is made of hundreds or thousands of adjacent triangles which connect the vertices of the mesh. Each triangle defines a plane. Our task is twofold: We must calculate the intersection of the sampling vector with the plane and also determine whether or not the intersection is inside the triangle defined with the mesh vertices. Furthermore, we must iterate this process for all triangles, for every sampling ray.

Mathematically, if we consider r_1 , r_2 , and r_3 to be vertices of a triangle on the reference surface mesh, the plane that contains the triangle is defined by equation (14):

$$P(u, v) = \vec{r}_1 + (\vec{r}_2 - \vec{r}_1)u + (\vec{r}_3 - \vec{r}_1)v \quad (14)$$

where u and v are barycentric coordinates of a point in the plane of the triangle (Moller et al., 1997). The equation for the ray originating from the reference centroid (denoted by \mathcal{O} , the origin of the coordinate system) is:

$$R(t) = \vec{O} + (\vec{\ell} - \vec{O})t \quad (15)$$

where $\vec{\ell}$ is the directional ray vector and t is the length of the ray (in this case, a parametric variable).

According to Moller and Trumbore (Moller et al., 1997), we can simultaneously determine the intersection of the ray with the plane and whether or not the intersection is inside the triangle by setting equation (14) equal to equation (15) and solving for the vector $[t \ u \ v]$.

$$\vec{O} + (\vec{\ell} - \vec{O})t = \vec{r}_1 + (\vec{r}_2 - \vec{r}_1)u + (\vec{r}_3 - \vec{r}_1)v \quad (16)$$

By rearranging and putting this equation into matrix form,

$$\begin{bmatrix} \mathcal{O}_x - r_{1,x} \\ \mathcal{O}_y - r_{1,y} \\ \mathcal{O}_z - r_{1,z} \end{bmatrix} = \begin{bmatrix} \mathcal{O}_x - \ell_x & r_{2,x} - r_{1,x} & r_{3,x} - r_{1,x} \\ \mathcal{O}_y - \ell_y & r_{2,y} - r_{1,y} & r_{3,y} - r_{1,y} \\ \mathcal{O}_z - \ell_z & r_{2,z} - r_{1,z} & r_{3,z} - r_{1,z} \end{bmatrix} \begin{bmatrix} t \\ u \\ v \end{bmatrix} \quad (17)$$

we can take the inverse of the middle matrix to determine $[t \ u \ v]$.

$$\begin{bmatrix} t \\ u \\ v \end{bmatrix} = \begin{bmatrix} \mathcal{O}_x - \ell_x & r_{2,x} - r_{1,x} & r_{3,x} - r_{1,x} \\ \mathcal{O}_y - \ell_y & r_{2,y} - r_{1,y} & r_{3,y} - r_{1,y} \\ \mathcal{O}_z - \ell_z & r_{2,z} - r_{1,z} & r_{3,z} - r_{1,z} \end{bmatrix}^{-1} \begin{bmatrix} \mathcal{O}_x - r_{1,x} \\ \mathcal{O}_y - r_{1,y} \\ \mathcal{O}_z - r_{1,z} \end{bmatrix} \quad (18)$$

Because u and v represent barycentric coordinates, they are relative to the vertices of the triangle. Therefore, if the solution of u and v satisfies the following conditions,

$$\begin{aligned} 0 &\leq u \leq 1 \\ 0 &\leq v \leq 1 \\ u + v &\leq 1 \end{aligned}$$

then the intersection of the ray and the plane lies within the triangle defined by r_1 , r_2 , and r_3 , and the coordinates of the intersection can be found by plugging the solution for t into equation (15). The intersection coordinates are deposited into a new matrix of points that “sample” the reference mesh surface. If the point lies outside the triangle, it is discarded. This is repeated for all triangles and all sampling rays.

For typical convex shapes, the number of sampling points will equal the number of sampling rays. There are clinical scenarios, however, when the tumor contains spiculations and will cause multiple intersections of the ray with the mesh surface. The algorithm is designed to include these multiple intersections in the surface separation calculation.

8.2 Determination of Shortest Distance between Reference and Test Surfaces

First, the test surface mesh is transformed to the reference ROI centroid coordinate system. The next step is to measure the separation between the reference surface and the test surface by calculating the shortest distance from each sampling point to the test surface. There are two outcomes: Either the shortest distance is on a face of the surface mesh (inside the triangle formed by the vertices) or it is on the edge of the surface mesh (one of the lines connecting the vertices). The algorithm is designed to consider each scenario separately and determine which distance is smaller.

8.2.1 Faces

First, to measure the distance from the sampling point to each plane formed by the surface triangles, we must calculate the projection of the sampling point q on every plane. To do so, we must establish orthogonal basis vectors within each plane using the Gram-Schmidt process (Lay, 1997). To summarize, if p_1 , p_2 , and p_3 are vertices of a triangle on the test surface mesh and q is the point to be projected onto that plane, consider the vectors $\vec{x}_1 = \vec{p}_2 - \vec{p}_1$, $\vec{x}_2 = \vec{p}_3 - \vec{p}_1$, and $\vec{y} = \vec{q} - \vec{p}_1$. Orthogonal basis vectors are formed using equations (19) and (20):

$$\vec{v}_1 = \vec{x}_1 \quad (19)$$

$$\vec{v}_2 = \vec{x}_2 - \frac{\vec{x}_2 \cdot \vec{v}_1}{\vec{v}_1 \cdot \vec{v}_1} \vec{v}_1 \quad (20)$$

The projection of the sampling point onto a p -dimensional space is defined by Lay (Lay, 1997):

$$\hat{y} = \frac{\vec{y} \cdot \vec{u}_1}{\vec{u}_1 \cdot \vec{u}_1} \vec{u}_1 + \dots + \frac{\vec{y} \cdot \vec{u}_p}{\vec{u}_p \cdot \vec{u}_p} \vec{u}_p \quad (21)$$

Where $\{u_1, \dots, u_p\}$ is an orthogonal basis of the plane. In our case, the orthogonal basis is provided by the Gram-Schmidt process, and the projection is demonstrated in equation (22):

$$\hat{y} = \frac{\vec{y} \cdot \vec{v}_1}{\vec{v}_1 \cdot \vec{v}_1} \vec{v}_1 + \frac{\vec{y} \cdot \vec{v}_2}{\vec{v}_2 \cdot \vec{v}_2} \vec{v}_2 + \vec{p}_1 \quad (22)$$

We now have two points that define a line normal to the plane: q , the sampling point on the reference mesh, and \hat{y} , the projection of q on the plane. Using the method described in the previous section, we determine whether or not this line falls inside the vertices of the plane-defining triangle p_1 , p_2 , and p_3 . If \hat{y} lies within the triangle, the distance $\|\hat{y} - q\|$ is placed in a matrix where “candidate” shortest distances are stored. If it lies outside the triangle, it is discarded.

8.2.2 Edges

The sampling point is then projected on each edge of the triangle using equation (21) with only 1 basis vector for each edge. The edges are defined thusly: $\vec{v}_1 = \vec{p}_2 - \vec{p}_1$, $\vec{v}_2 = \vec{p}_3 - \vec{p}_1$, $\vec{v}_3 = \vec{p}_3 - \vec{p}_2$. The vectors to be projected are defined as such: $\vec{y}_1 = \vec{q} - \vec{p}_1$, $\vec{y}_2 = \vec{q} - \vec{p}_2$). The projections are therefore:

$$\begin{aligned}\widehat{y}_1 &= \frac{\vec{y}_1 \cdot \vec{v}_1}{\vec{v}_1 \cdot \vec{v}_1} \vec{v}_1 + \vec{p}_1 \\ \widehat{y}_2 &= \frac{\vec{y}_1 \cdot \vec{v}_2}{\vec{v}_2 \cdot \vec{v}_2} \vec{v}_2 + \vec{p}_1 \\ \widehat{y}_3 &= \frac{\vec{y}_2 \cdot \vec{v}_3}{\vec{v}_3 \cdot \vec{v}_3} \vec{v}_3 + \vec{p}_2\end{aligned}\tag{ 23 }$$

The distances from the sampling point q to each projection is stored in the “candidate” matrix, along with the distance from q to the triangle face (if the normal lies inside the triangle). This represents one iteration of the process. The process is repeated for all triangles and the shortest distance of all the triangles is recorded as the surface separation for that particular sampling point. The process is iterated over all sampling points. A visualization of the surface separation algorithm is shown in Figure 8.1.

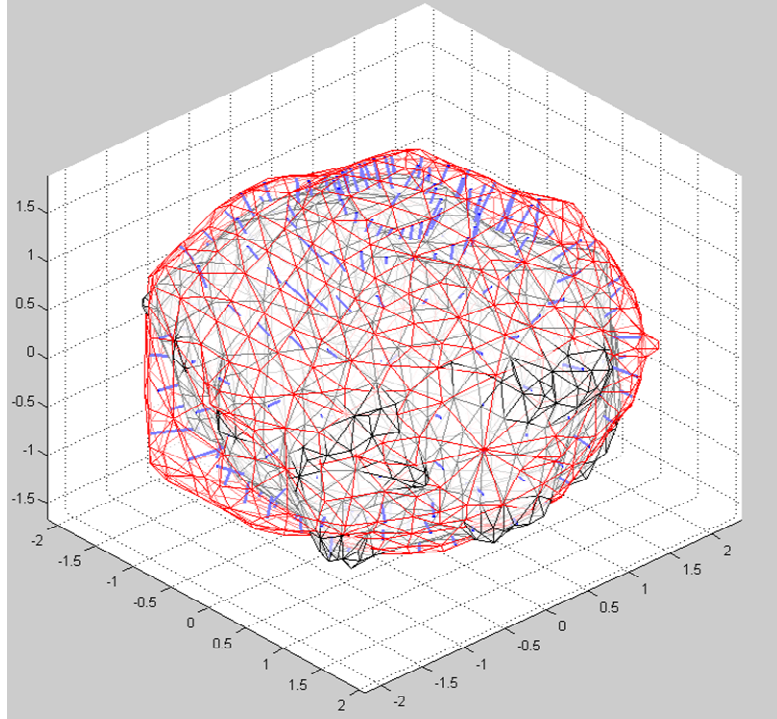


Figure 8.1: End result of the surface separation algorithm. Black mesh is "reference" mesh. Red mesh is "test" mesh. Blue lines represent shortest distances from the sampling points on the reference mesh to the test mesh surface.

REFERENCES

- American Cancer Society, "Cancer Facts & Figures 2009," Atlanta: American Cancer Society; 2009.
- Admiraal MA, Schuring D, Hurkmans CW. "Dose calculations accounting for breathing motion in stereotactic lung radiotherapy based on 4D-CT and the internal target volume." *Radiother Oncol.* (2008) **86**(1), 55-60.
- Ashamalla H, Rafla S, Parikh K, Mokhtar B, Goswami G, Kambam S, Abdel-Dayem H, Guirguis A, Ross P, Evola A. "The contribution of integrated PET/CT to the evolving definition of treatment volumes in radiation treatment planning in lung cancer." *Int J Radiat Oncol Biol Phys.* (2005) **63**(4), 1016-1023.
- Bacharach SL. "PET/CT attenuation correction: breathing lessons." *J Nucl Med.* (2007) **48**(5), 677-679.
- Bartko JJ. "Measurement and reliability: statistical thinking considerations." *Schizophr Bull.* (1991) **17**(3), 483-489.
- Beutel J. *Handbook of medical imaging. Vol 2: Medical Image Processing and Analysis.* Bellingham, Wash.: SPIE Press; 2000.
- Biehl KJ, Kong FM, Dehdashti F, Jin JY, Mutic S, El Naqa I, Siegel BA, Bradley JD. "18F-FDG PET definition of gross tumor volume for radiotherapy of non-small cell lung cancer: is a single standardized uptake value threshold approach appropriate?" *J Nucl Med.* (2006) **47**(11), 1808-1812.

- Black QC, Grills IS, Kestin LL, Wong CY, Wong JW, Martinez AA, Yan D. "Defining a radiotherapy target with positron emission tomography." *Int J Radiat Oncol Biol Phys.* (2004) **60**(4), 1272-1282.
- Boldea V, Sharp GC, Jiang SB, Sarrut D. "4D-CT lung motion estimation with deformable registration: quantification of motion nonlinearity and hysteresis." *Med Phys.* (2008) **35**(3), 1008-1018.
- Boucher L, Rodrigue S, Lecomte R, Benard F. "Respiratory gating for 3-dimensional PET of the thorax: feasibility and initial results." *J Nucl Med.* (2004) **45**(2), 214-219.
- Bradley J, Thorstad WL, Mutic S, Miller TR, Dehdashti F, Siegel BA, Bosch W, Bertrand RJ. "Impact of FDG-PET on radiation therapy volume delineation in non-small-cell lung cancer." *Int J Radiat Oncol Biol Phys.* (2004) **59**(1), 78-86.
- Bradley JD, Nofal AN, El Naqa IM, Lu W, Liu J, Hubenschmidt J, Low DA, Drzymala RE, Khullar D. "Comparison of helical, maximum intensity projection (MIP), and averaged intensity (AI) 4D CT imaging for stereotactic body radiation therapy (SBRT) planning in lung cancer." *Radiother Oncol.* (2006) **81**(3), 264-268.
- Brambilla M, Matheoud R, Secco C, Loi G, Krengli M, Inglese E. "Threshold segmentation for PET target volume delineation in radiation treatment planning: the role of target-to-background ratio and target size." *Med Phys.* (2008) **35**(4), 1207-1213.
- Brandner ED, Wu A, Chen H, Heron D, Kalnicki S, Komanduri K, Gerszten K, Burton S, Ahmed I, Shou Z. "Abdominal organ motion measured using 4D CT." *Int J Radiat Oncol Biol Phys.* (2006) **65**(2), 554-560.

Brink I, Schumacher T, Mix M, Ruhland S, Stoelben E, Digel W, Henke M, Ghanem N, Moser E, Nitzsche EU. "Impact of [18F]FDG-PET on the primary staging of small-cell lung cancer." *Eur J Nucl Med Mol Imaging*. (2004) **31**(12), 1614-1620.

Brooks RA, Di Chiro G. "Theory of image reconstruction in computed tomography." *Radiology*. (1975) **117**(3 Pt 1), 561-572.

Bushberg JT. *The essential physics of medical imaging*. 2nd ed. Philadelphia: Lippincott Williams & Wilkins; 2002.

Cai J, Read PW, Baisden JM, Lerner JM, Benedict SH, Sheng K. "Estimation of error in maximal intensity projection-based internal target volume of lung tumors: a simulation and comparison study using dynamic magnetic resonance imaging." *Int J Radiat Oncol Biol Phys*. (2007) **69**(3), 895-902.

Caldwell CB, Mah K, Ung YC, Danjoux CE, Balogh JM, Ganguli SN, Ehrlich LE. "Observer variation in contouring gross tumor volume in patients with poorly defined non-small-cell lung tumors on CT: the impact of 18FDG-hybrid PET fusion." *Int J Radiat Oncol Biol Phys*. (2001) **51**(4), 923-931.

Caldwell CB, Mah K, Skinner M, Danjoux CE. "Can PET provide the 3D extent of tumor motion for individualized internal target volumes? A phantom study of the limitations of CT and the promise of PET." *Int J Radiat Oncol Biol Phys*. (2003) **55**(5), 1381-1393.

Chang JY, Roth JA. "Stereotactic body radiation therapy for stage I non-small cell lung cancer." *Thorac Surg Clin*. (2007) **17**(2), 251-259.

- Chen GT, Kung JH, Beaudette KP. "Artifacts in computed tomography scanning of moving objects." *Semin Radiat Oncol.* (2004) **14**(1), 19-26.
- Chi PC, Mawlawi O, Nehmeh SA, Erdi YE, Balter PA, Luo D, Mohan R, Pan T. "Design of respiration averaged CT for attenuation correction of the PET data from PET/CT." *Med Phys.* (2007) **34**(6), 2039-2047.
- Childress NL, Rosen, II. "The design and testing of novel clinical parameters for dose comparison." *Int J Radiat Oncol Biol Phys.* (2003) **56**(5), 1464-1479.
- Childress NL, White RA, Bloch C, Salehpour M, Dong L, Rosen, II. "Retrospective analysis of 2D patient-specific IMRT verifications." *Med Phys.* (2005) **32**(4), 838-850.
- Chu JC, Ni B, Kriz R, Amod Saxena V. "Applications of simulator computed tomography number for photon dose calculations during radiotherapy treatment planning." *Radiother Oncol.* (2000) **55**(1), 65-73.
- Ciernik IF, Dizendorf E, Baumert BG, Reiner B, Burger C, Davis JB, Lutolf UM, Steinert HC, Von Schulthess GK. "Radiation treatment planning with an integrated positron emission and computer tomography (PET/CT): a feasibility study." *Int J Radiat Oncol Biol Phys.* (2003) **57**(3), 853-863.
- Cover KS, Lagerwaard FJ, Senan S. "Color intensity projections: a rapid approach for evaluating four-dimensional CT scans in treatment planning." *Int J Radiat Oncol Biol Phys.* (2006) **64**(3), 954-961.
- Daisne JF, Sibomana M, Bol A, Doumont T, Lonneux M, Gregoire V. "Tri-dimensional automatic segmentation of PET volumes based on measured source-to-background

- ratios: influence of reconstruction algorithms." *Radiother Oncol.* (2003) **69**(3), 247-250.
- Davis JB, Reiner B, Huser M, Burger C, Szekely G, Ciernik IF. "Assessment of 18F PET signals for automatic target volume definition in radiotherapy treatment planning." *Radiother Oncol.* (2006) **80**(1), 43-50.
- Davis JN, Stagg D. "Interrelationships of the volume and time components of individual breaths in resting man." *J Physiol.* (1975) **245**(2), 481-498.
- Depuydt T, Van Esch A, Huyskens DP. "A quantitative evaluation of IMRT dose distributions: refinement and clinical assessment of the gamma evaluation." *Radiother Oncol.* (2002) **62**(3), 309-319.
- Dice LR. "Measures of the amount of ecologic association between species." *Ecology.* (1945) **26**297-302.
- Dizendorf EV, Baumert BG, von Schulthess GK, Lutolf UM, Steinert HC. "Impact of whole-body 18F-FDG PET on staging and managing patients for radiation therapy." *J Nucl Med.* (2003) **44**(1), 24-29.
- Donnelly ED, Parikh PJ, Lu W, Zhao T, Lechleiter K, Nystrom M, Hubenschmidt JP, Low DA, Bradley JD. "Assessment of intrafraction mediastinal and hilar lymph node movement and comparison to lung tumor motion using four-dimensional CT." *Int J Radiat Oncol Biol Phys.* (2007) **69**(2), 580-588.
- Dosoretz DE, Katin MJ, Blitzer PH, Rubenstein JH, Salenius S, Rashid M, Dosani RA, Mestas G, Siegel AD, Chadha TT, et al. "Radiation therapy in the management of medically

- inoperable carcinoma of the lung: results and implications for future treatment strategies." *Int J Radiat Oncol Biol Phys.* (1992) **24**(1), 3-9.
- Drever LA, Roa W, McEwan A, Robinson D. "Comparison of three image segmentation techniques for target volume delineation in positron emission tomography." *J Appl Clin Med Phys.* (2007) **8**(2), 93-109.
- Erdi YE, Mawlawi O, Larson SM, Imbriaco M, Yeung H, Finn R, Humm JL. "Segmentation of lung lesion volume by adaptive positron emission tomography image thresholding." *Cancer.* (1997) **80**(12 Suppl), 2505-2509.
- Erdi YE, Rosenzweig K, Erdi AK, Macapinlac HA, Hu YC, Braban LE, Humm JL, Squire OD, Chui CS, Larson SM, Yorke ED. "Radiotherapy treatment planning for patients with non-small cell lung cancer using positron emission tomography (PET)." *Radiother Oncol.* (2002) **62**(1), 51-60.
- Ezhil M, Vedam S, Balter P, Choi B, Mirkovic D, Starkschall G, Chang JY. "Determination of patient-specific internal gross tumor volumes for lung cancer using four-dimensional computed tomography." *Radiat Oncol.* (2009) **44**.
- Feng S, Liang Q, Kinser RD, Newland K, Guilbaud R. "Testing equivalence between two laboratories or two methods using paired-sample analysis and interval hypothesis testing." *Anal Bioanal Chem.* (2006) **385**(5), 975-981.
- Flampouri S, Jiang SB, Sharp GC, Wolfgang J, Patel AA, Choi NC. "Estimation of the delivered patient dose in lung IMRT treatment based on deformable registration of 4D-CT data and Monte Carlo simulations." *Phys Med Biol.* (2006) **51**(11), 2763-2779.

- Furuse K, Fukuoka M, Kawahara M, Nishikawa H, Takada Y, Kudoh S, Katagami N, Ariyoshi Y. "Phase III study of concurrent versus sequential thoracic radiotherapy in combination with mitomycin, vindesine, and cisplatin in unresectable stage III non-small-cell lung cancer." *J Clin Oncol.* (1999) **17**(9), 2692-2699.
- Gagne IM, Robinson DM. "The impact of tumor motion upon CT image integrity and target delineation." *Med Phys.* (2004) **31**(12), 3378-3392.
- Gauden S, Ramsay J, Tripcony L. "The curative treatment by radiotherapy alone of stage I non-small cell carcinoma of the lung." *Chest.* (1995) **108**(5), 1278-1282.
- Geise RA, McCullough EC. "The use of CT scanners in megavoltage photon-beam therapy planning." *Radiology.* (1977) **124**(1), 133-141.
- Gillis S, De Wagter C, Bohsung J, Perrin B, Williams P, Mijnheer BJ. "An inter-centre quality assurance network for IMRT verification: results of the ESTRO QUASIMODO project." *Radiother Oncol.* (2005) **76**(3), 340-353.
- Giraud P, Elles S, Helfre S, De Rycke Y, Servois V, Carette MF, Alzieu C, Bondiau PY, Dubray B, Touboul E, Housset M, Rosenwald JC, Cosset JM. "Conformal radiotherapy for lung cancer: different delineation of the gross tumor volume (GTV) by radiologists and radiation oncologists." *Radiother Oncol.* (2002) **62**(1), 27-36.
- Glide-Hurst CK, Hugo GD, Liang J, Yan D. "A simplified method of four-dimensional dose accumulation using the mean patient density representation." *Med Phys.* (2008) **35**(12), 5269-5277.
- Goo JM, Tongdee T, Tongdee R, Yeo K, Hildebolt CF, Bae KT. "Volumetric measurement of synthetic lung nodules with multi-detector row CT: effect of various image

- reconstruction parameters and segmentation thresholds on measurement accuracy." *Radiology*. (2005) **235**(3), 850-856.
- Gould KL, Pan T, Loghin C, Johnson NP, Sdringola S. "Reducing radiation dose in rest-stress cardiac PET/CT by single poststress cine CT for attenuation correction: quantitative validation." *J Nucl Med*. (2008) **49**(5), 738-745.
- Govindan R. "Management of patients with non-small cell lung cancer and poor performance status." *Curr Treat Options Oncol*. (2003) **4**(1), 55-59.
- Guckenberger M, Wilbert J, Krieger T, Richter A, Baier K, Meyer J, Flentje M. "Four-dimensional treatment planning for stereotactic body radiotherapy." *Int J Radiat Oncol Biol Phys*. (2007) **69**(1), 276-285.
- Guckenberger M, Wilbert J, Meyer J, Baier K, Richter A, Flentje M. "Is a single respiratory correlated 4D-CT study sufficient for evaluation of breathing motion?" *Int J Radiat Oncol Biol Phys*. (2007) **67**(5), 1352-1359.
- Guerrero T, Sanders K, Castillo E, Zhang Y, Bidaut L, Pan T, Komaki R. "Dynamic ventilation imaging from four-dimensional computed tomography." *Phys Med Biol*. (2006) **51**(4), 777-791.
- Hudson HM, Larkin S. "Accelerated image reconstruction using ordered subsets of projection data." *IEEE Trans Med Imag*. (1994) **13**601-609.
- International Commission on Radiation Units and Measurements. Prescribing, recording, and reporting photon beam therapy. Bethesda, Md.: International Commission on Radiation Units and Measurements; 1999.

Kang Y, Zhang X, Chang JY, Wang H, Wei X, Liao Z, Komaki R, Cox JD, Balter PA, Liu H, Zhu XR, Mohan R, Dong L. "4D Proton treatment planning strategy for mobile lung tumors." *Int J Radiat Oncol Biol Phys.* (2007) **67**(3), 906-914.

Keall PJ, Siebers JV, Joshi S, Mohan R. "Monte Carlo as a four-dimensional radiotherapy treatment-planning tool to account for respiratory motion." *Phys Med Biol.* (2004) **49**(16), 3639-3648.

Keall PJ, Starkschall G, Shukla H, Forster KM, Ortiz V, Stevens CW, Vedam SS, George R, Guerrero T, Mohan R. "Acquiring 4D thoracic CT scans using a multislice helical method." *Phys Med Biol.* (2004) **49**(10), 2053-2067.

Keall PJ, Mageras GS, Balter JM, Emery RS, Forster KM, Jiang SB, Kapatoes JM, Low DA, Murphy MJ, Murray BR, Ramsey CR, Van Herk MB, Vedam SS, Wong JW, Yorke E. "The management of respiratory motion in radiation oncology report of AAPM Task Group 76." *Med Phys.* (2006) **33**(10), 3874-3900.

Kemerink GJ, Lamers RJ, Pellis BJ, Kruize HH, van Engelshoven JM. "On segmentation of lung parenchyma in quantitative computed tomography of the lung." *Med Phys.* (1998) **25**(12), 2432-2439.

Khan FM. *The physics of radiation therapy.* 3rd ed. Philadelphia: Lippincott Williams & Wilkins; 2003.

Kim J, Ferree Jr. GD. "Standardization in Causal Analysis." *Sociological Methods & Research.* (1981) **10**187-210.

Lagerwaard FJ, Van Sornsens de Koste JR, Nijssen-Visser MR, Schuchhard-Schipper RH, Oei SS, Munne A, Senan S. "Multiple "slow" CT scans for incorporating lung tumor

- mobility in radiotherapy planning." *Int J Radiat Oncol Biol Phys.* (2001) **51**(4), 932-937.
- Lange K, Carson R. "EM reconstruction algorithms for emission and transmission tomography." *J Comput Assist Tomogr.* (1984) **8**(2), 306-316.
- Lay DC. *Linear algebra and its applications.* 2nd ed. Reading, Mass.: Addison-Wesley; 1997.
- Limpert E, Werner AS, Abbt M. "Log-normal distributions across the sciences: Keys and clues." *BioScience.* (2001) **51**(5), 341-352.
- Liu HH, Balter P, Tutt T, Choi B, Zhang J, Wang C, Chi M, Luo D, Pan T, Hunjan S, Starkschall G, Rosen I, Prado K, Liao Z, Chang J, Komaki R, Cox JD, Mohan R, Dong L. "Assessing respiration-induced tumor motion and internal target volume using four-dimensional computed tomography for radiotherapy of lung cancer." *Int J Radiat Oncol Biol Phys.* (2007) **68**(2), 531-540.
- Low DA, Harms WB, Mutic S, Purdy JA. "A technique for the quantitative evaluation of dose distributions." *Med Phys.* (1998) **25**(5), 656-661.
- Low DA, Dempsey JF. "Evaluation of the gamma dose distribution comparison method." *Med Phys.* (2003) **30**(9), 2455-2464.
- Low DA, Nystrom M, Kalinin E, Parikh P, Dempsey JF, Bradley JD, Mutic S, Wahab SH, Islam T, Christensen G, Politte DG, Whiting BR. "A method for the reconstruction of four-dimensional synchronized CT scans acquired during free breathing." *Med Phys.* (2003) **30**(6), 1254-1263.

- Lowry R. "VassarStats: Web Site for Statistical Computation." Poughkeepsie, Lowry, Richard, 2008. <http://faculty.vassar.edu/lowry/VassarStats.html>
- Lujan AE, Larsen EW, Balter JM, Ten Haken RK. "A method for incorporating organ motion due to breathing into 3D dose calculations." *Med Phys.* (1999) **26**(5), 715-720.
- Mageras GS, Pevsner A, Yorke ED, Rosenzweig KE, Ford EC, Hertanto A, Larson SM, Lovelock DM, Erdi YE, Nehmeh SA, Humm JL, Ling CC. "Measurement of lung tumor motion using respiration-correlated CT." *Int J Radiat Oncol Biol Phys.* (2004) **60**(3), 933-941.
- Mah K, Caldwell CB, Ung YC, Danjoux CE, Balogh JM, Ganguli SN, Ehrlich LE, Tirona R. "The impact of (18)FDG-PET on target and critical organs in CT-based treatment planning of patients with poorly defined non-small-cell lung carcinoma: a prospective study." *Int J Radiat Oncol Biol Phys.* (2002) **52**(2), 339-350.
- Marin D, Nelson RC, Schindera ST, Richard S, Youngblood RS, Yoshizumi TT, Samei E. "Low-tube-voltage, high-tube-current multidetector abdominal CT: improved image quality and decreased radiation dose with adaptive statistical iterative reconstruction algorithm--initial clinical experience." *Radiology.* (2010) **254**(1), 145-153.
- McClelland JR, Blackall JM, Tarte S, Chandler AC, Hughes S, Ahmad S, Landau DB, Hawkes DJ. "A continuous 4D motion model from multiple respiratory cycles for use in lung radiotherapy." *Med Phys.* (2006) **33**(9), 3348-3358.
- Moller T, Trumbore B. "Fast, Minimum Storage Ray-Triangle Intersection." *J Graphics Tools.* (1997) **2**(1), 21-28.

Muirhead R, McNee SG, Featherstone C, Moore K, Muscat S. "Use of Maximum Intensity Projections (MIPs) for target outlining in 4DCT radiotherapy planning." *J Thorac Oncol.* (2008) **3**(12), 1433-1438.

NCI. "Stage Information for Non-Small Cell Lung Cancer." Rockville, National Cancer Institute, 2010. <http://www.cancer.gov/cancertopics/pdq/treatment/non-small-cell-lung/HealthProfessional/page4>

Nehmeh SA, Erdi YE, Pan T, Yorke E, Mageras GS, Rosenzweig KE, Schoder H, Mostafavi H, Squire O, Pevsner A, Larson SM, Humm JL. "Quantitation of respiratory motion during 4D-PET/CT acquisition." *Med Phys.* (2004) **31**(6), 1333-1338.

Nestle U, Walter K, Schmidt S, Licht N, Nieder C, Motaref B, Hellwig D, Niewald M, Ukena D, Kirsch CM, Sybrecht GW, Schnabel K. "18F-deoxyglucose positron emission tomography (FDG-PET) for the planning of radiotherapy in lung cancer: high impact in patients with atelectasis." *Int J Radiat Oncol Biol Phys.* (1999) **44**(3), 593-597.

Nestle U, Kremp S, Schaefer-Schuler A, Sebastian-Welsch C, Hellwig D, Rube C, Kirsch CM. "Comparison of different methods for delineation of 18F-FDG PET-positive tissue for target volume definition in radiotherapy of patients with non-Small cell lung cancer." *J Nucl Med.* (2005) **46**(8), 1342-1348.

Nestle U, Kremp S, Grosu AL. "Practical integration of [18F]-FDG-PET and PET-CT in the planning of radiotherapy for non-small cell lung cancer (NSCLC): the technical basis, ICRU-target volumes, problems, perspectives." *Radiother Oncol.* (2006) **81**(2), 209-225.

Okubo M, Nishimura Y, Nakamatsu K, Okumura M, Shibata T, Kanamori S, Hanaoka K, Hosono M. "Static and moving phantom studies for radiation treatment planning in

- a positron emission tomography and computed tomography (PET/CT) system." *Ann Nucl Med.* (2008) **22**(7), 579-586.
- Onishi H, Shirato H, Nagata Y, Hiraoka M, Fujino M, Gomi K, Niibe Y, Karasawa K, Hayakawa K, Takai Y, Kimura T, Takeda A, Ouchi A, Hareyama M, Kokubo M, Hara R, Itami J, Yamada K, Araki T. "Hypofractionated stereotactic radiotherapy (HypoFXSRT) for stage I non-small cell lung cancer: updated results of 257 patients in a Japanese multi-institutional study." *J Thorac Oncol.* (2007) **2**(7 Suppl 3), S94-100.
- Pan T, Lee TY, Rietzel E, Chen GT. "4D-CT imaging of a volume influenced by respiratory motion on multi-slice CT." *Med Phys.* (2004) **31**(2), 333-340.
- Pan T. "Comparison of helical and cine acquisitions for 4D-CT imaging with multislice CT." *Med Phys.* (2005) **32**(2), 627-634.
- Pan T, Mawlawi O, Nehmeh SA, Erdi YE, Luo D, Liu HH, Castillo R, Mohan R, Liao Z, Macapinlac HA. "Attenuation correction of PET images with respiration-averaged CT images in PET/CT." *J Nucl Med.* (2005) **46**(9), 1481-1487.
- Pan T, Mawlawi O, Luo D, Liu HH, Chi PC, Mar MV, Gladish G, Truong M, Erasmus J, Jr., Liao Z, Macapinlac HA. "Attenuation correction of PET cardiac data with low-dose average CT in PET/CT." *Med Phys.* (2006) **33**(10), 3931-3938.
- Pan T, Sun X, Luo D. "Improvement of the cine-CT based 4D-CT imaging." *Med Phys.* (2007) **34**(11), 4499-4503.
- Pantarotto JR, Piet AH, Vincent A, van Sornsen de Koste JR, Senan S. "Motion analysis of 100 mediastinal lymph nodes: potential pitfalls in treatment planning and adaptive strategies." *Int J Radiat Oncol Biol Phys.* (2009) **74**(4), 1092-1099.

American Association of Physicists in Medicine, "Tissue inhomogeneity corrections for megavoltage photon beams," Madison, WI: American Association of Physicists in Medicine; 2004.

Park K, Huang L, Gagne H, Papiez L. "Do maximum intensity projection images truly capture tumor motion?" *Int J Radiat Oncol Biol Phys.* (2009) **73**(2), 618-625.

Park SJ, Ionascu D, Killoran J, Mamede M, Gerbaudo VH, Chin L, Berbeco R. "Evaluation of the combined effects of target size, respiratory motion and background activity on 3D and 4D PET/CT images." *Phys Med Biol.* (2008) **53**(13), 3661-3679.

Patz EF, Jr., Lowe VJ, Hoffman JM, Paine SS, Burrowes P, Coleman RE, Goodman PC. "Focal pulmonary abnormalities: evaluation with F-18 fluorodeoxyglucose PET scanning." *Radiology.* (1993) **188**(2), 487-490.

Paulino AC, Johnstone PA. "FDG-PET in radiotherapy treatment planning: Pandora's box?" *Int J Radiat Oncol Biol Phys.* (2004) **59**(1), 4-5.

Pevsner A, Davis B, Joshi S, Hertanto A, Mechalakos J, Yorke E, Rosenzweig K, Nehmeh S, Erdi YE, Humm JL, Larson S, Ling CC, Mageras GS. "Evaluation of an automated deformable image matching method for quantifying lung motion in respiration-correlated CT images." *Med Phys.* (2006) **33**(2), 369-376.

Remeijer P, Rasch C, Lebesque JV, van Herk M. "A general methodology for three-dimensional analysis of variation in target volume delineation." *Med Phys.* (1999) **26**(6), 931-940.

Riegel AC, Berson AM, Destian S, Ng T, Tena LB, Mitnick RJ, Wong PS. "Variability of gross tumor volume delineation in head-and-neck cancer using CT and PET/CT fusion." *Int J Radiat Oncol Biol Phys.* (2006) **65**(3), 726-732.

Riegel AC, Ahmad M, Sun X, Pan T. "Dose calculation with respiration-averaged CT processed from cine CT without a respiratory surrogate." *Med Phys.* (2008) **35**(12), 5738-5747.

Riegel AC, Chang JY, Vedam SS, Johnson V, Chi PC, Pan T. "Cine computed tomography without respiratory surrogate in planning stereotactic radiotherapy for non-small-cell lung cancer." *Int J Radiat Oncol Biol Phys.* (2009) **73**(2), 433-441.

Riegel AC, Bucci KM, Mawlawi O, Johnson V, Ahmad M, Sun X, Luo D, Chandler AG, Pan T. "Target definition of moving lung tumors in positron emission tomography: Correlation of optimal activity concentration thresholds with object size, motion extent, and source-to-background ratio." *Med Phys.* (2010) **37**(4), 1742-1752.

Rietzel E, Chen GT, Choi NC, Willet CG. "Four-dimensional image-based treatment planning: Target volume segmentation and dose calculation in the presence of respiratory motion." *Int J Radiat Oncol Biol Phys.* (2005) **61**(5), 1535-1550.

Rietzel E, Pan T, Chen GT. "Four-dimensional computed tomography: image formation and clinical protocol." *Med Phys.* (2005) **32**(4), 874-889.

Rietzel E, Liu AK, Doppke KP, Wolfgang JA, Chen AB, Chen GT, Choi NC. "Design of 4D treatment planning target volumes." *Int J Radiat Oncol Biol Phys.* (2006) **66**(1), 287-295.

Rietzel E, Liu AK, Chen GT, Choi NC. "Maximum-intensity volumes for fast contouring of lung tumors including respiratory motion in 4DCT planning." *Int J Radiat Oncol Biol Phys.* (2008) **71**(4), 1245-1252.

Sause WT, Scott C, Taylor S, Johnson D, Livingston R, Komaki R, Emami B, Curran WJ, Byhardt RW, Turrisi AT, et al. "Radiation Therapy Oncology Group (RTOG) 88-08 and Eastern Cooperative Oncology Group (ECOG) 4588: preliminary results of a phase III trial in regionally advanced, unresectable non-small-cell lung cancer." *J Natl Cancer Inst.* (1995) **87**(3), 198-205.

Shepp LA, Vardi Y. "Maximum likelihood reconstruction for emission tomography." *IEEE Trans Med Imag.* (1972) **1**(2), 113-122.

Sher DJ, Wolfgang JA, Niemierko A, Choi NC. "Quantification of mediastinal and hilar lymph node movement using four-dimensional computed tomography scan: implications for radiation treatment planning." *Int J Radiat Oncol Biol Phys.* (2007) **69**(5), 1402-1408.

Soret M, Bacharach SL, Buvat I. "Partial-Volume Effect in PET Tumor Imaging." *J Nucl Med.* (2007) **48**(6), 932-945.

Spezi E, Lewis DG. "Gamma histograms for radiotherapy plan evaluation." *Radiother Oncol.* (2006) **79**(2), 224-230.

Starkschall G, Desai N, Balter P, Prado K, Luo D, Cody D, Pan T. "Quantitative assessment of four-dimensional computed tomography image acquisition quality." *J Appl Clin Med Phys.* (2007) **8**(3), 2362.

- Stevens CW, Munden RF, Forster KM, Kelly JF, Liao Z, Starkschall G, Tucker S, Komaki R. "Respiratory-driven lung tumor motion is independent of tumor size, tumor location, and pulmonary function." *Int J Radiat Oncol Biol Phys.* (2001) **51**(1), 62-68.
- Suh Y, Sawant A, Venkat R, Keall PJ. "Four-dimensional IMRT treatment planning using a DMLC motion-tracking algorithm." *Phys Med Biol.* (2009) **54**(12), 3821-3835.
- Sura S, Greco C, Gelblum D, Yorke ED, Jackson A, Rosenzweig KE. "(18)F-fluorodeoxyglucose positron emission tomography-based assessment of local failure patterns in non-small-cell lung cancer treated with definitive radiotherapy." *Int J Radiat Oncol Biol Phys.* (2008) **70**(5), 1397-1402.
- Timmerman RD, Park C, Kavanagh BD. "The North American experience with stereotactic body radiation therapy in non-small cell lung cancer." *J Thorac Oncol.* (2007) **2**(7 Suppl 3), S101-112.
- Underberg RW, Lagerwaard FJ, Cuijpers JP, Slotman BJ, van Sornsen de Koste JR, Senan S. "Four-dimensional CT scans for treatment planning in stereotactic radiotherapy for stage I lung cancer." *Int J Radiat Oncol Biol Phys.* (2004) **60**(4), 1283-1290.
- Underberg RW, Lagerwaard FJ, Slotman BJ, Cuijpers JP, Senan S. "Use of maximum intensity projections (MIP) for target volume generation in 4DCT scans for lung cancer." *Int J Radiat Oncol Biol Phys.* (2005) **63**(1), 253-260.
- van Baardwijk A, Baumert BG, Bosmans G, van Kroonenburgh M, Stroobants S, Gregoire V, Lambin P, De Ruyscher D. "The current status of FDG-PET in tumour volume definition in radiotherapy treatment planning." *Cancer Treat Rev.* (2006) **32**(4), 245-260.

van Baardwijk A, Bosmans G, Boersma L, Buijsen J, Wanders S, Hochstenbag M, van Suylen RJ, Dekker A, Dehing-Oberije C, Houben R, Bentzen SM, van Kroonenburgh M, Lambin P, De Ruyscher D. "PET-CT-based auto-contouring in non-small-cell lung cancer correlates with pathology and reduces interobserver variability in the delineation of the primary tumor and involved nodal volumes." *Int J Radiat Oncol Biol Phys.* (2007) **68**(3), 771-778.

Wendling M, Zijp LJ, McDermott LN, Smit EJ, Sonke JJ, Mijnheer BJ, van Herk M. "A fast algorithm for gamma evaluation in 3D." *Med Phys.* (2007) **34**(5), 1647-1654.

Xu F, Mueller K. "Real-time 3D computed tomographic reconstruction using commodity graphics hardware." *Phys Med Biol.* (2007) **52**(12), 3405-3419.

Yaremko B, Riauka T, Robinson D, Murray B, Alexander A, McEwan A, Roa W. "Thresholding in PET images of static and moving targets." *Phys Med Biol.* (2005) **50**(24), 5969-5982.

Zou KH, Warfield SK, Bharatha A, Tempany CM, Kaus MR, Haker SJ, Wells WM, 3rd, Jolesz FA, Kikinis R. "Statistical validation of image segmentation quality based on a spatial overlap index." *Acad Radiol.* (2004) **11**(2), 178-189.

VITA

Adam Christopher Riegel was born in Philadelphia, Pennsylvania on March 15, 1982, the son of Christine Galione Riegel and Bruce Marvin Riegel. After graduating from Upper Dublin High School in Fort Washington, Pennsylvania in 2000, he entered Vassar College in Poughkeepsie, New York for his undergraduate education. Adam received the degree of Bachelor of Arts with a major in physics and correlate sequence in mathematics from Vassar in May 2004. Adam worked as a research associate in the radiation oncology department at St. Vincent's Comprehensive Cancer Center in New York City for a year. In August 2005, he entered the medical physics program at The University of Texas Health Science Center at Houston Graduate School of Biomedical Sciences.